Optimization of Ti-6Al-4V and its foams for biomedical applications by field assisted sintering technique

Dissertation

zur Erlangung des akademischen .Grades
Doctor rerum naturalium (Dr. rer. nat.)

am Institut für Physik
der Mathematisch-Naturwissenschaftlichen Fakultät
der Universität Rostock

Rostock, März 2015

vorgelegt von:
Yujie Quan
aus Rostock
geboren am 06.10.1982 in Shandong, China

urn:nbn:de:gbv:28-diss2015-0160-0

Gutachter:

1. Gutachter:

   Prof. Dr. Eberhard Burkel,

   Institut für Physik, Universität Rostock

2. Gutachter:

   Prof. Dr. Hermann Seitz

   Fakultät für Maschinenbau und Schiffstechnik, Universität Rostock

Datum der Einreichung: 27. März 2015

Datum der Verteidigung: 28. August 2015

Contents

Abstract

Titanium and its alloys are significant for long-term load-bearing orthopedic applications because of their unique mechanical properties and their resistance to corrosion. The literature describes a number of processes that have been applied to produce Titanium and its alloy implants, but the optimization of the metallic implants with mechanical properties matching that of human bones is still a challenging topic. It is obvious that there is room for improvement in the existing production methods. In this thesis, powder metallurgy processes are used to generate the Ti-6Al-4V alloys by the field assisted sintering technique, for the first time, combined with a rapid gas cooling system. The influences of the sintering temperatures, the compaction pressures and the cooling rates on the microstructures and mechanical properties of the alloys are studied in detail. It could be proven that the rapid cooling has an important effect on the microstructures, while maintaining the nanostructures of the raw materials. This allowed to improve the mechanical properties of the sintered alloys. At the same time, porous structures are designed to achieve implants with low elastic modulus to improve the fixation between the bone and the implants. The work presented in this thesis demonstrates that the field assisted sintering technique is a suitable method to produce the Ti-6Al-4V implants with well controlled mechanical and structural characteristics.

Chapter 01 General introduction

1.1. Bone scaffolds

Since healthcare improves and people tend to live longer, materials with biomedical applications become more important. There is a general need to develop materials that can be implanted into the body. Bone graft is the second most common transplantation tissue [1]. The traditional biological methods of bone-defect management include autografting and allografting bone [2]. Autograft is considered ideal for grafting procedures, providing osteoinductive growth factors, osteogenic cells, and an osteoconductive scaffold [3]. However, the harvest of the autologous graft requires an additional invasive surgical procedure that may lead to donor site morbidity, chronic post-operative pain, hypersensitivity and infection. Another drawback of the use of autograft is the limited availability. Allograft can extend autograft, but has limited biological and mechanical properties and carries with it the potential for disease transmission. Also, it has not been accepted in some societies for other reasons [4, 5].

Due to the disadvantages of natural bone grafts, the use of synthetic graft substitutes is of increasing interest. A large number of bone graft alternatives are currently commercially available for orthopaedic use. These span the whole spectrum of materials types, from ceramics to polymers, metals and composites [6]. Ceramics were synthetically made from calcium phosphate that have been used in dentistry and in orthopaedics since the 1980s [7, 8]. Ceramics show excellent corrosion resistance and good bioactive properties, but they are brittle with low tensile strength, due to their intrinsic brittleness. Extensive work has been carried out to study the polymeric implants [9-11]. Polymeric systems are deemed to be ductile with insufficient rigidity and inability to sustain the mechanical forces present in the bone replacement surgery.

From a mechanical point, the synthetic bone substitutes should have similar mechanical properties to that of the bones being replaced. This needs to be matched with a similar modulus of elasticity to that of bone in an attempt to prevent stress shielding, as well as, to maintain adequate toughness to prevent a fatigue fracture under cyclic loading. Metals are more suitable for loading-bearing applications compared with ceramics or polymeric materials due to their combination of high-mechanical strength and fracture toughness.

1.2. Desired features of bone grafts

The design and selection of biomaterials depend on the intended medical application. Regardless of the bone graft material, certain considerations are necessary:

1.2.1. Biocompatibility

The most widely used definition for bicompatibility, comes from a consensus conference on definitions in biomaterials [12]: “Biocompatibility is the ability of a material to perform with an appropriate host response in a specific application.” Any materials designed for surgical implantation into the body should be biocompatible [13]. The two main factors that influence the biocompatibility of a material are the host response induced by the material and the materials degradation in the body environment. When implants are exposed to human tissues and fluids, several reactions take place between the host and the implant material. The issues with regard to biocompatibility are (1) thrombosis, which involves blood coagulation and adhesion of blood platelets to the biomaterial surface, and (2) the fibrous tissue encapsulation of the biomaterials that are implanted in soft tissues [14].

1.2.2. Mechanical properties

The mechanical properties of an ideal bone scaffold should match host bone properties. The failure of implant devices may be mechanical in origin, such as simple shearing of the bone-implant interface, or may be caused by biological processes [15]. The implants with higher stiffness than bone will prevent the needed stress transferred to adjacent bone, resulting in bone resorption around the implant and, consequently, in implant loosening. This leads to death of bone cells which is called the stress shielding effect [16, 17]. Thus adequate mechanical properties such as high fatigue strength and an elastic modulus similar to that of human bone are necessary to avoid fracture and stress-shielding [18].

1.2.3. High corrosion and wear resistance

Corrosion and degradation are generally seen as harmful. The low corrosion resistance of the implants in the body fluid results in the release of metal ions into the body. The released ions are found to cause allergic and toxic reactions [19]. The service period of the material is mainly determined by its wear resistance. The low wear resistance also results in implant loosening and wear debris is found to cause several reactions in the tissue [20]. Thus, the development of

implants with excellent resistance to degradation and to wear in the human body environment is important for the longevity of the material.

1.2.4. Osseointegration

Scaffolds should not only have similar mechanical properties to those of the host tissue, but they should also enhance the formation of new bone. In vivo conditions, the supply of oxygen and nutrients is essential for the survival of the growing cells and tissues within scaffolds. A fibrous tissue is formed between the bone and the implant, if the implant is not well integrated with the bone [21]. An ideal scaffold needs to form blood vessels in or around the implant within a few weeks of implantation to actively support the nutrient, oxygen, and waste transport [18, 22]. Porous materials allow the ingrowth of vessels and of the osteoprogenitor cells from the recipient bed into the implant. A must have property for implants is interconnected porosity where the pore size should be at least 100 μm in diameter for the successful diffusion of essential nutrients and oxygen for cell survivability [23].

1.2.5. Availability

Last but not least, the availability is an important factor in the choice of a material for biomedical applications. In order to achieve effective economic cost and good process ability, materials need to be relatively easy to be processed.

1.3. Metallic biomaterials

The replacement arthroplasty with metallic implants made important advances during the 1950s and 1960s. In the 1950s, stainless steel was successfully used as an implant material in the surgical field for the first time [24]. McKee introduced a metal-on-metal hip prosthesis in which components were originally made of stainless steel and rapidly changed to a cobalt-chromium-molybdenum alloy to mitigate the excessive friction and rapid loosening of the stainless steel pair [25]. Braenemark began his initial research into the development of titanium implant system in1952 and the first implant was placed in a patient in 1965 [26]. The materials currently used for surgical implants include stainless steels, cobalt-base alloys, titanium-base alloys, and tantalum, with an increasing number of devices being made of titanium and titanium alloys. An increased use of titanium alloys as biomaterials is occurring due to their outstanding characteristics such as high specific strength, complete inertness to body environment, lower modulus, superior

biocompatibility and enhanced corrosion resistance when compared to more conventional stainless steels and cobalt-based alloys [27]. Table 1.1 reinforces this point by demonstrating different scaffolds properties.

Table 1.1. Comparison for different biomaterials (adapted from [27])

	Stainless steels	Cobalt-base alloys	Ti and Ti alloys
Alloying elements	Fe, Cr, Ni, Mo	Co, Cr, Mo, Ni	Ti, Al, V, Nb
Advantages	Cost Availability Processing	Wear resistance Corrosion resistance Fatigue strength	Biocompatibility Corrosion resistance Minimum modulus Fatigue strength
Disadvantages	Long term behavior High modulus	High modulus Biocompatibility	Wear resistance Low shear strength
Primary utilisation	Temporary devices	Dentistry castings Prostheses stems Load-bearing components	Permanent devices

1.4. Physical metallurgy for titanium and titanium alloys

Titanium is a transition metal with an incomplete shell in its electronic structure which enables it to form solid solutions with elements having a size factor within ±20% [27]. In air, it is a highly reactive metal which rapidly absorbs oxygen and water. Titanium has a high melting point (1668°C), exhibiting two allotropic forms. At low temperatures it has a hexagonal closed packed crystal structure (hcp) named α, up to a temperature of (882±2)°C, where it transforms into a body centered cubic structure(bcc) termed β [28].

Depending on the alloying elements, titanium alloys may be classified as α, near α, α+β, metastable or stable β, depending upon their microstructure at room temperature. The alloying elements such as (Al, O, N, C, etc.) that tend to stabilize the α-phase are called alpha stabilizers and the addition of these elements increases the β-transus temperature, while elements that stabilize the β-phase are known as beta stabilizers (V, Mo, Nb, Fe, Co, Si, Cr, Ta, etc.). The addition of these elements depresses the β-transus temperature. The elements that do not have

any remarkable effect on the stability of the phases are termed as neutral elements such as Zr and Sn [28].

The alpha and near-α titanium alloys exhibit superior corrosion resistance. Their utility as biomedical materials is principally limited by their low strength. In contrast, α+β alloys exhibit higher strength due to the presence of both α and β phases. Their properties depend upon the composition, the relative proportions of the α/β phases, and the thermal treatment and thermo-mechanical processing conditions [29]. The beta titanium alloys show high strength, good formability and high hardenability and they also offer the unique possibility of a low elastic modulus combined with superior corrosion resistance [30]. Most of the biomedical titanium alloys belong to the α+β or the metastable β class [14].

1.5. Titanium and titanium alloys as biomaterials

Some specific properties of titanium and its alloys for the use in medicine are [31]: the spontaneous formation of a highly biocompatible dioxide passivation film in air and blood, thus, providing surfaces that support direct on-growth of local tissues, the corrosion resistance against atmospheric and aggressive fluidic environments that is helpful in long time implant applications, the ability to influence redox reactions at the tissue interface in a way that can modulate cell and tissue behavior, the ability to be fabricated into structured surfaces, to be optimized in morphology and porosity. They are also an improvement over stainless steel and cobalt-chromium alloys in cases where Nuclear Magnetic Resonance Imaging (NMR) and Computed Tomography (CT) are required. Since titanium weighs 40% less than steel, it lightness makes it to a candidate for surgical instruments, particularly microsurgery. There is also an absence of allergic reactions in patients.

1.5.1. Biocompatibility of titanium and its alloys

It is generally accepted that Ti and its alloys are relatively bioinert and that they exhibit acceptable in vitro and in vivo responses for the desired applications. In an optimal situation titanium is capable of the osseointegration with the bone [32]. In addition, the titanium forms a very stable passive layer of TiO_2 on its surface and provides superior biocompatibility. Even if the passive layer is damaged, the layer is immediately rebuilt. In the case of titanium, the nature of the oxide film that protects the metal substrate from corrosion is of particular importance and its physicochemical properties such as crystallinity, impurity segregation etc. have been found to

be quite relevant.

The titanium alloys show superior biocompatibility when compared to the stainless steel and Cr-Co alloys. Reservations have been expressed about the presence of long-term Ti-6Al-4V implants, because elements such as vanadium are toxic in the ionic state. These concerns have led to the development of new beta titanium alloys with nontoxic alloying elements like Ta, Nb, Zr, etc. It is reported that the addition of Ta remarkably reduces the concentration of the metal release [14]. In order to improve osteointagration, bioactivity, biocompatibility, and corrosion resistance, several surface modifications have been developed [33]. The methods include chemical and electrochemical treatments, sol-gel, chemical vapor deposition (CVD), and biochemical modification and physical methods including machining, grinding, polishing, blasting, thermal and plasma spraying, physical vapor deposition (PVD).

1.5.2. Mechanical properties of the orthopaedic titanium alloys

The applicability of various material types in orthopaedic surgery largely depends on their mechanical properties. It is evident that the proper selection of alloying elements with right thermo-mechanical processing has allowed the production of implant materials with enhanced properties.

The mechanical properties of various biomedical implants is compared with bone and shown in Table 1.2. From the biomechanical point of view, it is desirable to have a Young's modulus comparable to that of bone in order to achieve a good load transfer from the implant into the bone, leading to a continuous stimulation of new bone formation [34, 35]. The Young’s moduli of 316L stainless steel and of Co-Cr alloy are much greater than that of cortical bone. Coming to Ti and Ti alloys, their lower moduli varying from 113 GP to 55 GPa, offer a wide range of mechanical properties so that a selection according to the mechanical requirements is possible. The strength of the titanium alloys is very close to that of 316 L stainless steel, and its density is 55% less than that of steel, hence, when compared by specific strength, the titanium alloys outperform any other implant material [28]. However, their Young’s moduli are still higher than that of cortical bone. To further improve the mechanical strength of Ti implants, much effort is currently being carried out to develop new alloys with low elastic moduli that mimic those of bone tissues [24, 32].

The Young’s moduli of β-type titanium alloys are known to be smaller than those of α or α+β type titanium alloys. Therefore, the research and the development of low rigidity β-type titanium

alloys are getting much attention. Alternatively, a first attempt at reducing the elastic modulus of orthopaedic alloys was made by the introduction of α/β titanium alloys having elastic moduli values approximately half than those of stainless steels or Co-Cr-Mo alloys. A further reduction of Young's modulus of Ti alloys can be achieved by alloying with β-stabilizing elements [36]. The problems related to implant stress shielding of bone have resulted in a number of proposed solutions for more flexible designs and low modulus materials. However, they are far from being totally effective due to potential environmental degradation and poor tribological behavior. Synthesis of minimum modulus Ta alloys intended for orthopaedic applications has recently been demonstrated [36]. These alloys exhibit adequate mechanical strengths and elastic moduli lower than other available alloys.

Table 1.2. Different biomaterials developed as orthopaedic implants and their mechanical properties (adapted from[14, 18, 27, 37])

Type of Biomaterials	Young's modulus (Gpa)	Yield strength (MPa)	Ultimate strength (MPa)
Polymer			
PMMA	3.0	-	24-28
UHMA-PE	0.5	-	37-46
Ceramics			
Al_2O_3	-	-	350
ZrO_2	-	-	550-400
Metals			
Stainless steel 316L	205–210	170–750	465–950
Co-Cr alloy	220–230	550–650	800–1200
cp Ti	105	692	785
Ti-6Al-4V	110	850–900	960–970
"New generation"			
Ti-alloys	55–113	275–1585	590–1795
Bone			
Cortical bone	7–40	-	80–200
Cancellous bone	0.1–2	-	2–20

1.5.3. Corrosion behavior of biomedical titanium alloys

All metals and alloys are subjected to corrosion when in contact with body fluid, since the body environment is very aggressive due to the presence of chloride ions and proteins [14]. Local adverse tissue reactions or elicit allergy reactions caused by metallic implants originate

from the release of metal ions from the implant. This release of ions depends upon the corrosion rate of the alloy and on the solubility of the primarily formed corrosion products.

As previously mentioned, the biocompatibility performance of a metallic alloy is closely associated with its corrosion resistance and the biocompatibility of its corrosion products. Ti offers superior corrosion resistance and an outstanding biocompatibility [38]. In air, titanium is covered with a dense passive oxide layer, which protects the metal against corrosion. This oxide layer forms spontaneously on the implant surface in presence of oxygen. The passivation by the oxide layer is robust and persistent under physiological conditions and corrosion currents in normal saline are very low [39]. Ti implants remain virtually unchanged in appearance after implantation. It is the nature of this surface layer that is thought to give titanium its excellent biocompatibility [40]. Becker et al. studied the corrosion behavior and mechanical properties of three medical grade alloys: 316L stainless steel, the Co-29Cr-6Mo and Ti-6Al-4V alloys [41]. Ti-6Al-4V performed best in the combination and was therefore the recommended material for use in biomedical implants. This is attributed to the spontaneous formation of a few nm thick titanium dioxide film that protects the metal from further oxidation [42]. This behavior depends on the alloy composition and the corrosive medium. The fatigue corrosion resistance of titanium is almost independent of the pH value while the fatigue corrosion strength of stainless steel declines below pH 4 [14]. According to the fact that the pH of the body may vary from 3.5 to 9 depending upon the condition of the area around the implant, the corrosion behavior of various titanium alloys has been studied extensively in different environments. The work of Khan et al. on corrosive wear studies of titanium alloys demonstrated that the Ti-6Al-7Nb and Ti-6Al-4V possessed best combination of corrosion and wear in in vitro accelerated corrosion test, although Ti-Nb-Zr and Ti-Mo alloys all displayed excellent corrosion resistance [43]. The corrosion resistance of an alloy is not only affected by its bulk composition but also by the microstructure developed. The presence of the β-phase with elements such as Nb, Ta, etc. in the two phase alloys improves the corrosion resistance of the alloy. Heat treatments that lead to uneven distribution of alloying elements in either of the phase are detrimental with respect to corrosion. The redistribution of the alloying elements during heat treatment has been found to influence the corrosion resistance of an alloy. Moreover, the oxide formed on the surface should be highly stable in various environments, must not undergo dissolution, ought to be strong and adherent and its properties must not change with the change in the pH of the body fluid. Thus, it is highly

essential to select the appropriate alloying elements and the heat treatment procedure to have high corrosion resistant surface for biomedical applications. The titanium alloys tend to repassivate faster than the stainless steel and other biomedical alloys. The research on the interactions between the material and the biological system is relatively new and not yet matured, hence a systematic study based on physical chemistry and life science is required to understand the formation of the oxide film and the repassivated layer obtained under different environments.

1.5.4. Wear behavior of titanium alloys

Tribology, defined as the science and technology of interacting surfaces in relative motion, and embracing the study of friction, wear and lubrication [44], has emerged as a primary field in bioengineering. As some surface contact takes place, the friction between artificial materials is much higher than in natural joints and non-recoverable wear of the artificial joint materials takes place [27]. Failure generally occurs due to excessive wear of the components [45]: The wear debris accumulation produces an adverse cellular response leading to implant loosening eventually ensuing [46] .

Retrieval of implanted Ti-6Al-4V femoral components had generally shown directional scratching of bearing surfaces, those features being non-uniformly distributed over the femoral head area. It has been proposed that when the normal or shear stresses are high enough to induce breakdown of the surface passive layer, the oxide will be disrupted. The exposed metal surface may then either reform a passive layer or an adhesively bond to the polymer surface. The latter situation leads to the continuous removal and reformation of the passivating layer and results in gradual consumption of the alloy material.

An original study on friction and wear properties of implants has shown poor wear characteristics for unalloyed Ti as well as common titanium alloys [47]. This performance was related to the properties of the oxide layer and the deformation behavior of the subsurface regions. Hence, titanium and titanium alloys were considered to have poor oxidative wear resistance when tribo-chemical reactions occur at the contact area. In a fundamental tribological study of titanium sliding against Al_2O_3, the static formation of TiO_2 was reported to decrease the wear and friction coefficient of titanium. As the surface features of titanium alloys are of prime importance of friction and wear resistance, the nature and properties of the oxides present in the near-surface region deserve special attention. Tribo-chemical reactions during use, or even

detailed surface treatments before implantation, modify the surface characteristics of the alloy [48]. Further on, bulk composition has been shown to alter the composition of the surface oxide layer, suggesting that it might be possible to optimize the mechanical response of this outermost layer to improve its properties and the integrity to the bulk material through bulk chemical modifications. The kinetics of repassivation and the shear resistance of the oxide layer are two important parameters that will influence the behavior of the oxide layer. Oxidation reactions at the interface might be the cause of better bonding, reflecting the effect of composition on the surface/interface properties. The poor tribological property of Ti-6Al-4V for the implant articulation surfaces has resulted in the development of surface treatments to enhance the hardness and the abrasive wear resistance of the alloy [49-51]. In addition to the surface characteristics of titanium alloys, a basic understanding of the mechanisms involved in the friction and wear of titanium alloys is required with particular attention on the subsurface deformation induced during wear.

1.6. Synthesis of titanium alloys

Titanium alloys are available in machine, weld, cast, and powder metallurgy (PM) forms. The properties of these various product forms will vary depending on their interstitial contents and thermal-mechanical processing [28, 52].

1.6.1. Machining

To a large extent, machining of titanium and titanium alloys follows criteria that are also applied to common metallic materials. Titanium alloys can be machined at low speed. For optimum machining, heavy feed rates should be used for rough surfaces or to remove contaminated surfaces. A large volume of nonchlorinated cutting fluid should be used. Titanium chips are highly combustible. Extreme care should be taken to avoid possible fire hazards [52].

1.6.2. Welding

Titanium and most industrial titanium alloys may be welded by a wide variety of conventional processes, although its chemical reactivity typically requires special procedures and precautions. Fusion, resistance, flash butt, electron beam, diffusion bonding, and pressure welding techniques are available and are widely practiced to produce joints in titanium and titanium alloys. Designers of welded structures must consider both welding process applicability and the physical

characteristics and the mechanical properties of welds. During welding the metal locally melts, measures have to be taken to avoid that titanium molten metal comes into contact with reactive gases, including oxygen and nitrogen from the air. Generally, a clean environment has to be provided to avoid an embrittlement of the workpiece. Titanium alloy welds commonly are used in fatigue critical applications [28].

1.6.3. Casting

Titanium alloys have excellent casting characteristics. Due to often very extensive metal removal by machining from the ingot to the final component, and the relative expense of titanium material, casting offers a high cost saving potential. Further on, casting enables to avoid extensive post-processing of cast components. Often complex components can be produced for which conventional production methods would be too complex or expensive. However, the high reactivity of titanium in the molten state requires suitable casting technology and has limited the number of titanium foundries. The mechanical and fatigue properties of castings will be slightly lower than for the wrought product. The two casting methods used are rammed graphite mold casting and investment casting. The main fields of application for castings are high performance parts in the aerospace and the marine industry. Furthermore, cast parts from titanium are used in the automotive industry, medical engineering, dental technology as well as the electronics industry [28].

1.6.4. Powder metallurgy

The major reason for using the powder metallurgy (PM) is to produce complex components with little machining, thus keeping production costs down. The powder-metallurgical production of titanium parts covers both the powder production and the compaction of these powders to the final component. Most of the titanium PM effort has been done with Ti-6Al-4V because it is the most widely used alloy having a large data base for comparison. The two general approaches to titanium PM are the blended elements (BE) method and the prealloyed (PA) approach. Normally, the mechanical properties of PM titanium alloys are superior to the cast alloys. The BE method produces a product with less than full density that can be as strong as wrought material, but generally, it has lower ductility, toughness, and fatigue strength. Process modifications can improve these latter properties, even making them comparable to wrought, but they increase costs [28].

1.7. Approach and aims

1.7.1. Field assisted sintering technique

A promising method to produce titanium implants is the powder metallurgy using the field assisted sintering technique (FAST) [53], an electrical discharge sintering method. The equipment consists of a uniaxial compression device and electrical components to apply the pulsed and steady currents. A graphite die and graphite punches are used. The device is commonly placed in a vacuum or in gas controlled environment. The sintering of powder is achieved by combination of pulsed DC currents with rapid heating and pressure application. Unlike conventional sintering techniques of Ti and Ti alloy powders, that require maintaining a high sintering temperature (1200°C–1400°C) in high vacuum for a long time (24 hrs–48 hrs) [54], FAST process is performed in a relatively short period of time. The use of space-holder materials allows a simple and accurate control of pore fraction, shape and connectivity in titanium [55]. This method provides foam structures close to homogenous pore structures and high levels of porosities.

1.7.2. Aims of this thesis

This thesis mainly focuses on two main goals: (1) Investigating the different behavior of Ti-6Al-4V synthesized by the powder metallurgy method to address the influences of various heat treatments, on the physical and structural parameters and, thus, on their mechanical performance. (2) Applying new methods to synthesize porous Ti-6Al-4V that provides satisfying mechanical support and allows for bone ingrowth.

Chapter 02 Theoretical background and instrumentation

2.1. Theoretical background

2.1.1. Crystal structure

Pure titanium, as well as the majority of titanium alloys, is an allotropic element, existing in more than one crystallographic form. At room temperature, titanium has hexagonal close-packed (hcp) crystal structure, which is referred as "alpha" (α) phase. At high temperatures, this structure transforms to a body-centered-cubic (bcc) crystal structure, called "beta" (β) phase at (882±2)°C [28]. The atomic unit cells of the α-titanium and β-titanium are schematically shown in Figure 2.1. In α-titanium the lattice parameters of the crystal structure are a=0.295 nm and c=0.468 nm, giving a c/a ratio of 1.587. For body-centered-cubic β-titanium the lattice is a=0.332 nm.

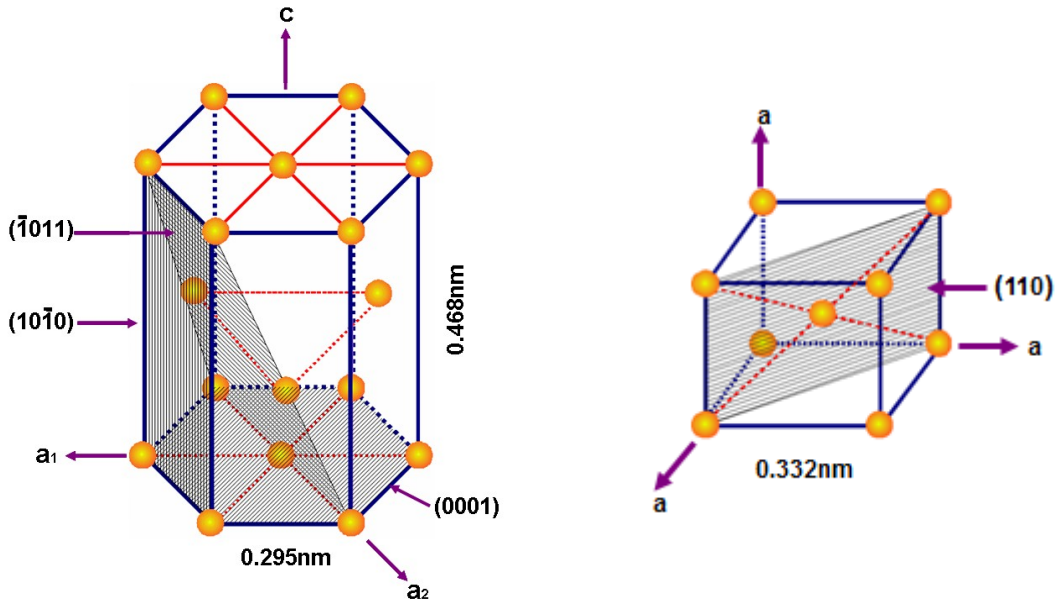

Figurre 2.1. Crystal structure of hcp-α and bcc- β phase[28].

2.1.2. Phase transformation

The complete transformation from one into another crystal structure is called allotropic transformation. The transformation temperature is known as β-transus temperature. Upon cooling from the β-phase field of titanium the most densely packed planes of the β-phase transform to the basal planes of the α-phase. The distance between the basal planes in the α-phase is slightly larger than the corresponding distance between the planes in the β-phase. Therefore, the phase transformation causes a slight atomic distortion (Figure 2.2). This leads to a slight contraction of

the c-axis relative to the a-axis in the α-phase and reduces the c/a-ratio (1.587) below the value of ideally close packed hexagonal atomic structures (1.633).

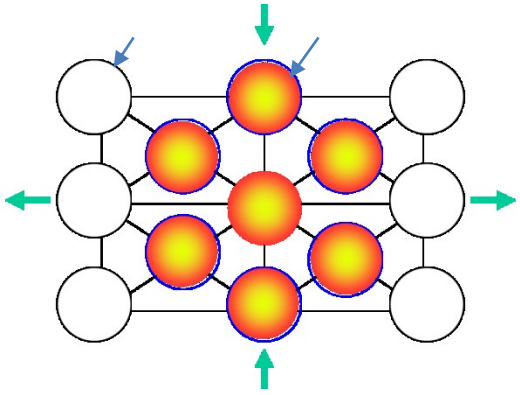

Figure 2.2. Phase transformation according to Burgers relationship[28].

The corresponding transformation of the slip planes of the β titanium into the basal planes of the α titanium and the respective orientations of the slip directions is given by the following Burgers relationship [28]:

$$\{0001\}_{\alpha} // \{110\}_{\beta}, \qquad \langle 1120\rangle_{\alpha} // \langle 111\rangle_{\beta}.$$

2.1.3. Ti-6Al-4V Microstructure

The Ti-6Al-4V is an α+β alloy, originally having been developed as construction alloy for aircraft industry. It belongs to the most significant alloys within the implant alloys for hard tissue replacements [56]. It has high strength, low density, excellent corrosion resistance and the best biocompatibility among metallic materials [57, 58]. In Ti-6Al-4V, alloying elements can act to stabilize either the α or the β-phase. Aluminum stabilizes the α crystal structure by raising the β-transus temperature. Beta stabilizers (vanadium) result in stability of the β-phase at lower temperatures. Through the use of alloying additions, the β-phase can be sufficiently stabilized to coexist with α at room temperature.

The microstructure of this alloy can be varied significantly allowing for fitting the mechanical properties to the specific requirements. Three different types of microstructures can be obtained by changing the thermo-mechanical processing route: lamellar structures, equiaxed structures, and bimodal microstructures containing an equiaxed primary α-phase in a lamellar matrix with an α+β phase [52]. The formation process of the microstructure is shown in Figure 2.3. It uses a constant-composition phase diagram section at 6% Al to illustrate the formation of the α-phase

upon cooling. The phase composition of the Ti-6Al-4V alloy after different heat treatments is mainly the α-phase, with a small amount of the β-phase. This β-phase is present because there is a small amount of vanadium present. Vanadium has low solubility in the α-phase and it therefore is subjected to form the β-phase, either during solidification or subsequent cooling.

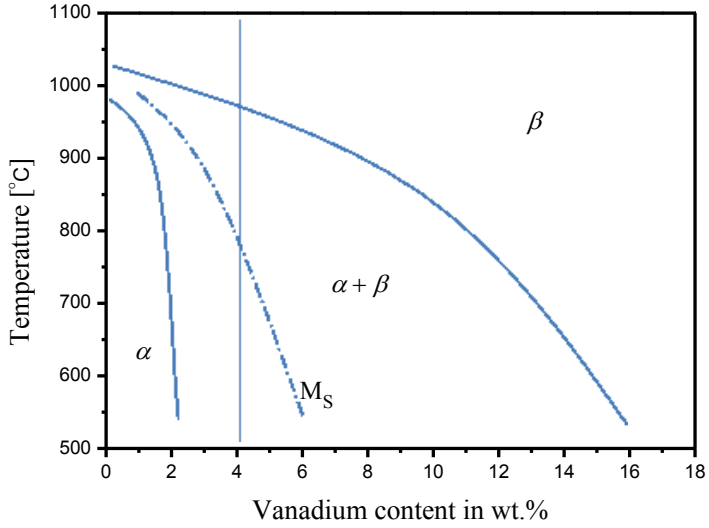

Figure 2.3. Schematic ternary phase diagram Ti-6Al-4V (M_S: martensite start temperature).

Lamellar microstructures are a result of simple cooling from temperatures above the β-transus temperature (the lowest equilibrium temperature at which material is 100% in the β-phase). Once the temperature falls below the β-transus temperature (about 980°C) [52] the α-phase nucleates at the grain boundaries and then grows as lamellae into the prior β-phase grain. Depending on the cooling rate, the lamellae are either fine or coarse. During slow cooling, pure lamellar microstructures are produced, with the lamellae becoming coarser with reduced cooling rates. The microstructure consists of parallel plates of α-phase delineated by the β-phase between them. This microstructural morphology is called a Widmanstätten structure. The diffusional redistribution of the alloying elements leads to the enrichment of the β-phase with the β-phase stabilizer (V). As a result, a small amount of the β-phase remains stable at room temperature. With high cooling rates from temperatures above the martensitic start temperature (M_S) and through the two-phase field, the β-phase transforms into Martensite, resulting in a very fine needle-like microstructure. Unlike lamellar microstructures, equiaxed microstructures are the result of a recrystallization process. The alloy first has to be highly deformed in the α+β field to introduce enough work into the material. Upon subsequent heat treatment at temperatures in the two-phase field, a recrystallized and equiaxed microstructure is generated. Heat treatment below

the β-transus temperature results in bimodal microstructures that can be considered to be a combination of the lamellar and equiaxed microstructure.

2.1.4. Influence of the microstructure on the properties of titanium alloys

The various microstructures have a strong influence on the mechanical behavior of the titanium alloys (Table 2.1). Fine grain sizes can be used to increase the strength as described by the Hall-Petch relationship and the ductility. Coarse microstructures are more resistant to creep and fatigue crack growth. Equiaxed microstructures often have high ductility as well as fatigue strength, while lamellar structures show superior resistance to creep and fatigue crack growth. Bimodal microstructures combine the advantages of lamellar and equiaxed structures, they exhibit a well-balanced property profile.

Table 2.1. Influence of microstructure on properties of titanium alloys (adapted from[52]).

Property	fine	coarse	lamellar	equiaxed
Elastic modulus	o	o	o	+/- (texture)
Strength	+	-	-	+
Ductility	+	-	-	+
Fatigue crack propagation	-	+	+	-
Creep strength	-	+	+	-

2.2. Synthesis methods

2.2.1. Field assisted sintering technique

The field assisted sintering technique (FAST) experiments were performed using the system (FCT system GmbH, Rauenstein, Germany) installed at the Tycho Sinter Lab in the University of Rostock. FAST also known as spark plasma sintering (SPS) [59] or pulsed electric current sintering (PECS) [60] belongs to a class of sintering techniques that involve a pulsed DC current to assist densification. The name SPS has been most widely used in the literature [61]. FAST is probably more accurate because the formation of plasma during sintering has not been well-demonstrated. Figure 2.4 shows a schematic of the main components of the FAST apparatus and a gas cooling set-up that was custom built at the University of Rostock. A typical system consists of a vacuum chamber, electrodes for both current and load delivery, and a power supply capable of delivering high electric currents at relatively low voltages.

The FAST experiments were conducted in vacuum under uniaxial pressure. The parameters that are typically associated with the process include the current, the applied uniaxial pressure, the heating rate and the temperature. The maximum current available depends on the specific FAST apparatus; in the case of the FCT system, the current capacity ranges from 1000 A to 5000 A at 10 V–15 V maximum. The pulsing pattern is made up of a sequence of pulses with the current, followed by the absence of a current. Thus, a pulse pattern of 12/2 means that 12 pulses are applied, followed by a duration of 2 pulses where the current is not applied.

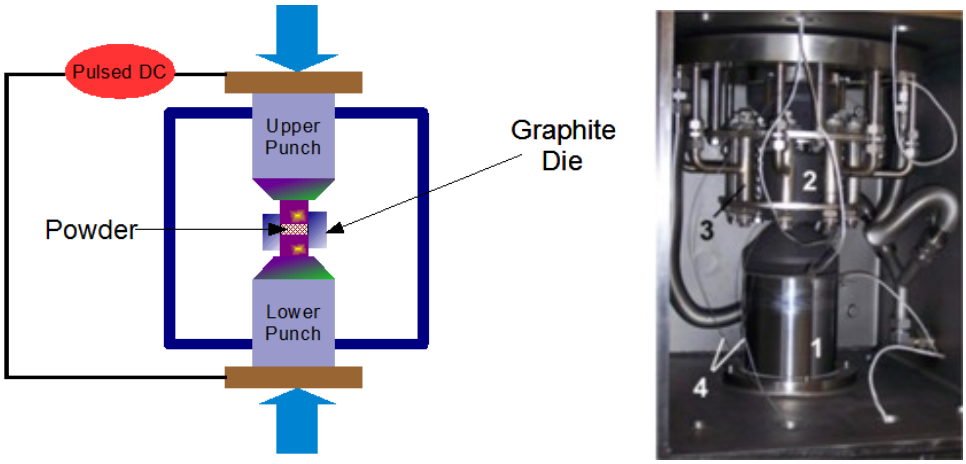

(a) (b)

Figure 2.4. (a) A schematic depicting the main components of a FAST apparatus. (b) A picture of a rapid cooling system(1, machine stamp, 2, sample block, 3, gas nozzle field, 4, thermocouples). This particular system was custom built at the University of Rostock.

The pressure plays a crucial role in the consolidation of materials. During FAST, the samples are densified inside a die that is placed in between the electrode. A uniaxial mechanical load is applied and leads to densification along the thickness direction. Thus, the lateral shrinkage of the sample remains negligible. The maximum pressure that can be uniaxially applied is limited by the mechanical property of die. Generally, materials that are suitable for sintering process are stable at elevated temperatures. Materials that decompose or sublime tend to be poor candidates for sintering. The most common die material is high-purity, high-density graphite because graphite has excellent mechanical strength up to very high temperatures, as well as high thermal and electrical conductivity. In the case of FAST, the electrical current flows through the graphite die and punches, so that the pressing tool also acts as a heating element by Joule heating. The

interior of the graphite die and the surfaces of the punches were covered by a compressible graphite foil to maximize the contact area between the rough powder compact surface and the punches and to reduce friction. To remove the remaining graphite foil, the substrate surface is blasted with compressed air jets carrying the abrasive sands.

The current and the sintering temperature are dependent parameters as Joule heating is the source of the thermal activation. Because of the nature of heating, high heating rates can be achieved in the FAST, as high as about 2000°C/min. Typical values of the heating rate are 100°C/min–600°C/min, and those for pressure are 30 MPa–150 MPa. During the experiments, the temperature is measured in two different ways: a drill hole in the surrounding graphite allows thermocouple temperature measurements; in the central of the graphite set-up, a pyrometer is used. The pyrometer is not able to measure temperatures below 400°C, and, thus, limited for the control of temperatures above 400°C. Figure 2.5 shows the die setup during a sintering run.

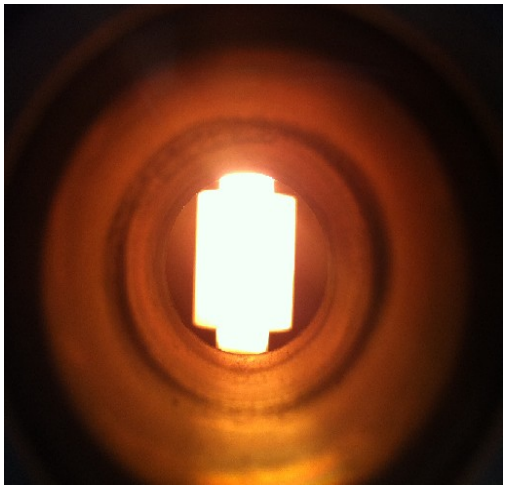

Figure 2.5. The apparatus during a densification run; the die that is visible through the viewport and temperature is at ~1200°C.

The unit is equipped with real-time data acquisition systems that monitor temperature, current, voltage, and displacement. Real-time data allows to monitor the densification process, using the displacement data. However, the observed displacement represents an overall characterization of shrinkage as it also includes contributions from the die and the system, as is demonstrated in Figure 2.6. The data acquisition system does not directly measure sample displacements. To measure the true displacement of the sample using collected displacement data, the system can be calibrated without any sample so that the compliance of the system can be removed. Using such an analysis, the FAST method can provide information on densification.

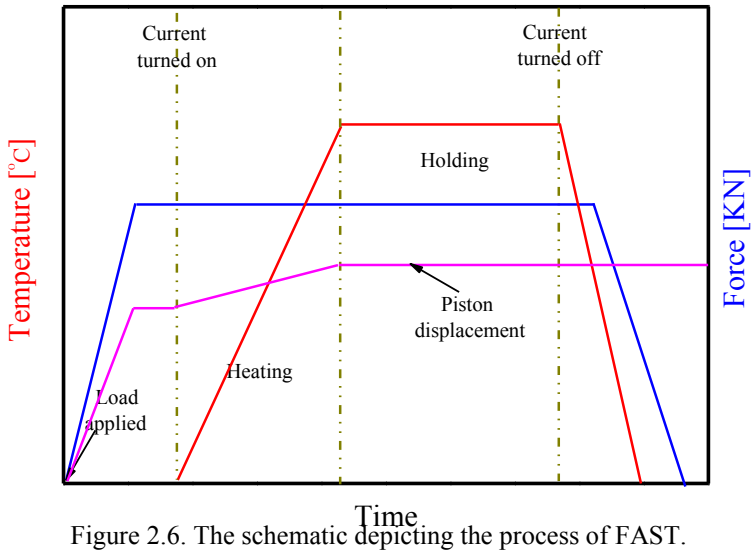

Figure 2.6. The schematic depicting the process of FAST.

The densification mechanisms that take place during this process are not well understood. In conductive materials (metals), it is clear that there is a Joule heating effect when the current is applied, but in the case of nonconductive materials (ceramics), it is palpable that the current goes through the punches and the graphite die. Even the formation of plasma is not clear in the literature. However, what is patent is that FAST allows the processing of materials with maximum density and with the lowest possible grain coarsening; this is a real advantage when nanostructures or nano-powders are used, and the benefits of the nano-features should be maintained during the consolidation of the powders [62, 63].

FAST can be viewed as an evolution of the field assisted hot pressing method. The main difference between FAST and the conventional hot pressing methods is that in FAST, the current is applied in many pulses over very short time instead one unique pulse for a longer time. Advantages of FAST are the short processing time, by using high heating rate. As a result, less grain growth and improved properties can be obtained. In addition, a mechanical compressive load is applied during sintering, which leads to improved properties and advanced densification without sintering aids. The disadvantage of this method is that the shape has just a simple geometry because of the currently available pressing tools.

2.2.2. Metal foam synthesis

Metal foam synthesis started in the 1940s, with one of the first products being aluminum

foam, which was synthesized by inducing gas into molten metal by Sosnik [64]. Metals are tough, thermally and electrically conductive and strong. Foams have low weight and adjustable densities [65]. Metallic macroporous structures in orthopedic implants are attracting increasing attention because they combine high strength, relatively low stiffness that reduces the stress-shielding effect, and porosity that allows full bone in-growth and stable long-term fixation. Various processes have been developed to create porous implants with improved mechanical performance in order to get a stable mechanical bone-implant interface [65-67]. Due to its high melting point and high contamination susceptibility, porous Ti alloys are difficult to be produced from the liquid state. These scaffolds are usually obtained by routes that include solid state foaming by superplastic expansion [68], decomposition of foaming agents [69], directional solidification of liquid titanium with dissolved gas [70], combustion synthesis [71], sintered metal fires and powders [72, 73], plasma spraying [74], rapid prototyping [75-78] and powder metallurgy with help of space holders [55]. Among the production methods, the powder metallurgical with the space-holder technique is promising due to their considerable advantages [79]. The most significant advantages of this method are low cost, better control and the capability of near-net-shape production.

There are some issues that must be considered in using the spacers for synthesis of titanium alloys. First, there is a considerable difference in the particle sizes between the titanium powders and the spacers. In fact, the greater the size differences of the metal and spacer powders are, the tougher the control of the process is. Additionally, some other spacer materials have some solubility in titanium, which affects the final foam properties. Furthermore, the cost of some common spacers is high, which makes them unsuitable for the synthesis. Generally, there are two types of space holders: those that can be removed thermally when the temperature is raised and those that are dissolved and removed by a solvent. To process titanium and titanium alloy foams, there are some typical spacers utilized by researchers. Kotan and Bor [80] used spherical carbamide powders to synthesize Ti-6Al-4V foams. Magnesium is another space holder used to process TiNi foams [81] and pure titanium foams [82]. In a similar process, TiH_2 has been employed in the synthesis of Ti alloy foams [83]. Sodium chloride is another spacer that can be removed by a solvent. It is selected and processed in the production of TiNi shape-memory alloy foams [84]. Sodium chloride is reliable, chemically stable and environmentally friendly that can easily be removed in water. Spherical particles are suitable for foaming; moreover, sodium

chloride is cheap and readily available. The characteristics, structure and applications of sodium chloride make it a good candidate as a spacer. As shown schematically in Figure 2.7, the technique using sodium chloride as a spacer consists of four major steps: powder selection, mixing, compaction and sintering, spacer removal. First, the metal and the spacer powders must be selected. Selecting the proper spacer plays the most crucial role. After selection, the metal and the spacer powders are mixed completely to assure the homogeneity of the mixture. The next step is sintering with compaction of the powders into a mold under controlled pressure. After sintering, the samples are then suspended in water to dissolve the space-holder.

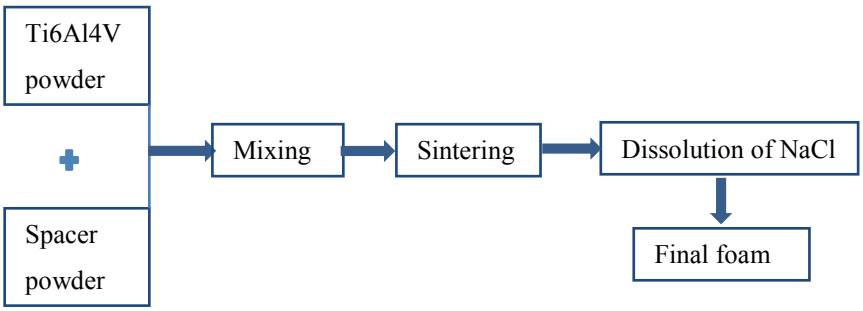

Figure 2.7. Schematic illustration of the pore forming process by using FAST and NaCl dissolution.

2.3. Examination methods

2.3.1. Density and porosity

The density of dense samples was measured by the Archimedes method in water. The mass of samples (m_a) was measured on a balance. Distilled water was used for testing with a density of 1.0 $g \cdot cm^{-3}$ (ρ_w).The sample was attached to a thread and fully immersed in a small beaker with water, without touching the bottom of the beaker. The weight of the sample in water (m_w) was measured, whereby the loss of weight of the sample when suspended in water is equal to the mass of fluid displaced, from which its volume and hence density ρ_d can be calculated:

$$\rho_d = \rho_w \, m_a / (m_a - m_w) \qquad (2\text{-}1)$$

A total of eight specimens in each group were examined and average values were determined. The relative density was calculated by comparing the bulk density of samples with the theoretical density of Ti-6Al-4V: 4.43 $g \cdot cm^{-3}$. Thereafter, the degree of densification was traced using the relative density examination.

One of the most important features of metal foams is their porosity, which defines how most

metal foams will be used. The porosity of foams cannot be measured directly using Archimedes' method. The method can only be used to calculate the volume of water displaced by immersed objects. For this reason, the density obtained from the weight of foams and the volume of water displaced only used for describing the situation of foam struts (ρ_{st}=weight of sample/volume of water displaced). The density (ρ_{st}) will be smaller than the theoretical one (ρ_{th}) when some residual NaCl or closed pores stay in the struts. In the present work, the concept was used to measure the relative density of foam struts (ρ_{st}/ρ_{th}) for tracing the dissolution of NaCl after water submergence. It can be concluded that the method described for calculating the density of sample struts cannot be applied to describe the porosity of foams. Hence, for porous samples, the apparent density (ρ^*) was evaluated from the weight and the apparent volume of the specimens (ρ^*=weight of sample/volume of sample). The relative density calculation was made by dividing the density of the cellular specimen (ρ^*) by density of the parent one (ρ_s), where ρ_s is the density of 100% dense material. The porosity (p) was calculated by the formula: $p=(1-\rho^*/\rho_s)$ x100. A total of 8 foams per structure were measured.

2.3.2. X-ray diffraction with synchrotron radiation

The XRD experiments were performed at the high energy materials science (HEMS) beamline (P07) of the PETRA III synchrotron radiation source at DESY (Hamburg, Germany). The emission of electromagnetic radiation by accelerated electrons is the idea of a synchrotron setup which has important advantages, namely:

1. High intensity: very short data acquisition times possible
2. Tunable wavelength: the users can select the wavelength required for their experiment
3. High stability: submicron source stability
4. High degree of polarization: both linear and circular
5. High penetration depth: non-destructive bulk properties measurable
6. Large Ewald Sphere: small Bragg angles, therefore, monitoring of complete diffraction rings with area detectors possible
7. Highly collimated photon beam generated by a small divergence: study extremely small samples possible
8. Extinction and multiple Bragg scattering negligible

The HEMS beamline at PETRA III is optimized for hard x-rays (i.e. short-wavelength) in the fully tunable range 30 keV–250 keV in order to investigate non-destructively bulk properties or

deeply buried structures and interfaces mainly in the context of materials research. In a typical synchrotron diffraction experiment, monochromatic radiation is used and the sample is analyzed in transmission. A schematic of the diffraction setup is shown in Figure 2.8. A hard X-ray beam illuminated a sample and the sample was irradiated in transmission geometry according to Debye–Scherrer method. For a monochromatic incident beam, the 2-theta angle between the incident and scattered beam is fixed for a given Bragg reflection, but the angle around the incident beam is arbitrary. The locus of all the possible scattered beams is a cone around the direction of the incident beam. For the high energy X-rays the sample absorption is relatively small, making it possible to study several mm thick samples in transmission geometry. The diffracted Debye–Scherrer cones were observed on the detector behind it and recorded using a flat panel 2D detector (Perkin Elmer XRD 1622, USA) with a number of pixels of 2048*2048 and a pixel size of 0.2*0.2 mm^2. Calibration of the wavelength and the sample-to-detector-distance was done by measuring Al_2O_3 as reference.

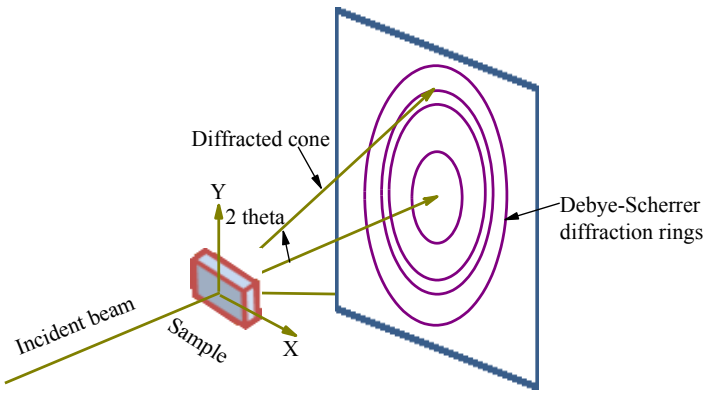

Figure 2.8. Debye- Scherrer geometry of the synchrotron diffraction experiment.

2.3.3. Rietveld refinement

The Rietveld method is a full-profile approach that was initially introduced for the refinement of crystal-structure parameters [85] but has been expanded for application in quantitative phase-analysis. The method is based on a least-squares fit between a measured diffraction pattern and a simulated X-ray-diffraction pattern. The simulated XRD pattern is calculated from a large number of parameters, including crystal-structure parameters of each component phase, a scale

factor for each constituent phase to adjust the relative intensities of the reflections, parameters describing the peak profile and the background, and parameters simulating the instrumental aberrations as well as effects resulting from size-related strain, preferred orientation, and crystallite size [86]. A feature of the quantitative analysis of phase proportions by the Rietveld method is that the phase abundances of the constituent phases can be directly calculated from the refined scale-factors. Therefore, quantitative analysis can be performed without the need of experiments undertaken on standard samples to calibrate the method. It consists in minimizing a function, named residue, which is the net result of the comparison between the experimental data and a simulated one, based on a starting structural model (adapted from [87]).

$$WSS = \sum_i w_i (I_i^{\exp} - I_i^{calc})^2, \quad w_i = \frac{1}{I_i^{\exp}}$$

The spectrum is calculated by the classical intensity equation:

$$I_i^{calc} = S_F \sum_{j=1}^{Nphase} \frac{f_j}{V_j^2} \sum_{k=1}^{Npeaks} L_k \left|F_{k,j}\right|^2 S_j\left(2\theta_i - 2\theta_{k,j}\right) P_{k,j} A_j + bkg_i$$

1. The scale factor (for each phase) is written in classical Rietveld programs as:

$$S_j = S_F \frac{f_j}{V_j^2}$$

S_j = phase scale factor (the overall Rietveld generic scale factor)

S_F = beam intensity (it depends on the measurement)

f_j = phase volume fraction

V_j = phase cell volume

2. The Lorentz-Polarization factor (L_p):

$$Lorentzfactor = \frac{1}{4\sin^2\theta\cos\theta}$$

$$Polarizationfactor = \sqrt{1+\cos^2(2\theta)}$$

$$L_p = \frac{1+\cos^2(2\theta)}{\sin^2\theta\cos\theta}$$

If a monochromator is used, then the polarization factor is $\sqrt{1+\cos^2(2\theta)\cos^2(2\theta_M)}$,

where θ_M is the Bragg angle for the monochromator.

3. The structure factor describes how the atom arrangement affects the scattered beam:

$$\left|F_{k,j}\right|^2 = m_k \left| \sum_{n=1}^{N} f_n e^{-B_n \frac{\sin^2\theta}{\lambda^2}} \left(e^{2\pi i (hx_n + ky_n + lz_n)} \right) \right|^2$$

m_k : the multiplicity of the k reflection (with h, k, l Miller indices)

B_n : the temperature factor

x_n , y_n , z_n : coordinates of the nth atom

f_n : atomic scattering factor

N: number of atoms

4. Of the analytical profile shape function $S_j\left(2\theta_i - 2\theta_{k,j}\right)$ investigated, the pseudo-Voigt approximation of the Voigt function is the most widely used for X-ray and constant wavelength neutron data. The function is simply a linear combination of Lorentzian and Gaussian components in the ratio $\eta/(1-\eta)$, where η is the pseudo-Voigt mixing parameter:

$$PV\left(2\theta_i - 2\theta_k\right) = I_n \left[\eta_k \left(\frac{1}{1+S_{i,k}^2} \right) + \left(1-\eta_k\right) e^{-S_{i,k}^2 \ln 2} \right] , \quad S_{i,k} = \frac{2\theta_i - 2\theta_k}{\omega_k}$$

$$\omega^2 = W + V\tan\theta + U\tan^2\theta$$

Where W, V, U are three experimental fitting parameters (the half width).

5. The March-Dollase formula for preferred orientation function $P_{k,j}$ is used:

$$P_{k,j} = \frac{1}{m_k} \sum_{n=1}^{m_k} \left(P_{MD}^2 \cos^2\alpha_n + \frac{\sin^2\alpha_n}{P_{MD}} \right)^{-\frac{3}{2}}$$

P_{MD} is the March-Dollase parameter, summation is done over all equivalent h k l reflections (m_k), α_n is the angle between the preferred orientation vector and the crystallographic plane h k l.

6. The absorption factor: $A_j = e^{(-\mu t)}$, μ is the linear absorption coefficient and t is the thickness of the sample.
7. The more used background in Rietveld refinements is a polynomial function in 2θ :

$$bkg(2\theta_i) = \sum_{n=0}^{N_b} a_n (2\theta_i)^n$$

Where, N_b is the polynomial degree, a_n is the polynomial coefficients.

8. R indices (N=number of points, P=number of parameters):

$$R_{wp} = \sqrt{\frac{\sum_{i=1}^{N}\left[w_i\left(I_i^{\exp} - I_i^{calc}\right)\right]^2}{\sum_{i=1}^{N}\left[w_i I_i^{\exp}\right]^2}}, \quad R_{\exp} = \sqrt{\frac{(N-P)}{\sum_{i=1}^{N}\left[w_i I_i^{\exp}\right]^2}}, \quad w_i = \frac{1}{\sqrt{I_i^{\exp}}}$$

The R_{wp} factor is the more valuable. Its absolute value does not depend on the absolute value of the intensities. But it depends on the background. With a high background is easy to reach very low values. Increasing the number of peaks is more difficult to get a good value. The R_{exp} is the minimum R_{wp} value reachable using a certain number of refineable parameters. It needs a valid weighting scheme to be reliable.

9. The goodness of fit is the ratio between the Rwp and Rexp:

$$sig = \frac{R_{WP}}{R_{\exp}}$$

The MAUD software program v4.1 was used for the Rietveld refinement [88]. The use of the program Maud proved to be particularly convenient because the measured and the calculated diffraction-patterns, as well as the difference curve, could be observed and compared with the peak positions of stored structures during calculation. The peak profiles were described by separate consideration of the wavelength distribution of the X-ray, the instrumental assemblage, and the contribution of the phases contained in the sample (e.g., crystallite sizes and degree of microstrain). The peak profile was modeled by a modified pseudo-Voigt profile function. The unit-cell parameters, used in the refinement, were a_α=2.950 Å, c_α=4.686 Å for hexagonal close-packed (α-phase) and a_β=3.306 Å for body-centered cubic (β-phase) given by Wyckoff, R. W. G [89]. During routine Rietveld analysis, only the sample function was refined because the

wavelength distribution of the X-ray is constant and the instrumental settings remained unmodified. The quality of the Rietveld refinement was assessed by inspection of the difference curve between the measured and the calculated XRD patterns and examination of numerical criteria of quality. A typical Rietveld refinement plot for Al_2O_3 is given in Figure 2.9 to visualize the goodness of fit obtained between the measured and calculated intensities. The observed weighted residual errors R_{wp} ranged from approximately 6.5% to 15%, indicating very good agreement between the observed and simulated XRD patterns. Ideally, these weighted residual errors should approach the statistically expected values R_{exp} that ranged from 4% to 6%. The calculated goodness-of fit values ranged from approximately 1.0 to 2.5.

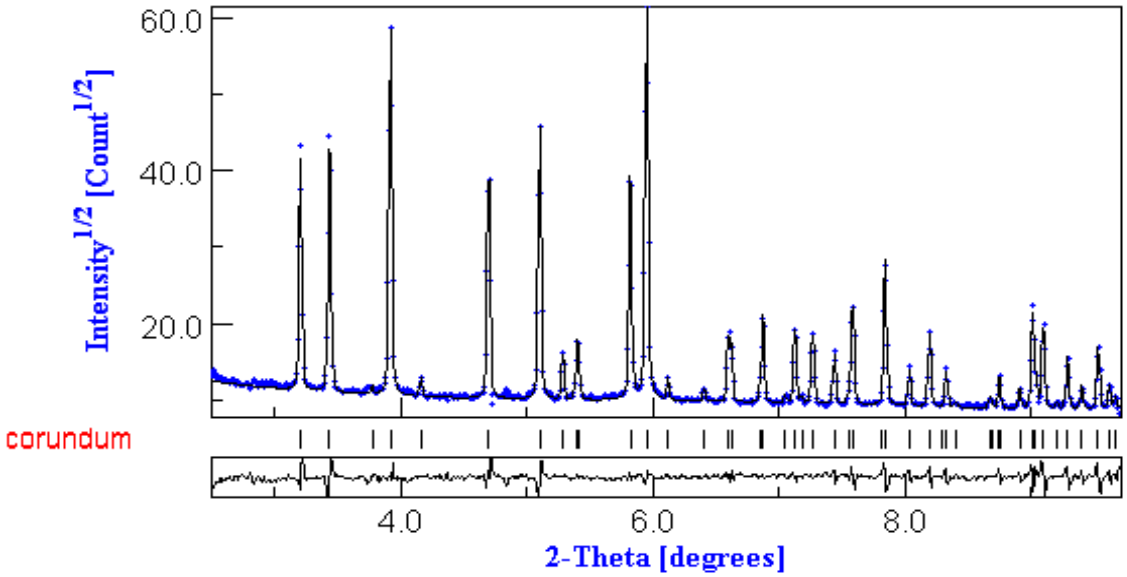

Figure 2.9. Rietveld plot of Al_2O_3 from the refinement using synchrotron data.

2.3.4. Metallographic morphology characterization

Optical investigations were conducted with samples cut from the sintered compacts. The polished sample being etched with Kroll's reagent (3 ml HF and 5 ml HNO_3 in 100 ml H_2O) and optical observations were performed to study the microstructure following standard metallographical practice.

2.3.5. Compression evaluations

Mechanical tests were carried out on a universal testing machine (Zwick/Roell, Z050) at room

temperature, equipped with a 50 kN load cell at a cross-head speed of 0.3 mm/min with loading direction parallel to the building direction, each with five specimens per group. The dense specimens were cylinders of 5 mm in diameter and 5 mm in height, cut out from the sintered alloy. The porous specimens exhibited cylindrical shape with a diameter of about 20 mm and a height of 20 mm. The data of load and displacement obtained through compressive tests were converted to true stress and strain using the formulae (2-2) and (2-3) assuming that there was no volume change in the compressive specimen [90, 91].

$$\sigma_t = P/F_0*(1-L/L_0) \quad (2\text{-}2)$$

$$\varepsilon = -\ln(1-L/L_0) \quad (2\text{-}3)$$

where σ_t is the true stress, ε is the true strain, P is the measured load, F_0 is the initial cross-sectional area of specimens, L_0 is the initial length of specimens before testing and L is the measured length of specimens during test. The elastic modulus was calculated from the slope of the compressive stress-strain curve in the linear elastic region, while the compressive yield strength was determined from the curve according to the 0.2% offset method.

2.3.6. Nanoindentation analysis

Nanoindentation analysis was performed to determine the elastic modulus (E) and surface hardness (H) of the metal alloys. Testing was conducted using the nano-indenter of our group (APEX, CETR Inc.). According to the Oliver-Pharr methodology, the nanoindentation tests are performed by applying a force to drive an indenter probe into the surface of a sample and then reducing the force to withdraw a probe. The applied load and indenter displacement into the sample are continuously monitored. After experimentation, a load vs. displacement curve was generated from collected data, allowing for the calculation of sample hardness (H) and elastic modulus (E). The tests were performed using a diamond Berkovich indenter probe. In this procedure the polished sample is mounted on a heavy mass and fixed with wax to it. Then a camera microscope is used to align the indentation head next to the sample's surface. After that a computer program performs an automatic standardized test. Test parameters included using the load-controlled feedback mode with a 5 s linear loading to a peak force of 500 mN, a 10 s hold at peak force, and a 5 s linear unloading duration. This measurement system offers a standardized procedure to obtain the measured quantities. The results can be analyzed with a special program (UMT Test Viewer, CETR Inc.) (Figure 2.8).

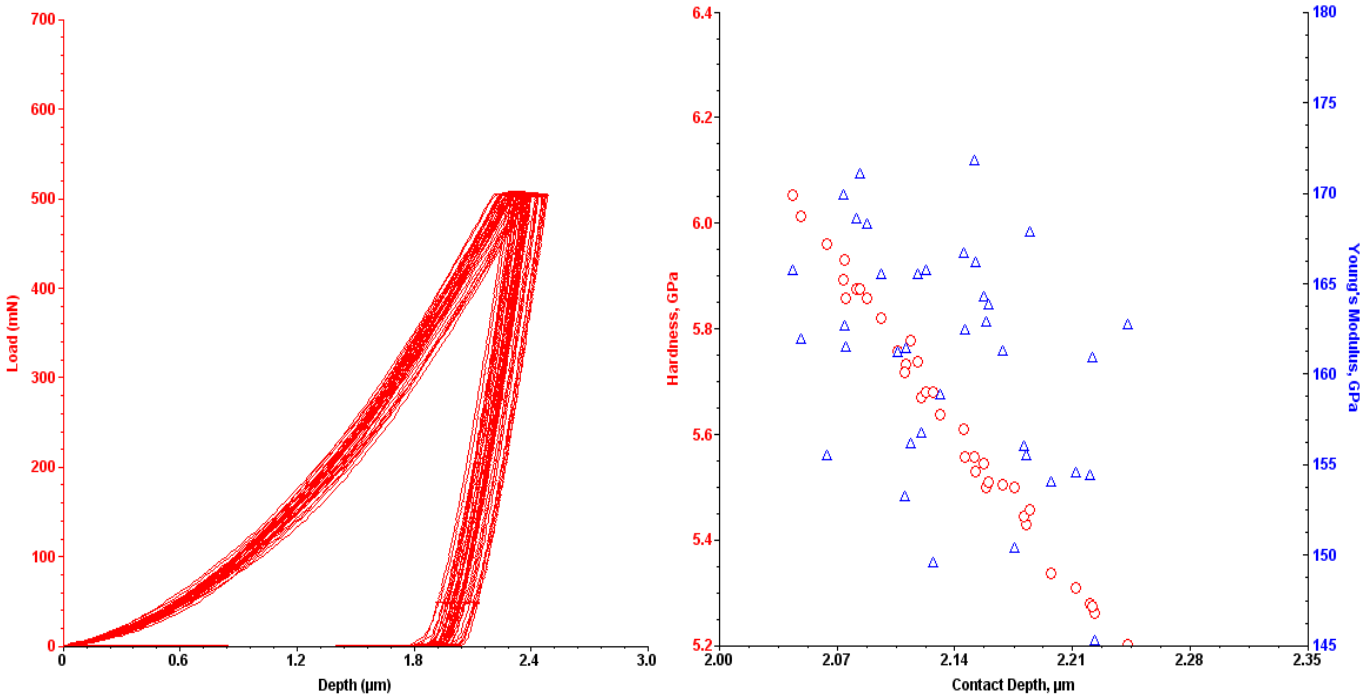

Figure 2.10. An example for the nanoindentation test of the sintered samples.

2.3.7. Scanning electron microscope

With the help of a scanning electron microscope (SEM) it is possible to analyze the microstructure of sample surfaces. By grid-wise scanning the surface with an electron beam of several keV the electron emission is induced. The emitted electrons are counted by a detector point per point and recalculated to an image by a computer. The intensity of the detected secondary electrons is influenced by the topography of the scanned material and its electronic configuration. A detector which detects secondary electrons for images with a high topographical contrast is used. The fracture surfaces after compression tests and the microstructures of the porous Ti alloys were observed using a scanning electron microscope (SEM, Zeiss Supra25, Germany) at 15 kV acceleration voltage.

2.3.8. 3-D micro-focus computed tomography

The porous structure of the sample was analyzed with an X-ray micro-CT (GE, USA). 3-D micro-focus computed tomography is a method that uses x-rays to scan an object from different positions and that reconstructs the three-dimensional internal and external structure of the

specimen by the performed scans. Because the pixel sizes of the recreated images are in the range of micrometers it is called micro CT or high resolution x-ray tomography. In principle it is similar to normal computer tomography used in hospitals. The used micro-CT has a stationary x-ray tube and detector. Therefore the sample is rotated during the examination. The specimens were mounted on a rotary stage and scanned over the whole volume, being rotated by 360° in 1400 equiangular steps (4 pics per 1°). The detector size is 2284 pixel in x and y and 2304 pixel in the z direction. The voxel size of the images is 10.2 um in all three axes.

2.3.9. Cellular acceptance of the surfaces

The human osteoblast-like cell line MG-63 (ATCC, CRL-1427, LGC Promochem, Wesel, Germany) was used for the evaluation of the cellular acceptance of the surfaces [92]. In general, the cells were cultured in Dulbecco's modified Eagle's medium (DMEM) with 10% fetal calf serum (FCS, PAA), and 1% gentamicin (Ratiopharm GmbH, Ulm, Germany) at 37°C in a humidified atmosphere with 5% CO_2. For cell analyses, $1x10^5$ cells were grown on the porous Ti-6Al-4V plates for 24 hours, fixed with 4% glutaraldehyde (1 h), dehydrated through a graded series of acetone, dried in a critical point dryer (K 850, EMITECH, Taunusstein, Germany) and sputtered with a coater (SCD 004, BAL-TEC, Balzers, Lichtenstein). The samples were investigated with a SEM DSM 960A (Zeiss, Germany).

Chapter 03 Ti-6Al-4V synthesized by field assisted sintering technique

3.1. Experimental

3.1.1. Materials

The commercially available Ti-6Al-4V powders were employed in this study, which are prealloyed Ti-6Al-4V (Arcam AB, Sweden) with spherical morphologies and the size distribution of 45 μm–100 μm (Figure 3.1). The chemical composition of the powders is presented in Table 3.1.

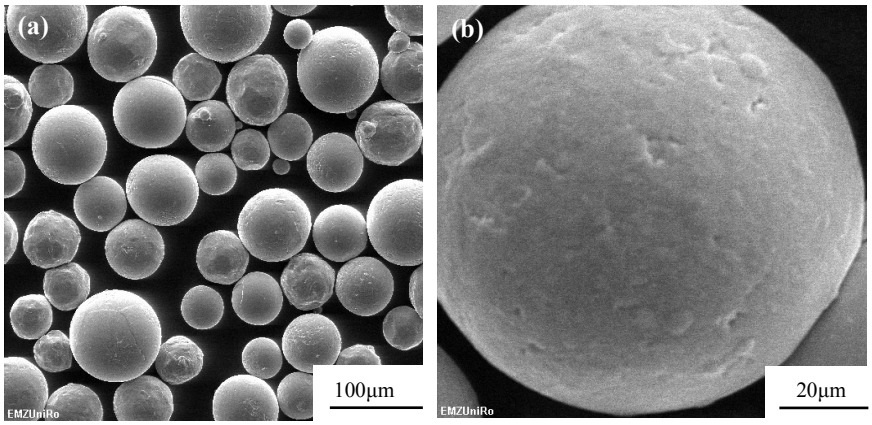

Figure 3.1. Images of the raw Ti-6Al-4V with spherical morphologies (a) and the solidification surface of the bead (b). The size distribution is 45 μm–100 μm.

Table 3.1. Chemical composition of the Ti-6Al-4V alloy.

Chemical composition	Al	V	C	N	O	Fe	H	Ti
Percentages (wt.%)	6.75	4.24	0.03	0.01	0.15	0.17	<0.003	rest

3.1.2. Sample preparation

The field assisted sintering technique (FAST) was performed to synthesize Ti-6Al-4V specimens. This process consists of the sintering of Ti-6Al-4V powders in a cylindrical graphite die under high compaction pressure and subsequent cooling [93]. The applied direct current for the process was 1000 A–2000 A with the pulse duration of 12 ms and an interval of 2 ms. Ti-6Al-4V powders were pressed into a graphite die, and heated under vacuum. A heating rate of 100°C/min was applied, and the sintering process lasted for 6 minutes. As soon as the sintering was finished, argon gas was released into the chamber. After 2 minutes of holding, nitrogen was flowed into the chamber for cooling with different flow speeds. A set-up for obtaining the gas

cooling is shown schematically in Figure 3.2. The system is rotationally symmetric, with six nozzles in one group and eight groups arranged around the sintered component. The core temperature was measured by a central pyrometer and the surface temperature was measured by thermocouples (TC). Continuous monitoring of the temperature–time history during sintering, cooling rate was derived therefrom.

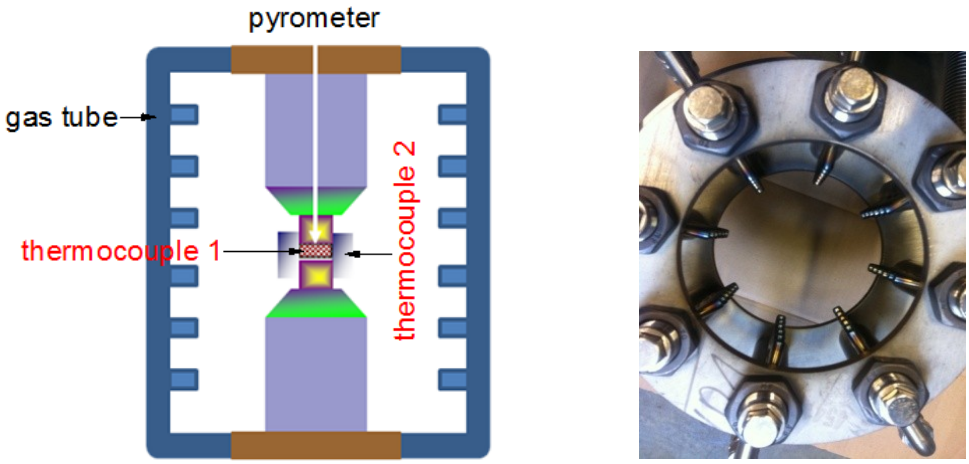

Figure 3.2. Schematic diagram showing the setup for field assisted sintering with gas cooling system (a) and the image of the gas cooling apparatus (b).

The different conditions during sintering were as follows: After preheating powders up to 425˚C, holding at 750˚C, 850˚C, 950˚C, 1050˚C for sintering and the compaction pressures of 30 MPa, 40 MPa, 50 MPa were applied to get the sintered specimens (40 mm diameter, thickness 5 mm–7 mm). The samples were then cooled to room temperature with different cooling procedures, i.e.: furnace-cooling (FC), gas-cooling (GC). Table 3.2 gives an overview of the parameters used in the process.

Table 3.2. Overviews of the field assisted sintering parameters.

Sample No	FC1	FC2	FC3	FC4	FC5	GC1	GC2	GC3	GC4	GC5
Temperature (˚C)	750	850	850	850	950	850	850	750	950	1050
Pressure (MPa)	50	30	40	50	50	50	50	50	50	50
Die thickness (mm)	20	20	20	20	20	20	20	20	20	20

Cooling method	FC	FC	FC	FC	FC	GC2.6K	GC8.0K	GC8.0K	GC8.0K	GC8.0K
Relative density (%)	90.6± 1.0	96.5± 0.8	97.5± 0.6	98.9± 0.4	99.2± 0.7	98.8± 0.5	98.9± 1.0	89.5± 0.5	99.0± 0.4	99.3± 0.3

FC: furnace cooling; GC2.6k: gas cooling with a nitrogen flow speed of 2600 l/min; GC8.0k: gas cooling with a nitrogen flow speed of 8000 l/min. Relative density is represented as mean ± standard deviation.

3.2. Results

3.2.1. Synthesis of Ti-6Al-4V alloy

Figure 3.3 shows the calculated relative density as a function of sintering pressure and temperature. The relative density increases with the rise of sintering temperature and pressure. It is found that the relative densities of samples sintered at 850°C, 950°C with 50 MPa compaction pressure are nearly 99% of the theoretical density (Table 3.2). Therefore, the pressure of 50 MPa was routinely applied throughout the study.

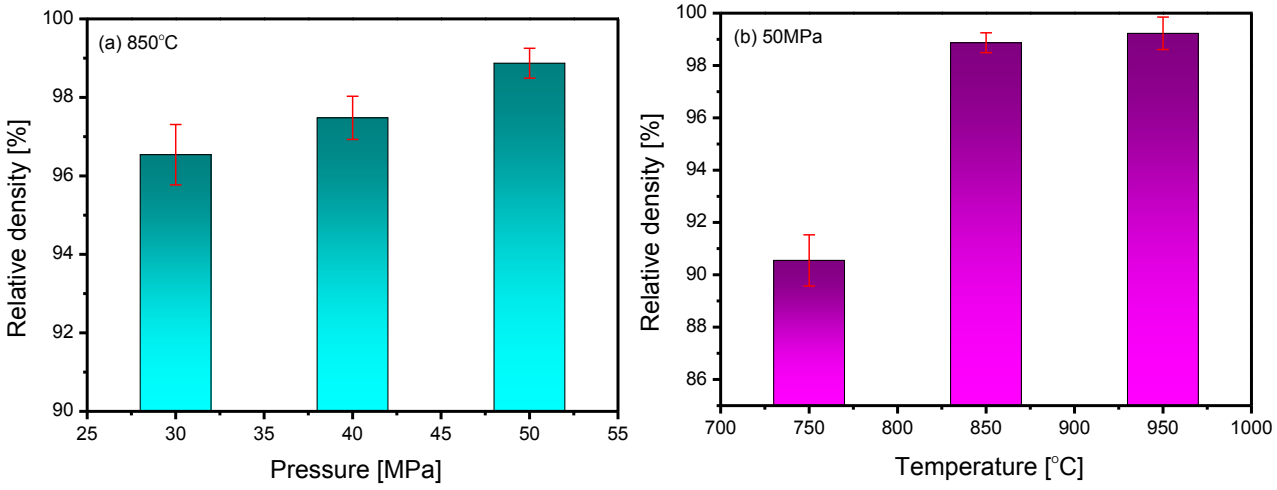

Figure 3.3. Calculated relative density as a function of sintering pressures (a) and temperatures (b) with furnace cooling.

Figure 3.4 shows the temperature–time curves of the field assisted sintered Ti-6Al-4V alloy with various cooling procedures. The red and the blue lines show the temperature values from thermocouples and the black line shows values from the pyrometer above 400°C. The average cooling rates were derived by taking the cooling time from 850°C to 400°C into account.

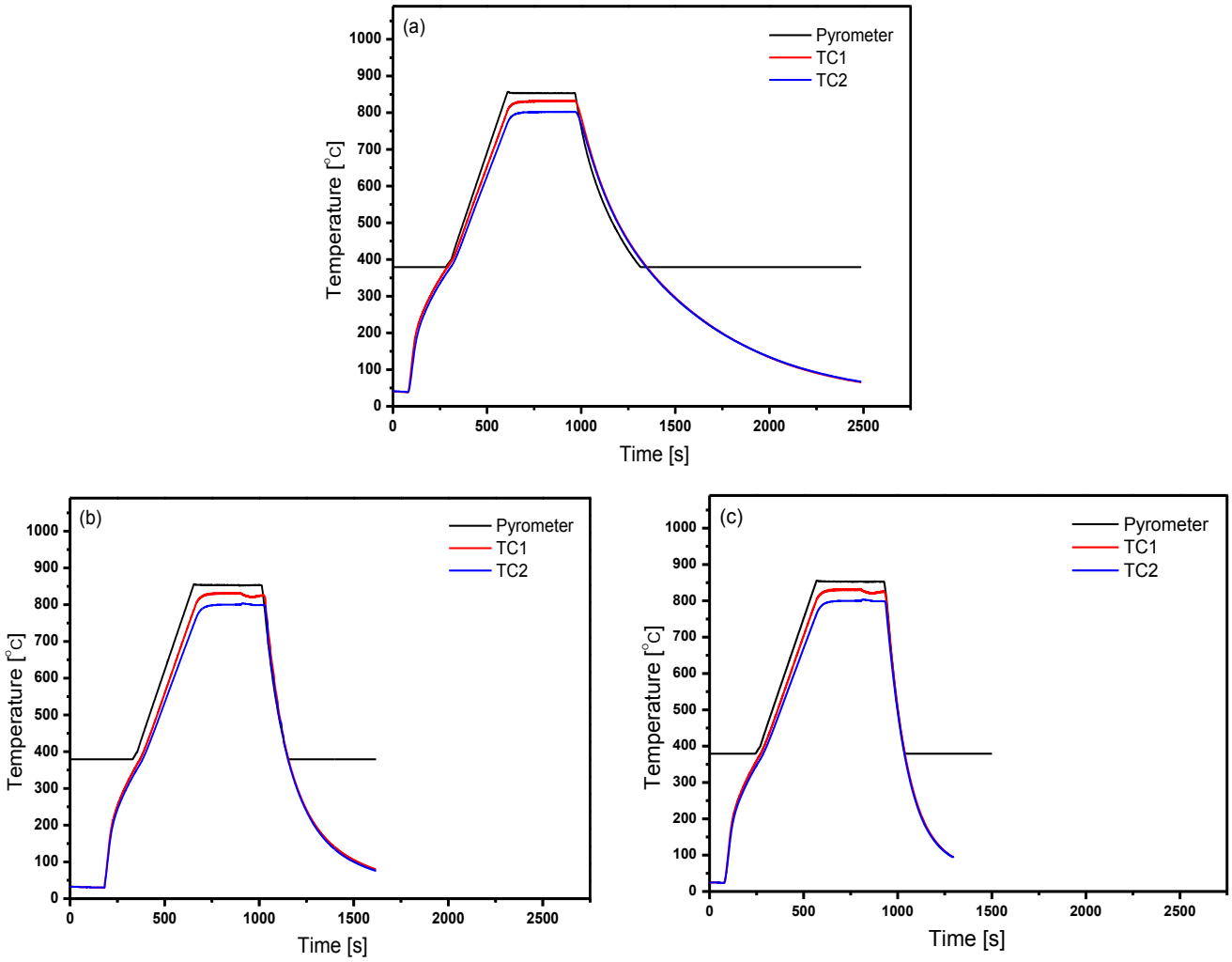

Figure 3.4. Representative temperature–time curves for Ti-6Al-4V sintered at 850°C with different cooling regimes: (a) furnace cooling (FC4); (b) 2600 l/min gas cooling (GC1); (c) 8000 l/min gas cooling (GC2).

The comparison of the cooling curves is shown in Fig. 3.5. From the cooling curves, the cooling rate of 1.55°C/s is achieved with a 20 mm thick graphite die and furnace cooling, 3.54°C/s and 4.78°C/s are obtained with 2600 l/min and 8000 l/min nitrogen gas cooling, respectively.

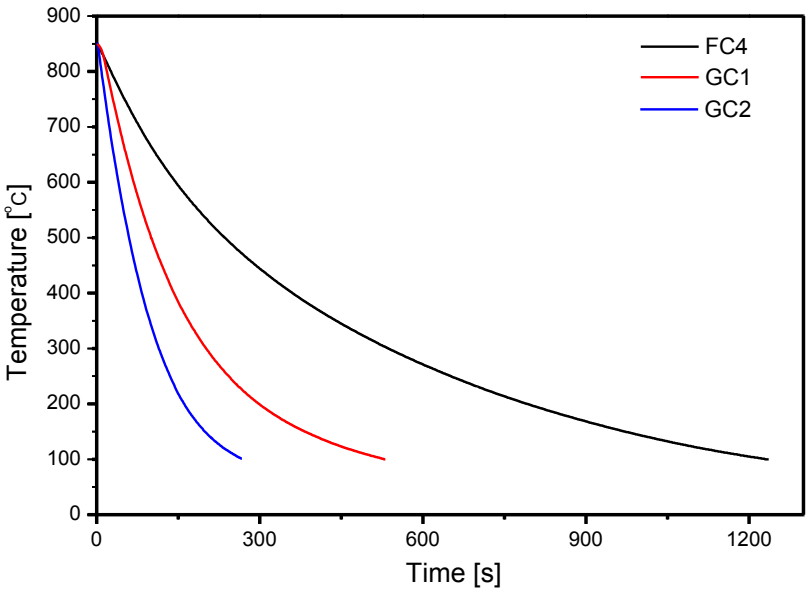

Figure 3.5. Representative cooling curves for Ti-6Al-4V sintered at 850°C with varied cooling rates. Cooling rates are: 1.55°C/s (FC4), 3.54°C/s (GC1) and 4.78°C/s (GC2), respectively.

3.2.2. X-ray diffraction analysis

Figure 3.6 shows the diffraction images of Al_2O_3 standard and Ti-6Al-4V alloy with Debye rings corresponding to reflections on h k l lattice planes. Debye rings are smooth, indicating excellent grain statistics, which is a prerequisite for a quantitative analysis with the Rietveld method. The recalculation of X-Ray diffraction data was performed by assuming ideal structures of materials except where the microstructures and scale factors were refined as a part of the Rietveld analysis. For diffraction data a square root scale for intensity was used, as smaller peaks were more visible. The comparison of experimental and fitted spectra can be viewed with the "Plot 2D" tab in which all individual patterns are displayed (Figure 3.7). This image is after instrument correction refinement and diffractions appear as straight lines.

An example of the Rietveld analysis for the Ti-6Al-4V powders is given in Figure 3.8. Because of the high quality data obtained using the synchrotron source, it is possible to identify the small amount of β-phase. The agreement factors as well as the visual inspection of the fitting resulted in a good fit, with R-factor and goodness-of-fit indicator being: Rw=8.18, sig=1.55. According to the X-ray analysis, the weight ratio of the α- and β-phases amounts to 97.6% and 2.4%, respectively. The crystal lattice parameters for the α-phase are: a_α=2.925 Å, c_α=4.669 Å and for the β-phase: a_β=3.189 Å.

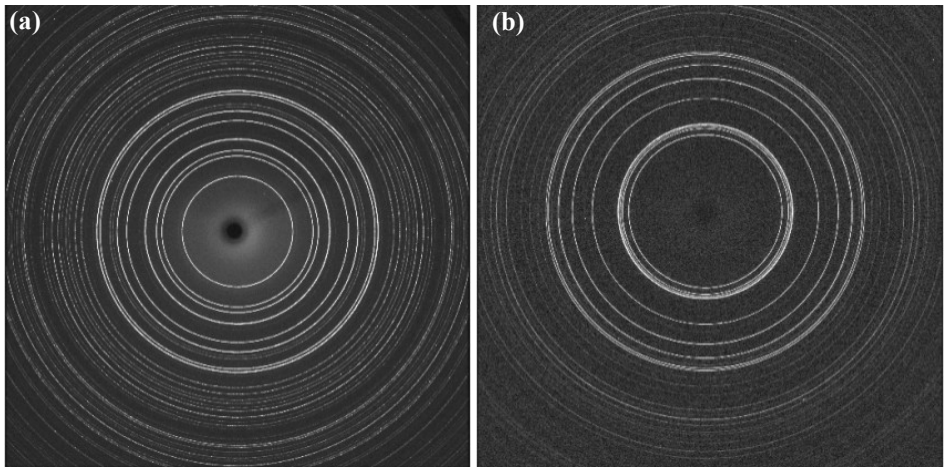

Figure 3.6. Diffraction images with Debye rings measured at Desy: Al_2O_3 standard (a), Ti-6Al-4V alloy (b).

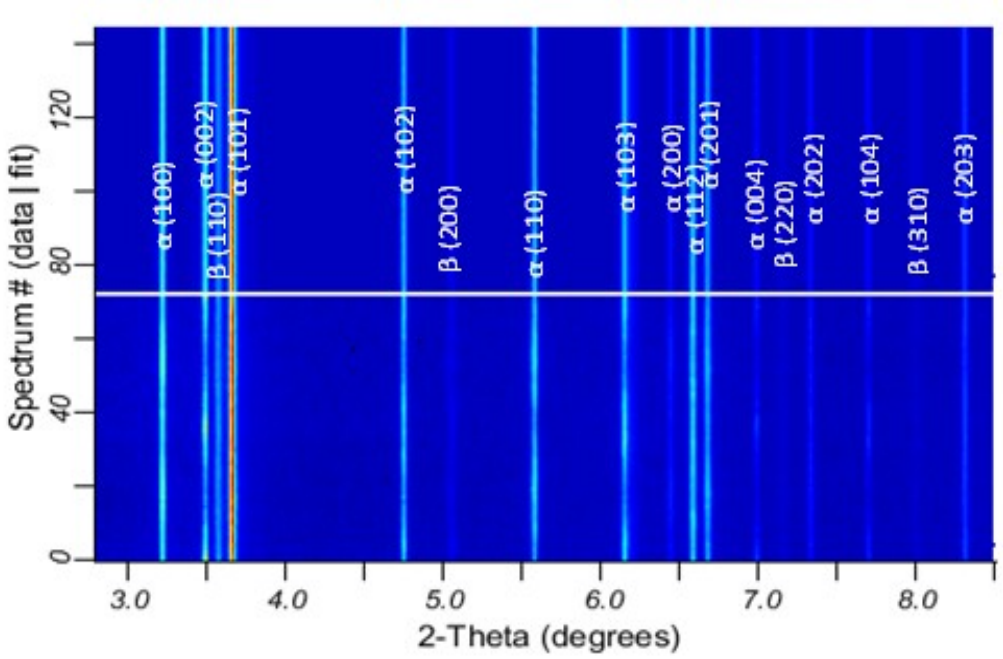

Figure 3.7. Experimental (bottom) and calculated diffraction patterns (top) for Ti-6Al-4V at the end of refinement. After refinement of detector, Plot2D display, diffraction lines are straight. Lattice plane indices are indicated.

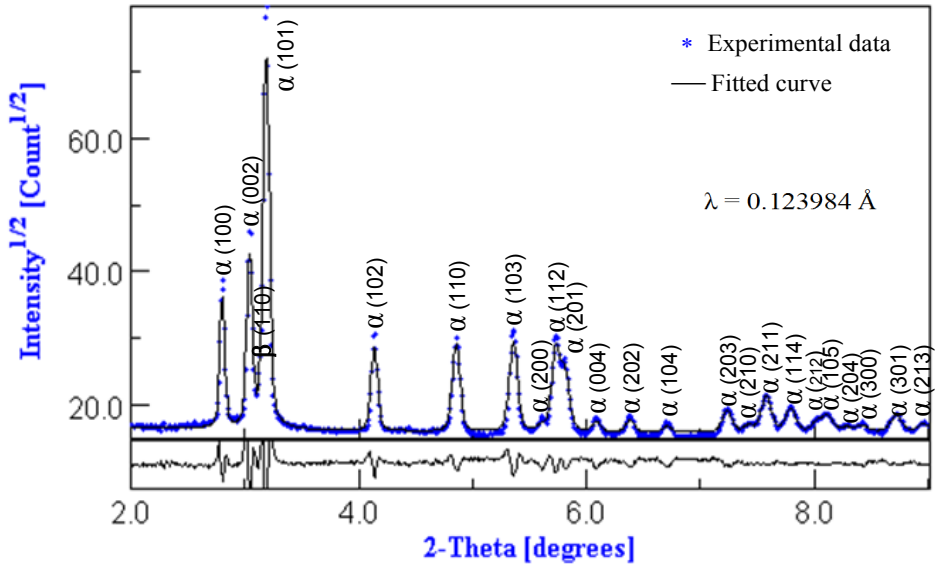

Figure 3.8. Rietveld analysis, using synchrotron data, for the Ti-6Al-4V powders. The residual of fitting is indicated below the graph. The fitted parameters are: α=97.6 wt.%, β=2.4 wt.%, Rw=8.18, sig=1.55. Notes: Rw: weighted residual error, sig: goodness of fit.

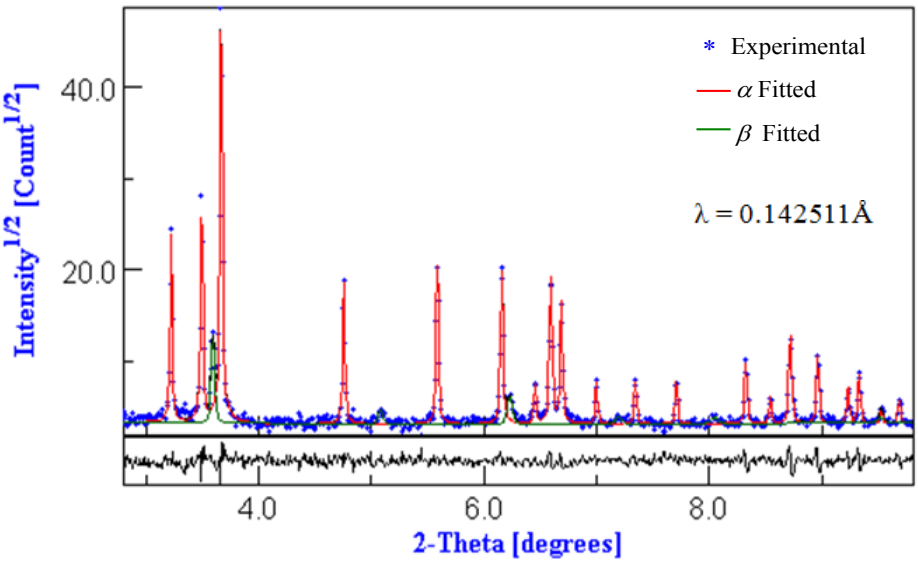

Figure 3.9. Rietveld analysis for the Ti-6Al-4Valloy sintered at 850°C, where the peaks of β-phase can be observed. α=94.8%, β=5.2%, Rw=15.24, sig=1.08. Rw: weighted residual error, sig: goodness of fit, proportion of phases in wt.%.

The X-ray diffraction patterns of samples sintered at 850°C and furnace-cooled and gas-cooled are shown in Figure 3.10. Reflections of the α- and β-phases are detected in the diffraction patterns of all samples. The furnace-cooled sample shows weak diffraction peaks from the β-Ti lattice plane (110). The gas-cooled Ti-6Al-4V specimens exhibit sharper diffraction peaks corresponding to the β-phase. It should be noted that the β-reflections are rather weak, suggesting a relatively low fraction of β-phase. The intensity of the β-reflections increases with increasing the cooling rate, which indicates the increase of the β-fraction.

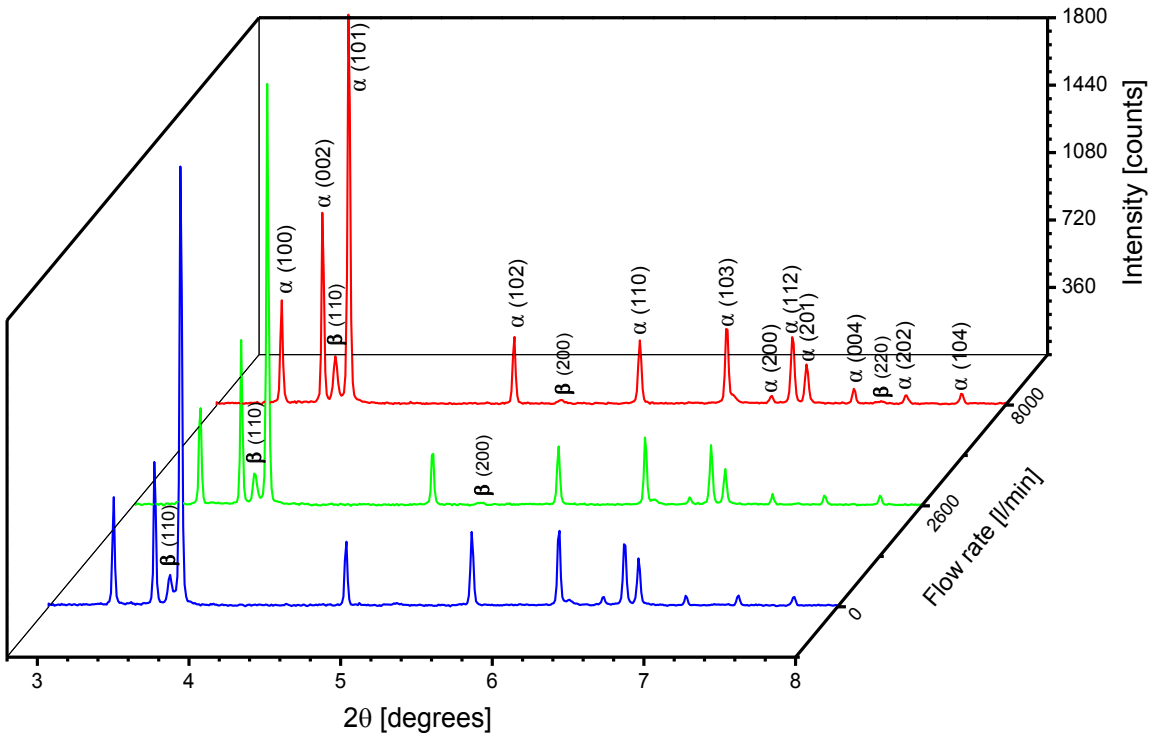

Figure 3.10. X-ray diffraction patterns of Ti-6Al-4V samples sintered at 850°C after cooling with different cooling rates. Cooling rates are: 1.55°C/s (FC4), 3.54°C/s (GC1) and 4.78°C/s (GC2), respectively. λ=0.142511 Å.

Figure 3.11 shows a comparison of the average crystallite size for the sintered samples derived from the recalculation of X-ray diffraction patterns, when the one obtained from Ti-6Al-4V powders included. After Rietveld refinement, the crystallite size is characterized in a range of 295 nm–349 nm. It is found out that decreasing the cooling rate leads to the growth of crystallite size.

The plot of the phase fraction versus the cooling rate is shown in Figure 3.12. The error bar is determined by the Rietveld refinement. The plot demonstrates that the phase fraction varied with different cooling rates. The Ti-6Al-4V powder has a weight fraction of (97.6±0.6) wt.% for the

α-phase and (2.4±0.2) wt.% for the β-phase. The furnace cooled sample with a cooling rate of 1.55˚C/s has (94.8±0.5) wt.% α-phase and (5.2±0.8) wt.% β-phase. The gas cooled samples exhibit a fraction of (93.8±1.0) wt.% α-phase and (6.3±0.8) wt.% β-phase for the cooling rate of 3.54˚C/s, (92.7±0.8) wt.% α-phase and (7.4±0.9) wt.% β-phase for the cooling rate of 4.78˚C/s, respectively.

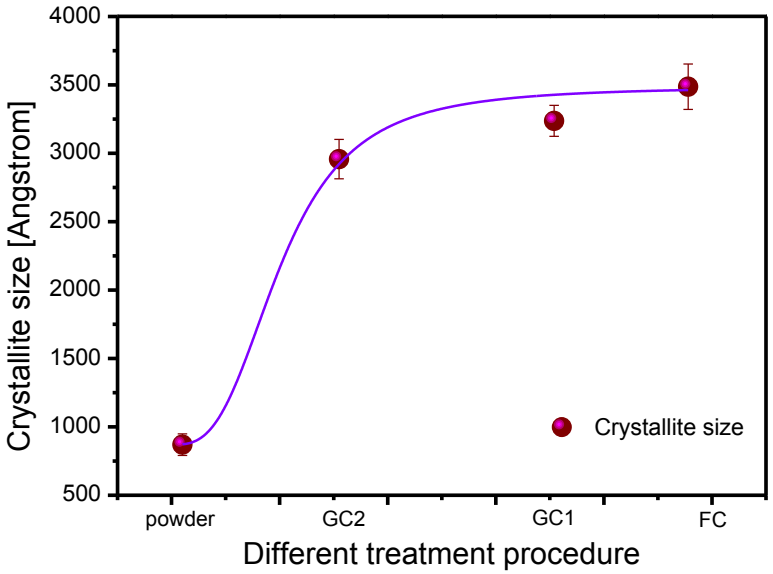

Figure 3.11. Effect of the cooling rate on the α-crystallite size of Ti-6Al-4V alloys. FC4: sintered at 850˚C with a furnace cooling (1.55˚C/s); GC1: sintered at 850˚C with a gas cooling flow of 2600 l/min (3.54˚C/s); GC2: sintered at 850˚C with a gas cooling flow of 8000 l/min (4.78˚C/s).

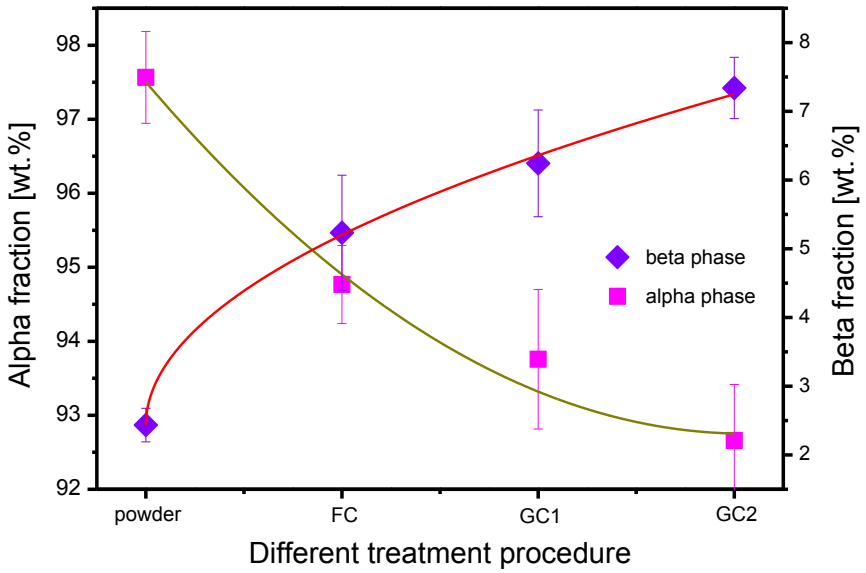

Figure 3.12. Effect of cooling rate on the phase fraction of Ti-6Al-4V alloys. Powder: raw powder; FC4: sintered at 850˚C with furnace cooling (1.55˚C/s); GC1: sintered at 850˚C with gas cooling flow of 2600 l/min (3.54˚C/s); GC2: sintered at 850˚C with gas cooling flow of 8000 l/min (4.78˚C/s).

In Table 3.3, the values of crystal lattice parameters and phase fraction in titanium alloys after sintering at 850°C with different cooling rates are given. The α-phase crystallite size increases from (2957±344) Å to (3486±265) Å while the cooling rate decreases from 4.78°C/s to 1.55°C/s. The weight fraction of the α-phase decreases from (94.8±0.5) wt.% to (92.7±0.8) wt.% with increasing cooling rate, whereas in the opposite case the β-phase fraction increases from (5.2±0.8) wt.% to (7.4±0.9) wt.%. Compared with the cell parameters of Ti-6Al-4V powder, the sintered samples show that the unit-cell of the β-phase increasing and the unit-cell of the α-phase decreasing, although not so significantly.

Table 3.3. Rietveld refinement results of present phases upon different treatment procedures (850°C).

Sample	Crystallite size (Å)	α fraction (wt.%)	β fraction (wt.%)	Cell length a_α (Å)	Cell length c_α (Å)	Cell length a_β (Å)
Powder	869 ± 178	97.6 ± 0.6	2.4 ± 0.2	2.925	4.669	3.189
FC4	3486 ± 265	94.8 ± 0.5	5.2 ± 0.8	2.922	4.668	3.210
GC1	3237 ± 212	93.8 ± 1.0	6.3 ± 0.8	2.923	4.669	3.221
GC2	2957 ± 344	92.7 ± 0.8	7.4 ± 0.9	2.923	4.669	3.226

FC4: sintered at 850°C with furnace cooling (1.55°C/s);
GC1: sintered at 850°C with gas cooling flow of 2600 l/min (3.54°C/s);
GC2: sintered at 850°C with gas cooling flow of 8000 l/min (4.78°C/s).

X-ray diffraction patterns of Ti-6Al-4V samples sintered at different temperatures after gas cooling with a flow speed of 8000 l/min are shown in Figure 3.13. For all specimens, the XRD patterns are comprised of the same diffraction peaks indicating the α-Ti and β-Ti phases. The α-phase is the dominant phase in the Ti-6Al-4V alloys after the FAST process. Starting at 750°C, a small amount of residual β-phase is detected. During the second sample at sintering temperature equals to 850°C, the β-phase peaks (110) and (200) are observed. Gradually, Ti-6Al-4V samples sintered at higher temperatures present higher β-phase peaks. Since some peaks of the β-phase coincide with peaks of the α-phase, asymmetry of peak shapes is observed.

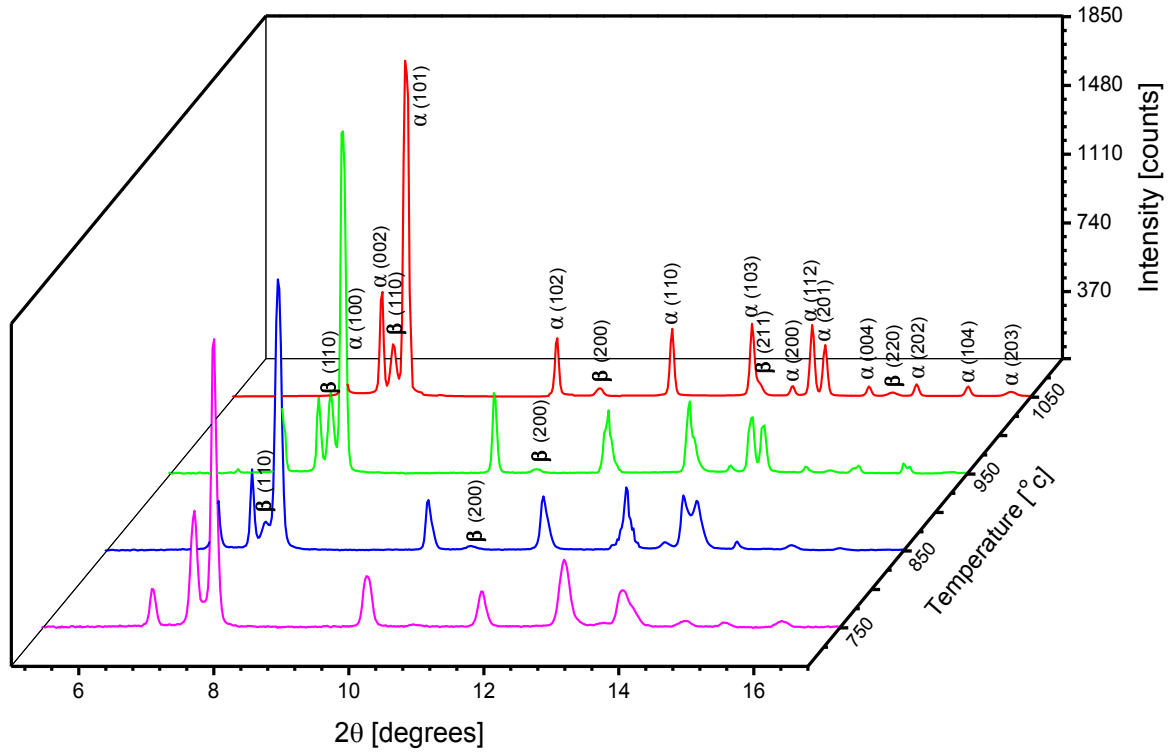

Figure 3.13. X-ray diffraction patterns of Ti-6Al-4V samples sintered at different temperatures after cooling with a flow speed of 8000l/min. λ=0.029118 Å.

Figure 3.14 shows the effect of sintering temperatures on the α-crystallite size of Ti-6Al-4V alloys. When compared with the ones obtained at lower temperature, the crystallite size of α-phase increases with increasing temperature. Table 3.4 shows the results of quantitative analyses for the sintered samples. The weight fraction of the α-phase is reduced with increasing temperature for the samples processed between 750°C and 950°C. The value varies from (94.8±0.9) wt.% to (88.9±1.4) wt.% and the content of the β-phase ranges up from (5.3±0.8) wt.% to (10.9±1.3) wt.%. The sample sintered at 1050°C exhibits a β-phase fraction of (9.8±1.6) wt.%, which is lower than that at 950°C. In all samples investigated, the crystallite size is found to be increased from 1886 Å to 7426 Å with increasing temperatures.

Table 3.4. Rietveld refinement results of present phase upon different sintering temperature.

Temperature (°C)	Crystallite size (Å)	α fraction (wt.%)	β fraction (wt.%)
750	1886 ± 243	94.8 ± 0.9	5.3 ± 0.8
850	2957 ± 344	92.7 ± 0.8	7.4 ± 0.9
950	5753 ± 552	88.9 ± 1.4	10.9 ± 1.3
1050	7426 ± 877	90.6 ± 1.8	9.8 ± 1.6

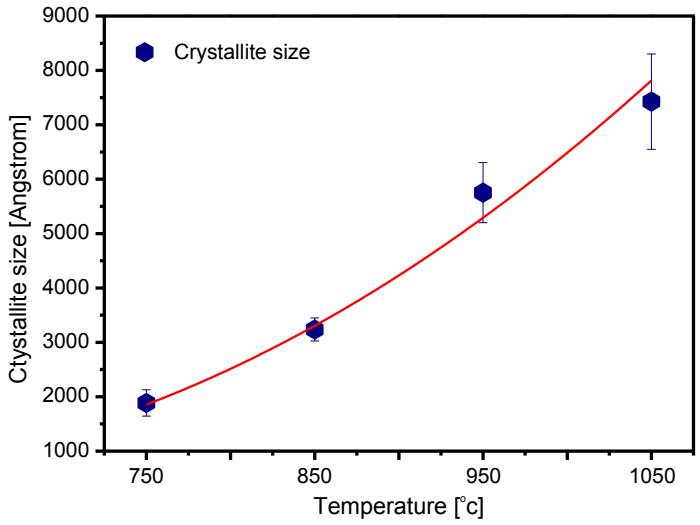

Figure 3.14. Effect of the sintering temperature on the α-crystallite size of Ti-6Al-4V alloys.

3.2.3. Metallographic examination

Figure 3.15 shows the microstructures of Ti-6Al-4V samples sintered at different temperatures with varied sintering pressures. Initial bonding between particles and neck formation appears at 750°C, but the main evolution occurs at 850°C between 30 MPa and 40 MPa compaction pressures with the particles get closer to each other and the porosity is highly reduced. After sintered at 850°C with the pressure of 50 MPa, a well densified Ti-6Al-4V alloy obtained, when the separate original particles diffuse to the neighbors.

The microstructures of the alloys sintered at 850°C with controlled cooling rates are presented in Figure. 3.16. The microstructure developed by the furnace cooling at the rate of 1.55°C/s consists of the α-colonies within the prealloyed Ti-6Al-4V particles and equiaxed α-phase at the boundary of particles. Increasing the cooling rate (4.68°C/s) leads to the reduction of thickness and length for the α-plates.

Similar microstructures are obtained upon gas cooling from 950°C, except that the size of the α-plates is bigger since the sintering temperature is higher (Figure 3.17). Also, furnace-cooling produces thicker α-plates than gas-cooling sintering at the same temperature.

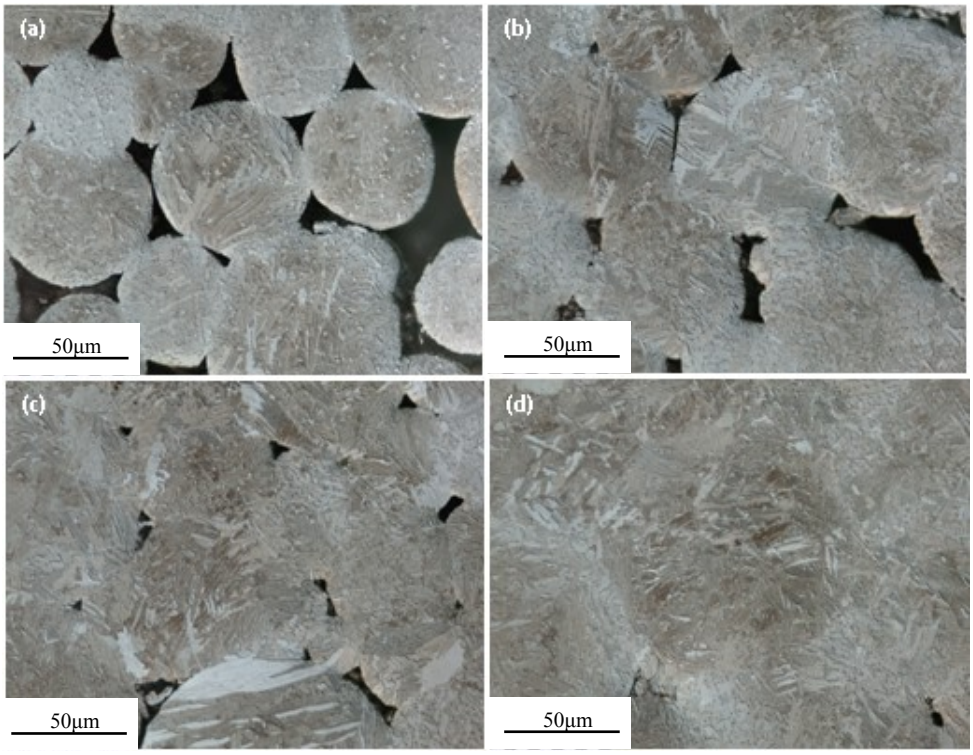

Figure 3.15. Microstructures of Ti-6Al-4V alloys sintered at different temperatures and varied compaction pressures after furnace cooling: "soft" agglomeration of Ti-6Al-4V particles sintered at 750°C with a compaction pressure of 50 MPa (a); forming a "hard" agglomeration at 850°C, 30 MPa (b) and 850°C, 40 MPa (c); "hard" agglomeration of Ti-6Al-4V particles sintered at 850°C with the compaction pressure of 50 MPa (d).

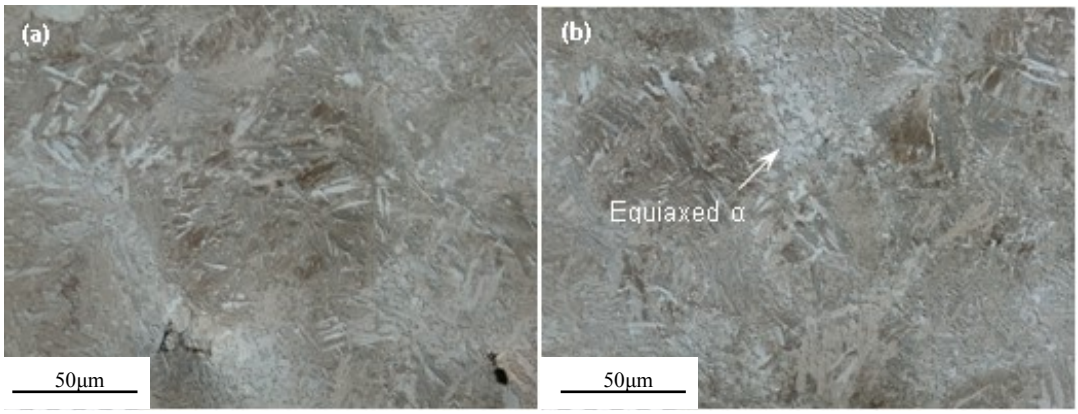

Figure 3.16. Microstructures of Ti-6Al-4V alloys after heating to 850°C and cooling to room temperature at different cooling rates:1.55°C/s (a), 4.68°C/s (b). Optical micrograph shows equiaxed α-phase present on the particle boundary. The intra-particles microstructure is composed of long parallel α-plates and retained β between the plates.

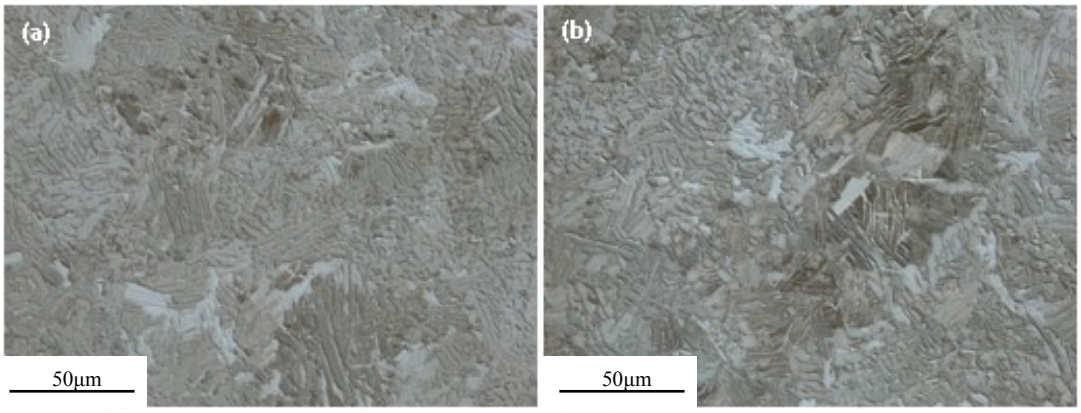

Figure 3.17. Microstructures of Ti–6Al–4V alloys after heating to 950°C and cooling to room temperature at different cooling rates: 1.55°C/s (a), 4.68°C/s (b). The thickness of α-plates increases with decreasing cooling rate.

Figure 3.18 shows the microstructures of Ti-6Al-4V alloys sintered at different temperatures. After gas cooling from 1050°C, Widmanstätten prevails in the microstructure (Figure 3.18(c)). Plates of α-phase with some retained β-phase are present in the sample sintered at 950°C, whereas gas cooling from 850°C produces a bimodal structure with α-phase colonies at pre-existing particle interior and equiaxed α-phase formed at boundaries. It is noticed that the thickness and lengths of the α-plates increases with raised temperature.

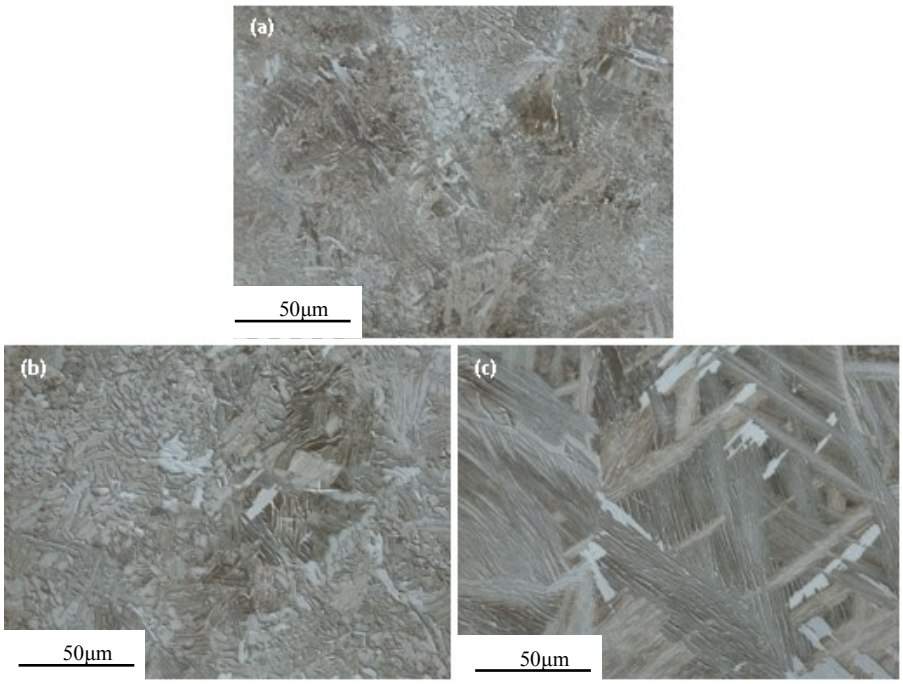

Figure 3.18. Microstructures of Ti-6Al-4V alloys sintered at different temperatures ((a) 850°C, (b) 950°C and (c) 1050°C) and nitrogen gas cooled with a flow speed of 8000 l/min. The size of α-plates increases with increasing sintering temperature. A Widmanstätten α-structure being observed.

3.2.4. Nanoindentation measurement

Table 3.5 summarizes the results of nanoindentation measurements. The alloy sintered at 850°C with furnace cooling has a lower elastic modulus than those of specimens after gas cooling. Notably, the alloy formed at 1050°C is revealed to possess higher (E) and (H) values than other metal alloys.

Table 3.5 Nanoindentation results for the Ti-6Al-4V specimens.

Specimens NO	FC4	GC1	GC2	GC4	GC5
Surface hardness (GPa)	4.5 ± 0.7	4.4 ± 0.9	4.6 ± 0.6	4.5 ± 0.8	4.8 ± 0.9
Elastic modulus (GPa)	132 ± 12	144 ± 17	143 ± 13	143 ± 17	145.4 ± 19

Data is represented as mean ± standard deviation.

3.2.5. Compression fracture analysis

After compressive tests, fracture features were examined by scanning electron microscopy. Figure 3.19 shows the fracture views of the specimens after furnace cooling with different sintering temperatures and varied compaction pressures. Fracture behavior shows ductile characteristics as displayed by the presence of dimples. In the sample sintered at 750°C, pores are identified. In Figure 3.19 (b) and (c), a lack of connection between raw prealloyed particles is observed. The specimen synthesized at 850°C with 50 MPa pressure displays good interparticle connection.

The fracture surfaces for the samples after gas cooling with different rates are shown in Figure 3.20. It can be seen that elongated dimple patterns are distributed on the fracture surfaces, which is an indicative of sheared loading. Some small dimples between large dimples are observed from the microstructure of Figure 3.20 (b). The fracture surface in Figure 3.20 (d) shows the dimples with a deeper ductile aspect. As the cooling rate was raised, Figure 3.20 (e) and (f), an increase of the dimple size is observed.

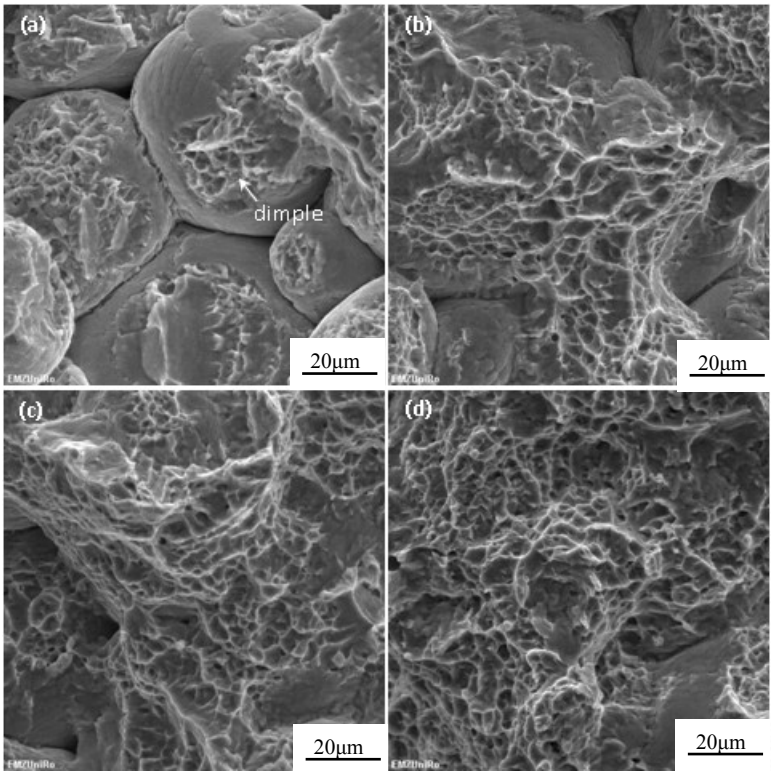

Figure 3.19. Views of fracture features for the Ti-6Al-4V sintered at different procedures: (a) 750°C, 50 MPa; (b) 850°C, 30 MPa; (c) 850°C, 40 MPa; (d) 850°C, 50 MPa. Fracture through interpaticle necks is clearly seen and the figures show the occurrence of ductile fracture known as dimples.

Also the fracture surfaces from samples with different sintering temperatures were investigated by SEM, as reported in Figure 3.21. The surfaces are covered by dimples, clearly visible only at higher magnification. There are many microvoids on the fracture surface for the specimen sintered at 850°C, which display an elongated shape oriented in the ductile crack propagation direction. From Figure 3.21 (d), the fracture surface exhibits shallower dimples and larger average dimple size when compared to those at Figure 3.21 (b). For the higher temperature (1050°C) sintered material, the size of dimple is reduced once more (Figure 3.21 (f)).

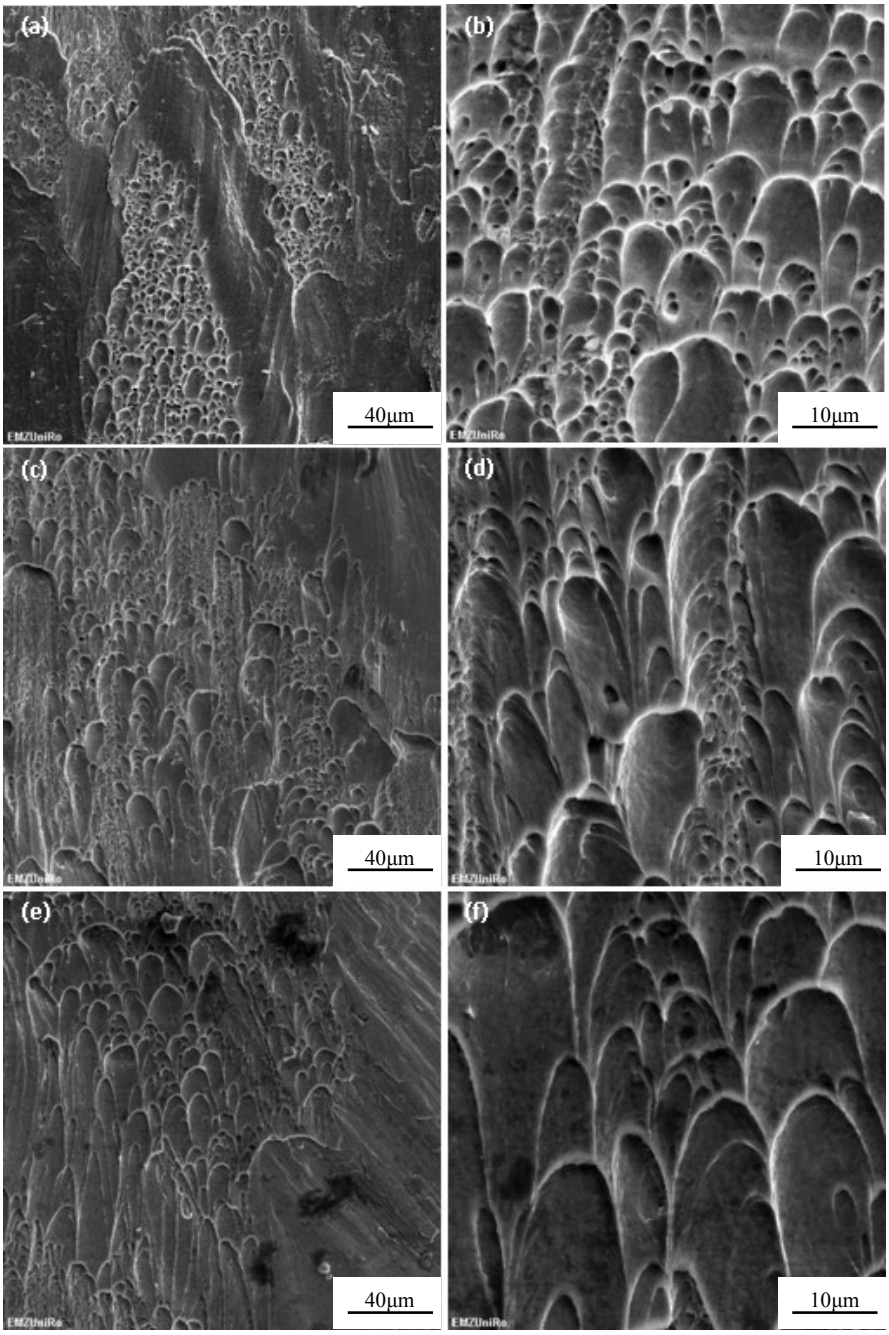

Figure 3.20. Fracture surface of the Ti-6Al-4V specimen sintered at 850°C with a cooling rate of 1.55°C/s (a) and (b) the enlarged image of the dimple region in (a); Fracture surface of the specimen sintered at 850°C with a cooling rate of 3.54°C/s (c) and (d). (e) and (f) are the fracture images of specimen sintered at 850°C with a cooling rate of 4.68°C/s. Presence of dimples characteristic of ductile fracture demonstrates a highly ductile fracture in Ti-6Al-4V alloy.

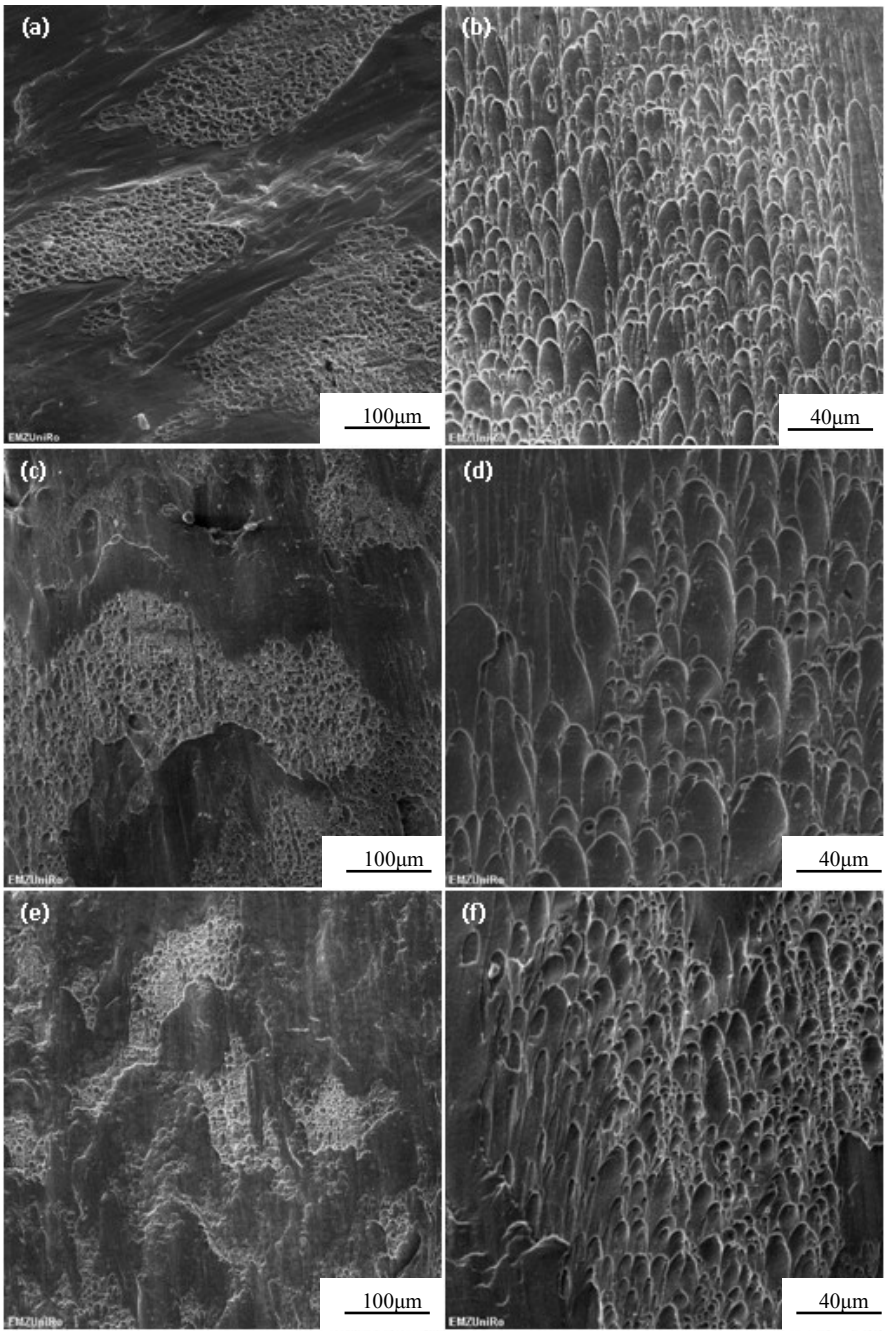

Figure 3.21. Fracture surface of the Ti-6Al-4V specimen sintered at 850°C (a) and (b) the enlarged image of the dimple region in (a); Fracture surface of the specimen sintered at 950°C (c) and (d); (e) and (f) are the fracture images of specimen sintered at 1050°C.

3.2.6. Compressive mechanical properties

Typical true stress-strain curves obtained from compression tests are compared in Figure 3.22. It is noted that for all the test samples, after the yield strength is reached, the curve firstly is of a parabolic shape and then becomes linear under a specific work-hardening rate. At 750°C sintering temperature, the yield strength is presently at (606±34) MPa due to the weak bonding between raw particles. In comparing these curves with one another, it is seen that the increase of temperature and compaction pressure has a very pronounced effect on the magnitude of the yield strength. Compressive elongation changes in the same manner, on the other hand, elongation increases with both sintering temperature rise and compaction pressure increment.

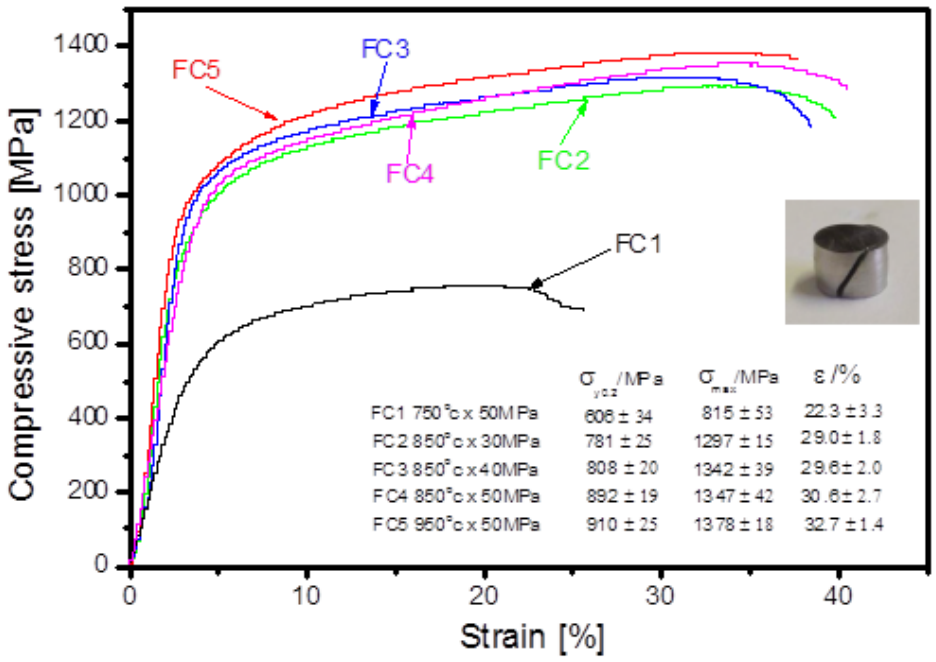

Figure 3.22. Compressive true stresss-strain curves for samples sintered at different treatment regimes. Inset is the side view of the fracture feature from the specimen deformed at room temperature. Data is represented as mean ± standard deviation.

Figure 3.23 displays true stress-strain curves for the sintered specimens upon compressive loading, in which a curve obtained from the specimen with furnace cooling is included in order to compare the cooling rate effect. For gas-cooled Ti-6Al-4V alloys, the yield strengths are superior to those cooled with furnace cooling. The highest strength of the alloy, about (936±14)

MPa, is obtained from the specimen (GC2) synthesized at 850°C and cooled in nitrogen gas with a flow speed of 8000 l/min. The lowest strength, about (892±19) MPa, accompanied with the lowest elongation of (30.6±2.7)%, is obtained when the alloy (FC4) was produced at 850 °C upon furnace cooling. The elongation at failure for GC4 ((33.2±1.9)%) and GC2 ((32.4±1.7)%) are comparable to the GC1 ((31.8±2.0)%). As the sintering temperature was reached to 1050°C, a little decrease of elongation is observed for GC5 ((31.1±2.3)%).

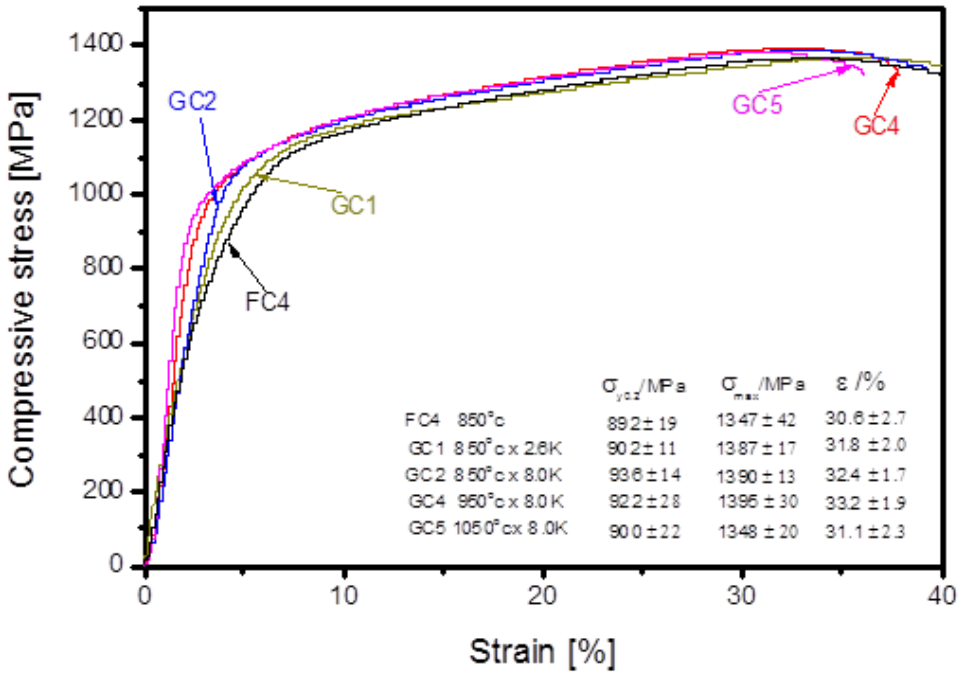

Figure 3.23. Compressive true stress-strain curves for samples sintered at different treatment regimes. Data is represented as mean ± standard deviation.

Changes of yield strengths for the specimens sintered at 850°C with different cooling rates are shown in Figure 3.24. In general, the yield strength increases with increasing cooling rate, being highest with the nitrogen cooling rate of 4.68°C/s. The strength of (902±11) MPa was obtained for the specimen sintered at 850°C with the cooling rate of 3.54°C/s, whereas upon furnace-cooling the lowest strength value ((892±19) MPa) was registered.

Figure 3.25 shows the effect of the sintering temperature on the compressive yield strength of Ti-6Al-4V alloys. It clearly indicates that the material has a low rate of decrease in the yield strength with increasing temperature.

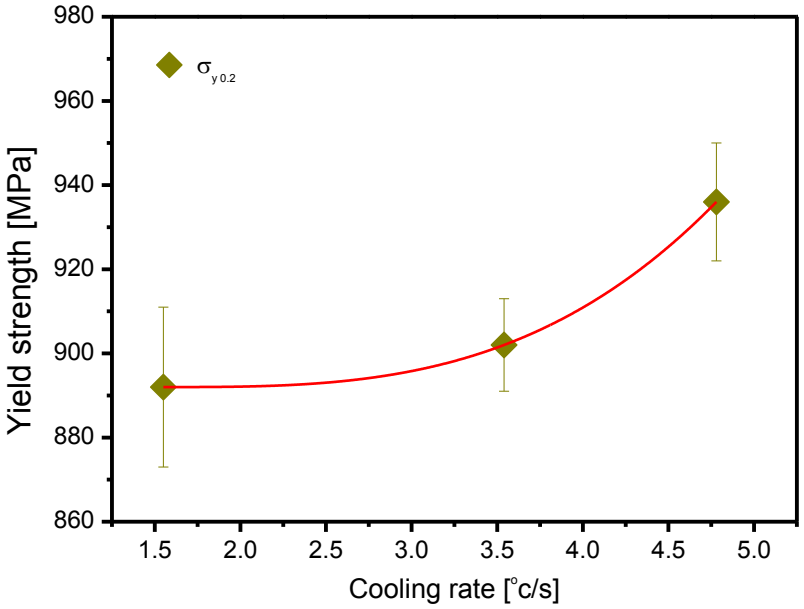

Figure 3.24. Effect of the cooling rate on the compressive yield strength of Ti-6Al-4V alloys.

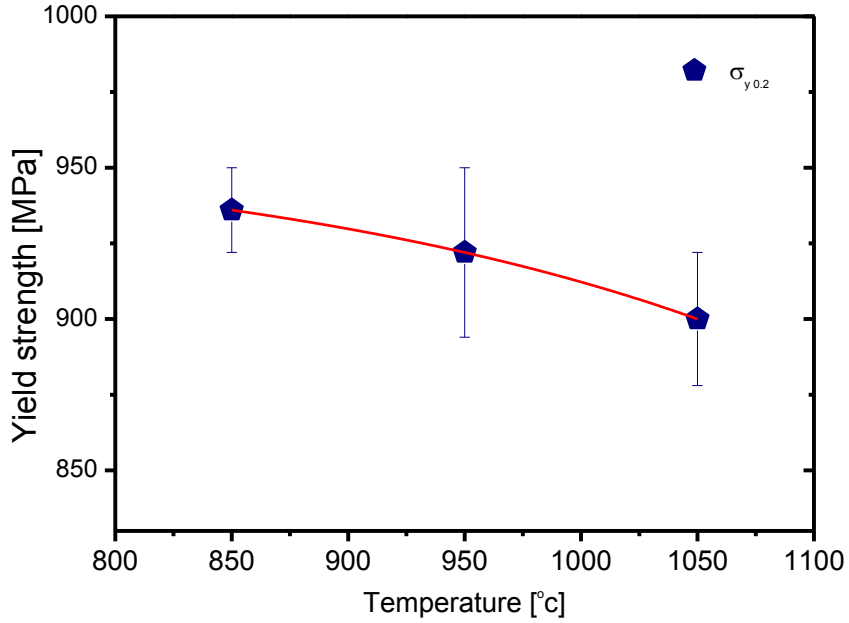

Figure 3.25. Effect of the sintering temperature on the compressive yield strength of Ti-6Al-4V alloys.

3.3. Discussion

3.3.1. X-ray diffraction

As shown in Figure 3.8, some residual of β-phase is observed in the case of the sample sintered at 850°C with furnace cooling. Applying Rietveld refinement for all the specimens produced after different cooling rates, the results are summarized in Table 3.3. According to the data, lattice parameters for the α-phase are: α_a=(2.923±0.001) Å, α_c=(4.669±0.001) Å and β_a=(3.219±0.008) Å for the β-phase, which are slightly bigger than that of prealloyed powders. The observed deviations can be accounted for substitutions among cations that were changed in the sintering process. The relative intensities of the peaks of β-phase are different in Figure 3.10. With cooling rates varied for 1.55°C/s to 4.68°C/s, the β-phase amount is in the range of 2.4 wt.%–7.4 wt.%. This indicates that the fast cooling delayed the phase transformation in the sintered alloy. After field assisted sintering, the β-phase cannot transform to the α-phase completely. There are some discrepancies compared to the published results for Ti-6Al-4V [94]. According to the reference, the amount of residual β-phase was independent of the cooling rate. The difference might be due to the variation in the composition of the alloy used and the accuracy of the X-ray diffraction. Refinement errors may also yield some changes between the results.

Quantitative analyses were performed on the diffraction data of the samples sintered at different temperatures. The results are exposed in Table 3.4. The crystallite size of the α-phase increases when the temperature rising from 750°C to 1050°C. The similar situation for the β-phase fraction is experienced upon sintering temperature changing from 750°C to 950°C, i.e., the weight fraction of the β-phase increases from 5.3 wt.% to 10.9 wt.% and the presence of the α-phase is decreased with increasing sintering temperature. At 1050°C, the fraction of the β-phase is reduced to 9.8 wt.%. This indicates that phase transfer and dissipation are faster at this temperature.

3.3.2. Metallography

The morphological features while cooling with different rates were identified, the microstructure composed of α-plates having a lamellar appearance and particle boundary α-phase having an equiaxed appearance (Figure 3.16 and 3.17). In the field assisted sintering, the original Ti-6Al-4V particles only occurs localized connection, except for the starting lamellar

microstructure in the particle interior, the equiaxed α-phase recrystallized in the connection zone was observed. In situations where recrystallization takes place on cooling, the nucleation rate is determined by a Boltzman type equation, which has an activation energy that decreases more than linearly with decreasing temperature [95]. As the alloy was cooled with the cooling rate of 4.68°C/s, this gives a rapidly increasing nucleation rate, thus more equiaxed α-phase appeared at the particle boundaries. Decreasing cooling rate to the lowest examined in this study, 1.5°C/s, further growth of the α-plates progressively observed.

In addition, the sintering temperature appears to play an important role in the formation of the observed microstructures (Figure 3.18). At high temperatures, the crystallite of nucleation and growth are controlled by volumetric diffusion, resulting in increased thicknesses of the α-phase colonies. Increasing the sintering temperature to the highest examined in this study, 1050°C, a volumetric diffusion controlled Widmanstätten formation is observed. The features of the Widmanstätten structure is consistent with those reported by Ahmed et al. [96]. Sintering below the β-transus (980°C) leads to the development of microstructures composed both of lamellar and equiaxed α-phases. In this case, the volumetric diffusion is limited, therefore the crystallite growth controlled by the interfacial diffusion. The recrystallized β-phase penetrates into the staring α-phase lamellae along phase boundaries causing the separation into individual α-grains [97], the equiaxed structure can be seen.

3.3.3. Hardness and elastic modulus

The modulus of elasticity (E) and hardness (H) for the Ti-6Al-4V alloys were determined by nanoindentation tests. The increase in elastic moduli is due to the changes of material's crystal structure and microstructure with gas cooling. The hardness for Ti-6Al-4V is related to the presence of variation in the crystallite size. Comparing the results with the literature [52] data (elastic moduli: 105 GPa–116 GPa), it is obvious that the values of elastic moduli are higher. The higher (E) values mean that the alloys require more applied stress to deform the materials.

To account for these values, besides the effect of the two analytical procedures, the process of indentation on a non-homogenous sample should be analyzed. In such a sample, areas of separated phases formed within the alloy possess different mechanical properties, which would lead to different (E) and (H) values if the measurement was conducted on or near the grain boundary. This matter has been extensively studied [98-101], the differences in tensile and nanoindentation values were attributed to the different size and microstructural levels that were

probed. Nanoindentation tests measure a very small area of the sample surface, almost at the dimension of a single grain. Conventional tensile-testing procedures consider the entire alloy. However, the difference in this work is also due to the changes in the composition of the alloy used. It is well known that, for example impurity or oxygen levels have a dramatic influence on the Titanium alloy properties [102].

3.3.4. Compression fracture

The analysis on the compressive fraction shows that the fracture section was covered by shearing dimples that elongated in a certain direction with different sizes and depths. Figure 3.19 (a) shows a decrease connection area of the intact particles, which leads to the premature mechanical failure. Comparing the fracture surface of the sample subjected to 850°C sintering temperature (Figure 3.20), except for the elongated dimple patterns, many shear bands are observed on the surface, Analogous results have been found in other specimens (Figure 3.21). The dimple patterns as well as the smooth regions between them indicate a lower crack propagation speed.

The fracture surface for the sample synthesized with a cooling rate of 4.68°C/s has an occurrence of bigger dimple sizes (Figure 3.20 (f)). This indicates that it is more ductile, since the size of dimples can be used to quantify the ability of a material to absorb energy up to fracture under loading [103]. In the fracture surface referring to the specimen sintered at 1050°C, Figure 3.21 (f), more microvoids are observed, this feature indicates a relatively less ductile behavior. Regardless of the differences in the size of dimples, the fracture surfaces of all specimens had a similar appearance which indicates that the fracture mechanism is similar. Ductile fracture occurs as a result of the intense plastic deformation located along the crack entrance. In other words, inhomogenous stress distribution contributes to the generation of certain plasticity. It is known that the packed crystal structure (hcp) α-phase need a much higher local deformation, i.e. energy consumption, to nucleate dimples, than that required for the body centered cubic (bcc) β-phase. Therefore, it can be inferred that, in Ti-6Al-4V, the ductile behavior is dominated by the deformation of the α-phase.

3.3.5. Compression mechanical results

A weak connection between original particles was obtained in the alloy sintered at 750°C, which contributed to the yield strength of (606±34) MPa. Figure 3.24 plots the yield strength

increases with increasing cooling rate. This indicates the existence of the Hall-Petch type relationship, which established that the yield strength varies inversely to the square root of the crystallite size. The finer crystallite can be obtained by rapid cooling and cause the enhancement of a material's strength, since increasing crystallite boundaries are effective barriers for dislocation glide and climb, which moderates the localization of plastic deformation and delays the fracture.

Figure 3.25 shows the variation of the yield strength as a function of the sintering temperatures. As expected, the sintering temperature exhibits an obvious effect on the strength of the material. The yield strength of Ti-6Al-4V alloy sintered at 1050°C ((900±22) MPa) is lower than that sintered at 950° C ((922±28) MPa), and 850°C ((936±14) MPa), but most comparable to literature reported values (825 MPa–895 MPa) [52]. However, the ultimate compressive strength distribution for the Ti-6Al-4V alloys is quite narrow (Figure 3.23). This trend indicates that the drop of yield strength caused by the rise of crystallite size is pronounced under the present test conditions, and that the Hall-petch effect dominates the deformation process. In the bimodal microstructure, the localization of the equiaxed α-phase along the particle boundaries can also strengthen the alloy by dispersive strengthening through pinning the movement of the dislocations.

Though the α-phase is a room temperature stable phase, the β-phase can also be steadily retained at room temperature by the gas cooling. The results so far obtained show that, besides the α-phase, it must be considered the contribution of the β-phase to the overall mechanical properties. In this sense, studies are in progress seeking for the quantification of these partial phases, by determining the fraction of phases through the Rietveld refinement. In the case of shear buckling of Ti-6Al-4V alloy, α-grain buckling aids in dispersing localized stored energy during compressive deformation. This allows the alloy to absorb relatively large amounts of strain energy. Colonies of the α-phase lamellae with various orientations hinder the crack growth. When crossing the boundary between colonies, the crack changes direction, which causes crack branching and secondary crack creation. These processes require additional energy and result in increased yield strength of the material. Crack propagation through the β-phase grains does not require so much energy and in turn the strength is reduced with increasing the fraction of β-phase. Further, it is noted that sintering Ti-6Al-4V at 1050°C results in the Widmanstätten microstructure (Figure 3.18), which will also get the strength reduction.

From the stress–strain characteristics mentioned above, it is also found that some improvement in elongation could be achieved. High values of compressive strength together with improved ductility cannot be ascribed to the presence of finer crystallites in the microstructure, but the effect of residual β-phase must be considered. The microvoid-active energy in the β-phase is lower than those in the α-phase. The increasing amount of the β-phase results in a loss of resistance to the plastic deformation, therefore, the alloys display better ductility.

Chapter 04 Ti-6Al-4V foams synthesized by field assisted sintering technique

The content of this chapter is partly published in:
Quan Y, Zhang F, Rebl H, Nebe B, Keßler O, Burkel E. Ti-6Al-4V foams fabricated by spark plasma sintering with post heat treatment. Materials Science and Engineering: A. 2012, 565:118-25.

4.1. Experimental

4.1.1. Materials

As a basis of the powder mixtures, the Ti-6Al-4V powders with chemical purity of 99.0% (TLS Technik GmbH & Co, Germany) were blended with 99.0% pure NaCl powders and poly vinyl alcohol as a binder. The Ti-6Al-4V powders are spherical with size distributions of 5 μm–35 μm and the cuboidal sodium chloride powders have round angles as shown in Figure 4.1. In the preparation process, the size of the metal powders should be smaller than the average powder size of the space-holder material [104]. The space-holder particles with sizes of: 125 μm–250 μm, 250 μm–425 μm and 425 μm–650 μm, can be obtained by sieving.

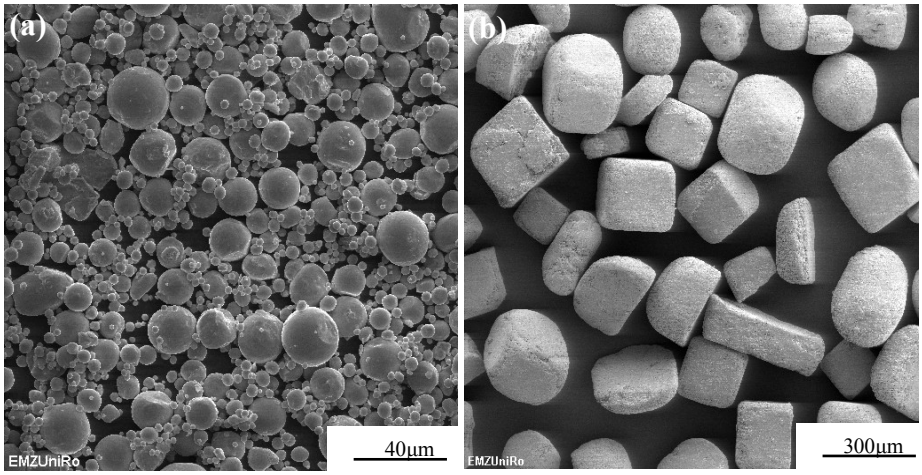

Figure 4.1. SEM images of the prealloyed Ti-6Al-4V (a) and NaCl powders (b).

4.1.2. Foams preparation

All blends were FAST treated under vacuum in cylindrical graphite dies. After heating the samples with a rate of 100°C/min up to different sintering temperatures, varied pressures were applied for 8 minutes to get disc-shaped pellets. Porous Ti-6Al-4V foams were obtained through dissolution of the NaCl space-holder in renewed deionized water for 72 hours at room temperature. The foams were cleaned in an ultrasonic water bath for 30 min and furnace dried at 120°C for 2 h. By changing the weight ratio of NaCl, a series of samples with different porosities were obtained.

In addition, a post-heat treatment was used to increase the strength of the foams. It was carried out by a pressureless mode of the FAST method [53, 105]. The set-up is shown in Figure 4.2. A small gap d was designed to avoid damaging the porous materials. The foams after the NaCl being removed were sintered at 1100°C for 5 minutes in this pressureless mode. The sintering cycles as presented in Figure 4.3. Table 4.1 gives an overview of the parameters used in the process.

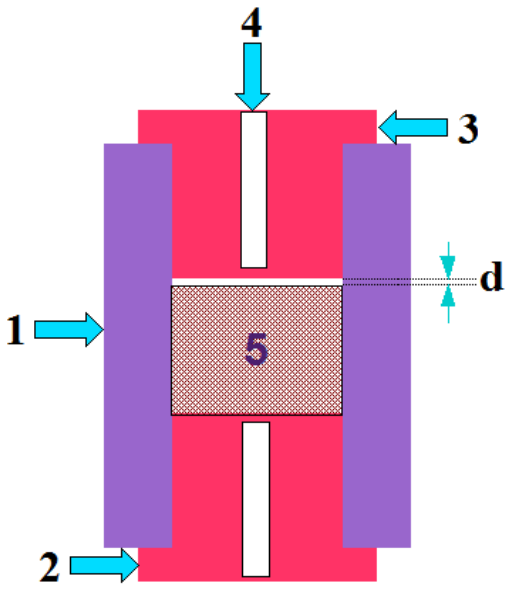

Figure 4.2. Schematic diagram of the graphite die set-up for the pressureless mode of the FAST (1. graphite form, 2. graphite bottom punch, 3. graphite up punch, 4. pyrometer measurement hole, 5. sample, d. gap>0mm).

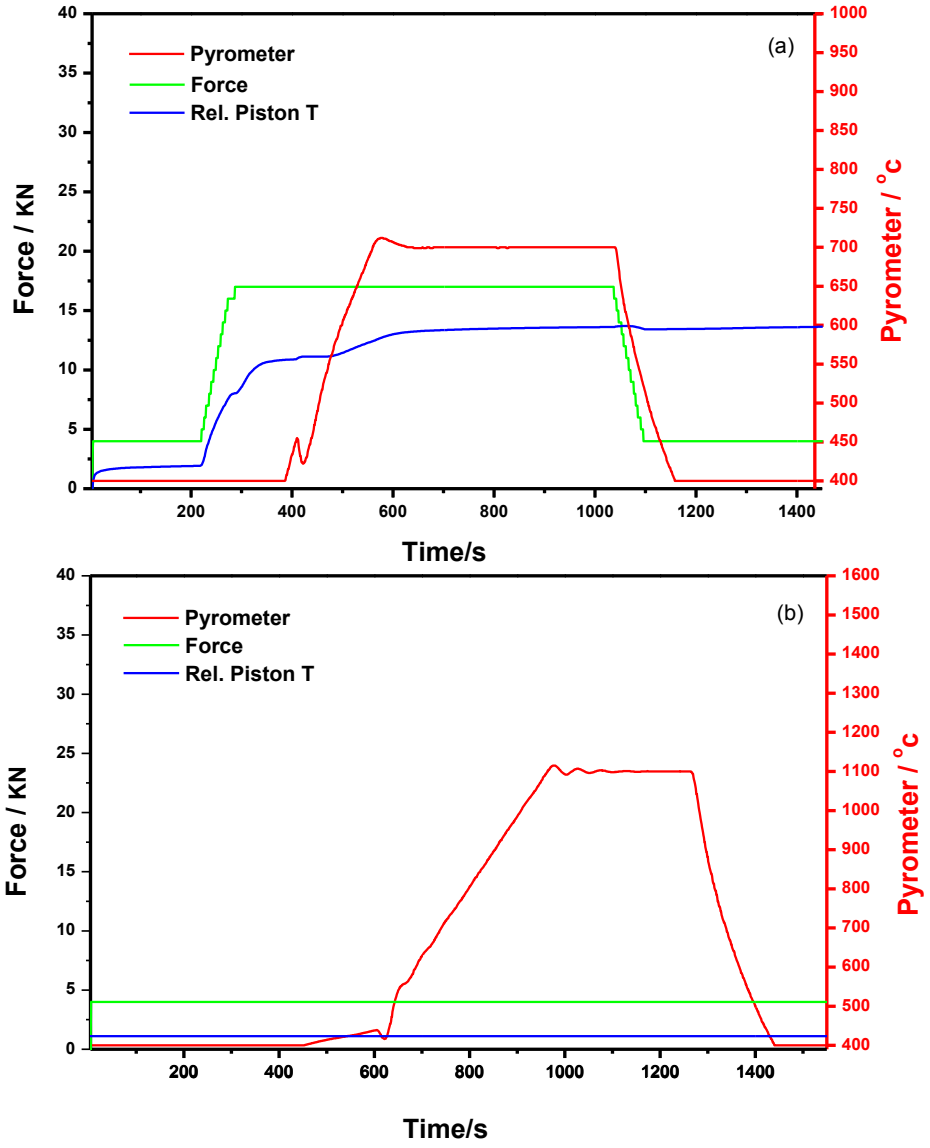

Figure 4.3. Field assisted sintering cycles of porous Ti-6Al-4V samples: (a) sintering with compaction pressure and (b) sintering without pressure.

Table 4.1. Overview of the parameters used in the sintering.

Temperature (°C)	Pressure (MPa)	Dwell time (min)	Result
650	50	8	success
700	50	8	success
720	50	8	NaCl melt
750	50	8	NaCl melt
700	60	8	Die break
700	80	8	Die break

1000	0	5	Weak densitification
1100	0	5	Well densitification
1200	0	5	Well densitification

4.2. Results

4.2.1 Synthesis of Ti-6Al-4V foams

Figure 4.4 shows the calculated relative density for foam struts as a function of NaCl/Ti-6Al-4V ratio after sintering at different temperatures. The red line shows the values from the samples with sintering temperature 700°C and the blue line shows values after post-heated at 1100°C. The relative density increases with the rise of sintering temperatures and NaCl fraction. It is found that the value for samples sintered at 1110°C, with a NaCl/Ti-6Al-4V ratio of 0.34 is nearly 99% of the theoretical density.

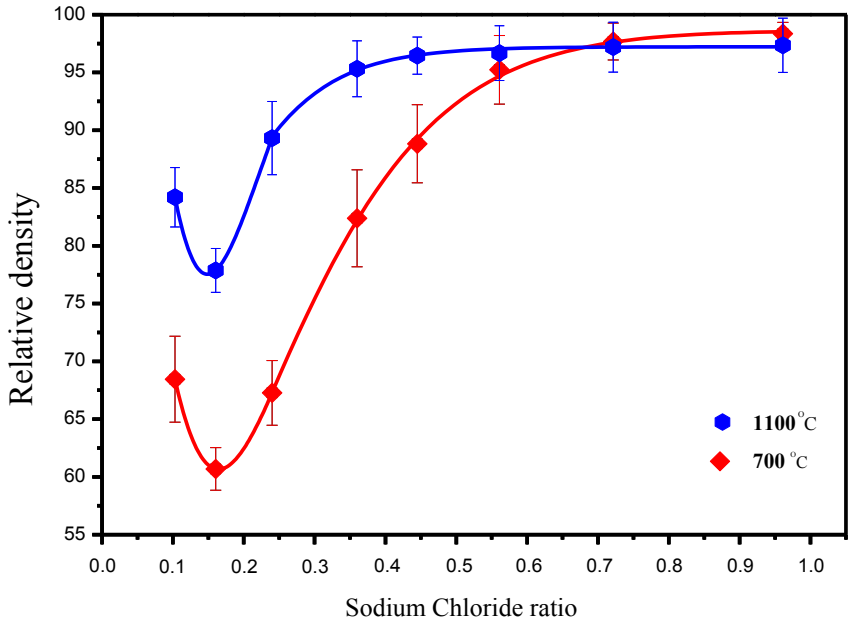

Figure 4.4. The relative density of foam struts after different sintering temperatures as a function of NaCl/Ti-6Al-4V ratios.

Figure 4.5 shows the porosities of the post heated Ti-6Al-4V foams with changing NaCl/Ti-6Al-4V ratios. The red line shows the values evaluated from the weight and the apparent volume of the specimens and the blue line shows values from a theoretical calculation. Below the ratio of 0.73, the porosity of the foams is higher than the theoretical ones. Increasing the ratio to 2.27, the foams show a lower apparent porosity compared to the theoretical value.

Table 4.2 shows a summary of the parameters for Ti-6Al-4V foams after the field assisted

sintering. After the foams were sintered at 700°C, they show porosities of (48±3)%, (58±3)%, (64±1)%, (68±3)%, (73±3)%, (76±2)%, (79±3)% and (82±3)%, respectively. When they are post heat treated at 1100°C, they display porosities of (45±2)%, (54±3)%, (61±3)%, (65±3)%, (70±3)%, (74±2)%, (77±3)% and (81±3)%. The densities of the foams increase 5.5%, 7.5%, 8.9%, 8.6%, 9.1%, 9.7%, 9.5% and 9.5% after the heat treatments. The foams sintered with higher space-holder sizes show bigger increments of density (10.1% and 9.7%, respectively).

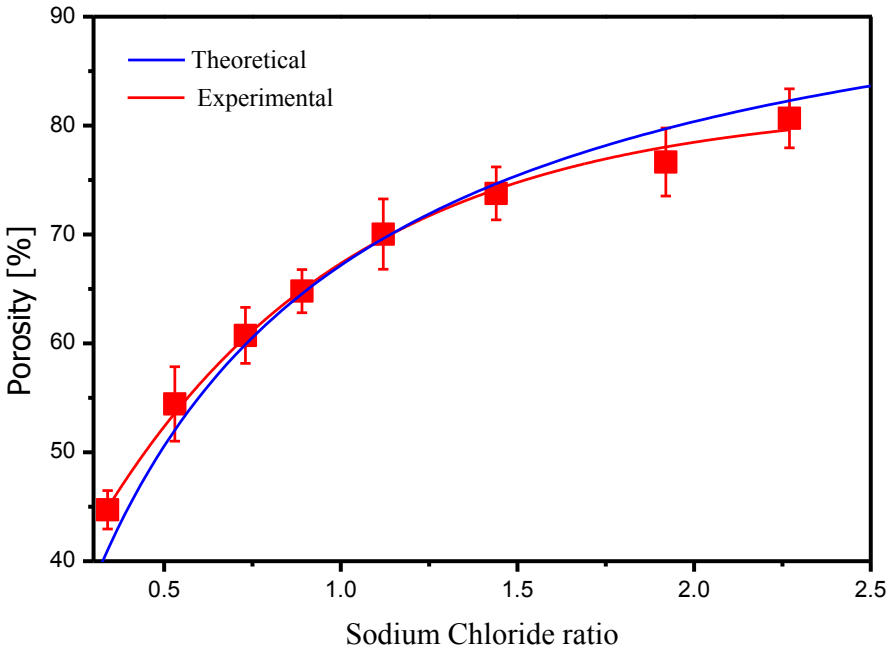

Figure 4.5. Porosities varied with the changing weight ratio of NaCl space-holders.

Table 4.2. Porosities of the Ti-6Al-4V foams after sintering at different temperatures.

Specimen NO	Space-holder size (μm)	NaCl ratio	Porosity (700°C) (%)	Porosity (1100°C) (%)	Increments of density (%)
1	125-250	0.34	48 ± 3	45 ± 2	5.5
2	125-250	0.53	58 ± 3	54 ± 3	7.5
3	125-250	0.73	64 ± 1	61 ± 3	8.9
4	125-250	0.89	68 ± 3	65 ± 2	8.6
5	125-250	1.12	73 ± 3	70 ± 3	9.1
6	125-250	1.44	76 ± 2	74 ± 2	9.7

7	125-250	1.92	79 ± 3	77 ± 3	9.5
8	125-250	2.27	82 ± 3	81 ± 3	9.5
9	250-425	1.92	79 ± 3	77 ± 3	10.1
10	425-650	1.92	80 ± 4	78 ± 4	9.7

4.2.2. X-ray diffraction analysis

Figure 4.6 demonstrates the high energy X-ray diffraction patterns for the Ti-6Al-4V foams produced by the FAST and the prealloyed powders. The XRD patterns are comprised of the diffraction peaks indicating the α-Ti and β-Ti phases. The α-phase is the dominant phase in the prealloyed powders. Sintering at 700°C, in addition to the diffraction peaks of the α-phase, a peak of the β-phase (110) is visible. The α-Ti phase is still the dominant phase in the Ti-6Al-4V foams after the post-heat treatment at 1100°C. Additionally, the β-phase peaks (110), (200) and (211) are detected.

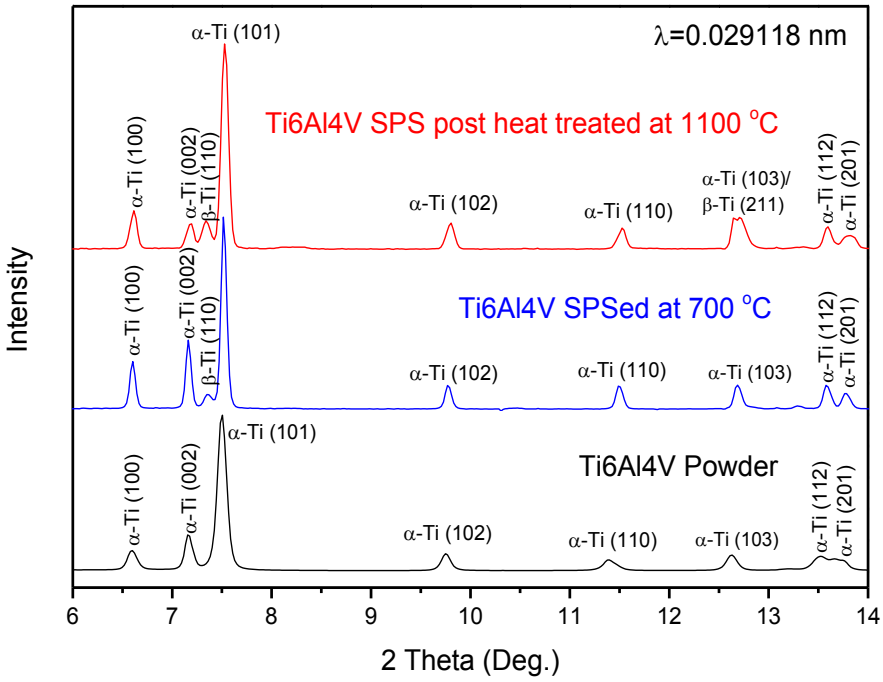

Figure 4.6. Synchrotron Radiation high energy X-ray diffraction patterns of the Ti-6Al-4V powders and field assisted sintered Ti-6Al-4V foams.

4.2.3. SEM micrographs

Figure 4.7 shows the images of the porous metals with different pore sizes. The foams were

produced by a similar NaCl/Ti-6Al-4V ratio with increasing space-holder size, which resulted in identical structures with increasing pore sizes. Because of the increasing size of the space-holder particles, the distances between the struts were larger leading to larger interconnecting pore sizes.

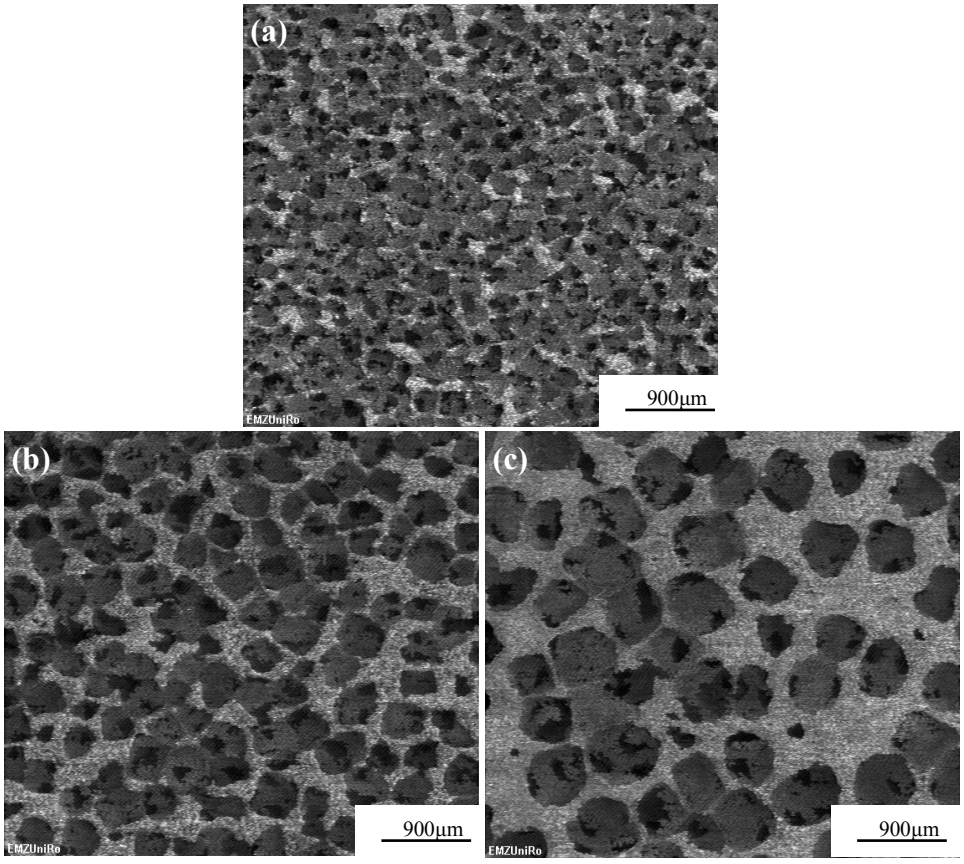

Figure 4.7. SEM images of the porous structures for the Ti-6Al-4V foams sintered with different space-holder size: (a) 125 μm-250 μm, (b) 250 μm-425 μm, (c) 425 μm-650 μm.

SEM images of the samples after post-heat treatment at different temperatures are shown in Figure 4.8. Figure 4.8 (a) shows the cell strut of the foam, having rough surfaces, with many micropores, indicating that at 1000°C it cannot densify the foam strut well. Conversely, microstructures are smooth on the strut of the Ti-6Al-4V implant post-heat treated at 1100°C (Figure 4.8 (b)). At 1200°C, the strut of pores was well densified with melting of the particle boundaries (Figure 4.8 (c)).

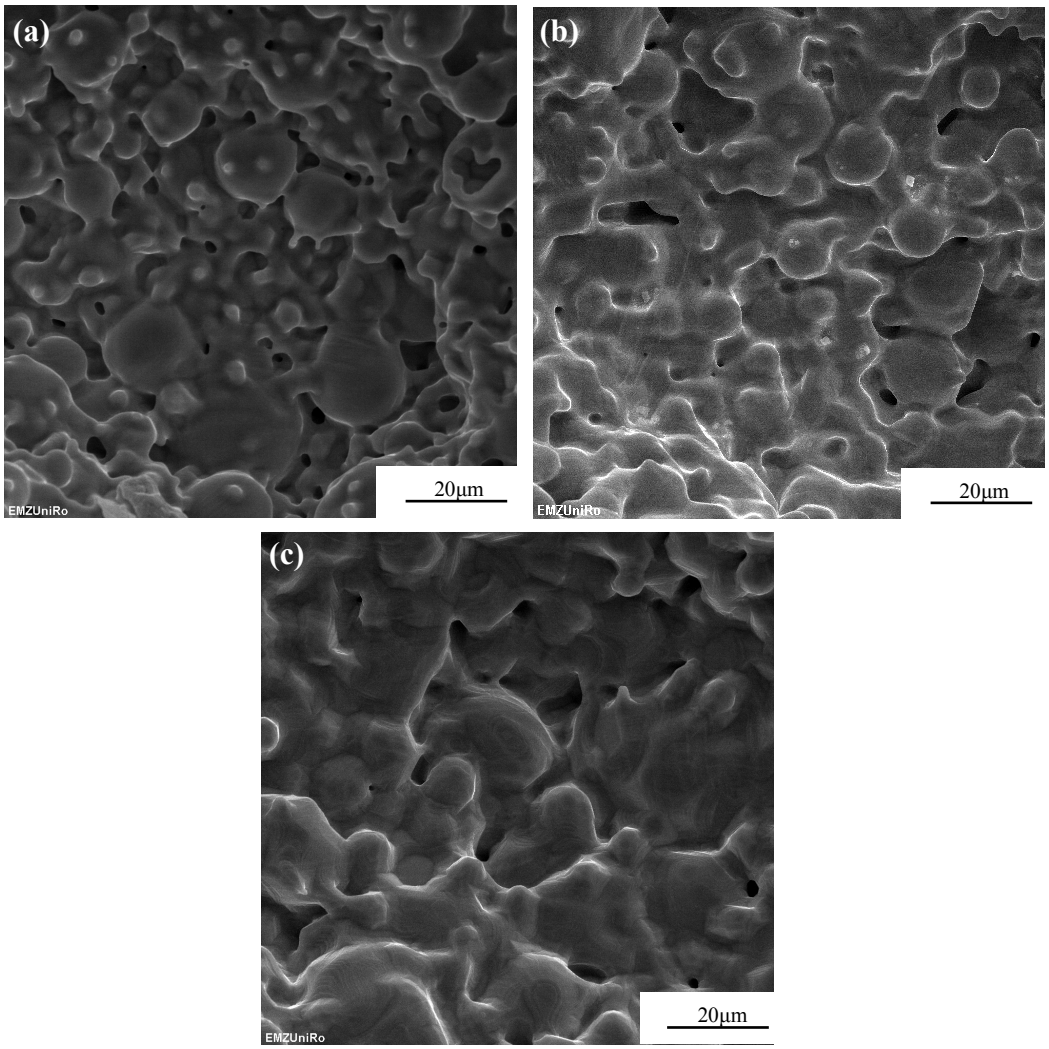

Figure 4.8. SEM images of the pore walls for the Ti-6Al-4V foams pressureless sintered at (a) 1000°C, (b) 1100°C, (c) 1200°C.

Figure 4.9 shows the SEM micrographs of the porous Ti-6Al-4V foams with different porosities of (45±2)%, (54±3)%, (61±3)% and (70±3)%. It shows the pore sizes ranged from 150 µm to 260 µm with the NaCl spacing material in the range of 125 µm to 250 µm. The thicknesses of the pore struts decrease with increasing porosity. The higher porosity samples show good interconnectivities. The primary pores replicate the sizes and shapes of the angular NaCl particles with rounded corners. Thus, pore shapes can be controlled by using NaCl powders with various shapes. Finally, interconnected pores are visible either as black pores or as necks between adjacent pores in cross sections. These interconnected pores usually ranged 20 µm – 150 µm in sizes, indicating that osteoblasts may be able to penetrate into the porous structure.

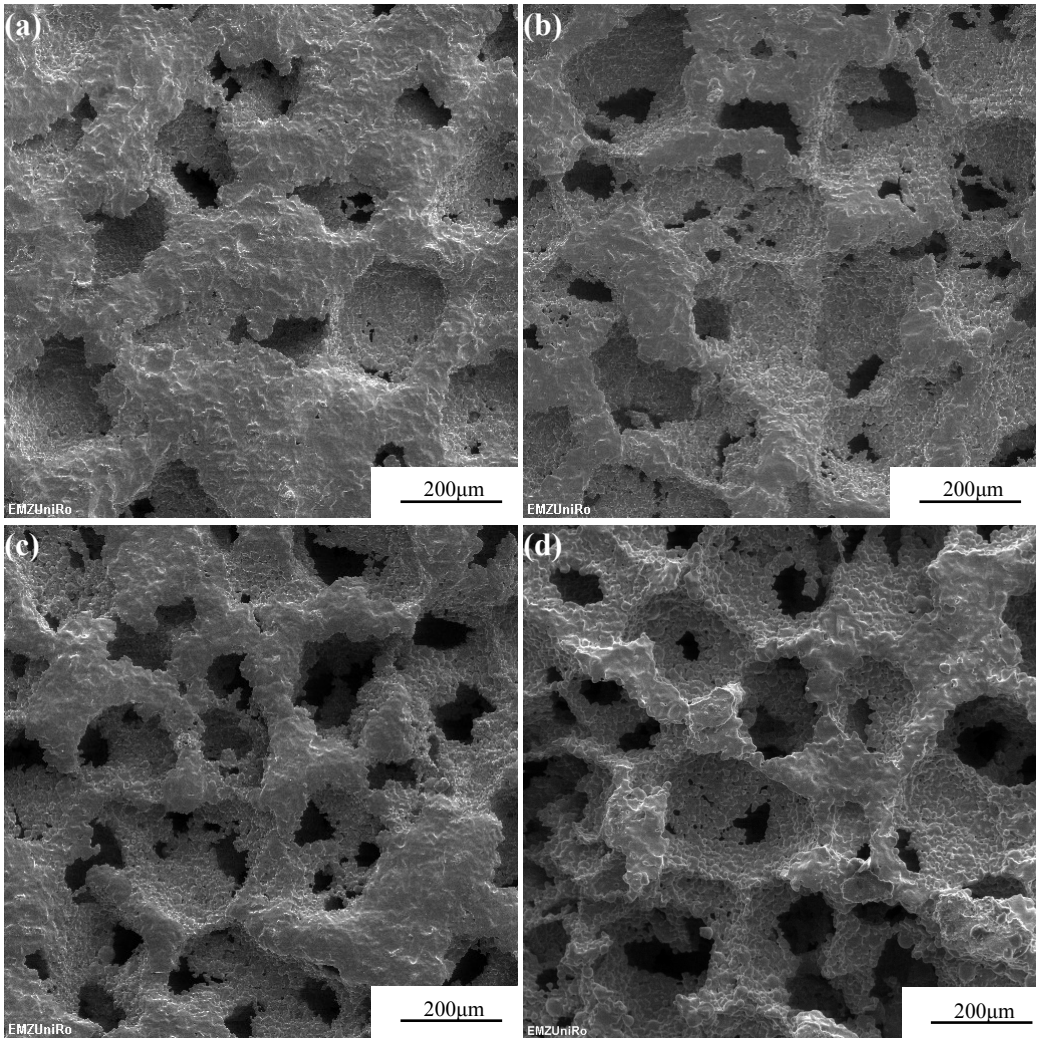

Figure 4.9. SEM images of the Ti-6Al-4V foams prepared by FAST with different porosities of (a) 44.7%, (b) 54.4%, (c) 60.7%, (d) 70.0%.

Detailed microstructural views of the Ti-6Al-4V foam with (70±3)% porosity are shown in Figure 4.10. Figure 4.10 (a) and (b) display the foams synthesized at 700°C and 50 MPa. They show the porous structure and the pore struts, revealing relatively uniformly shaped macropores having rough surfaces, with many micropores and the shapes and the sizes of the original alloy powders being visible. This indicates that the Ti-6Al-4V/NaCl mixture is difficult to be densified and, as expected, the melt of the alloy powders at 700°C was not sufficient to smooth the micropores due to the very high melting point of Ti-6Al-4V. Figure 4.10 (c), (d) display the Ti-6Al-4V foams post-heat treated at 1100°C with the pressureless mode. After the heat treatment, the junctions between the original particles are formed with only few micropores left. As seen in

Figure 4.10 (d), most of the micropores disappeared due to the heat treatment. Since no pressure was applied and only diffusion dominated the FAST process, this indicates that the pressureless heat treatment contributes to reduce the microporosity of the struts. Thus, Ti-6Al-4V foams with higher density of the pore struts can be synthesized by the FAST method at 700°C with a post-heat treatment at 1100°C.

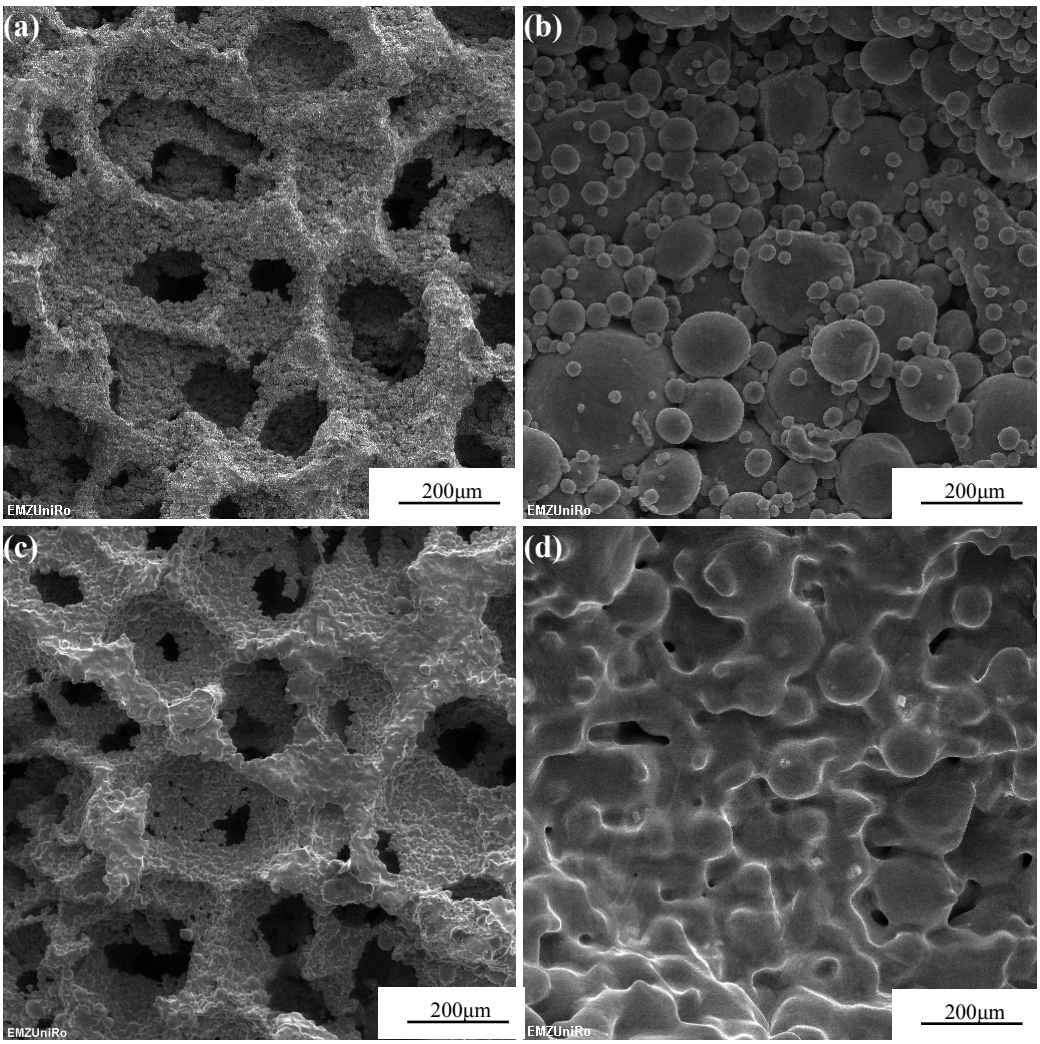

Figure 4.10. SEM images of the porous structures and pore walls of the Ti-6Al-4V foams sintered at 700°C, 50MPa (a, b), and FAST post heat treatment at 1100°C (c, d).

4.2.4. Micro computed tomography

The outer shape of the Ti-6Al-4V foam with (54±3)% porosity is shown in Figure 4.11 (a). Figure 4.11 (b), (c), (d) display the micro-CT 3D reconstructions of the foam. From the images, the complex macroporous structure is recognizable. The macrostructure of the foam is composed of homogeneously dispersed porous cavities (dark) and continuously connected Ti-6Al-4V struts (yellow). The Micro-CT 2D top view and side views show that the pore sizes range from 170 µm to 250 µm. Other samples show similar morphologies but different strut thickness and interconnectivities.

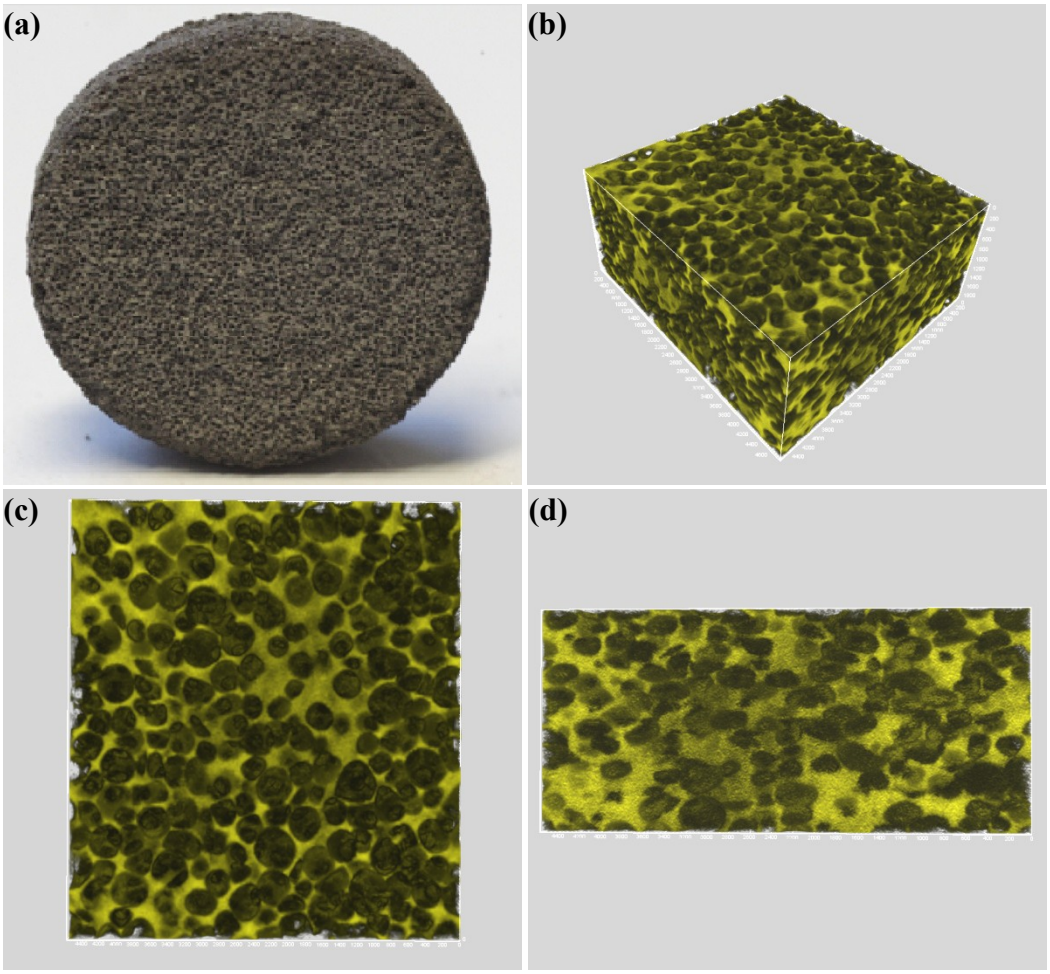

Figure 4.11. Micro-CT three-dimensional 3D reconstructions of the Ti-6Al-4V foam (54% of porosity) with outer shape of the alloy foam (a), an isometric view (b), 2D top view (c), left side view (d) (scare bar 200 µm).

4.2.5. Mechanical evaluations

For the evaluation of the mechanical properties of the porous samples, compression tests were performed along the axial direction. The compressive stress-strain curves of the Ti-6Al-4V foams are shown in Figure 4.12. It is noted that for all the test samples, the curves are typical for porous metals in compression since they exhibit initial deformation, a plateau region corresponding to the collapse of the pores, and an upward inflection corresponding to compression. However, the differences are obvious in the yield strength as the low porosity specimens demonstrate significantly increased values when compared with those of the high porosity samples.

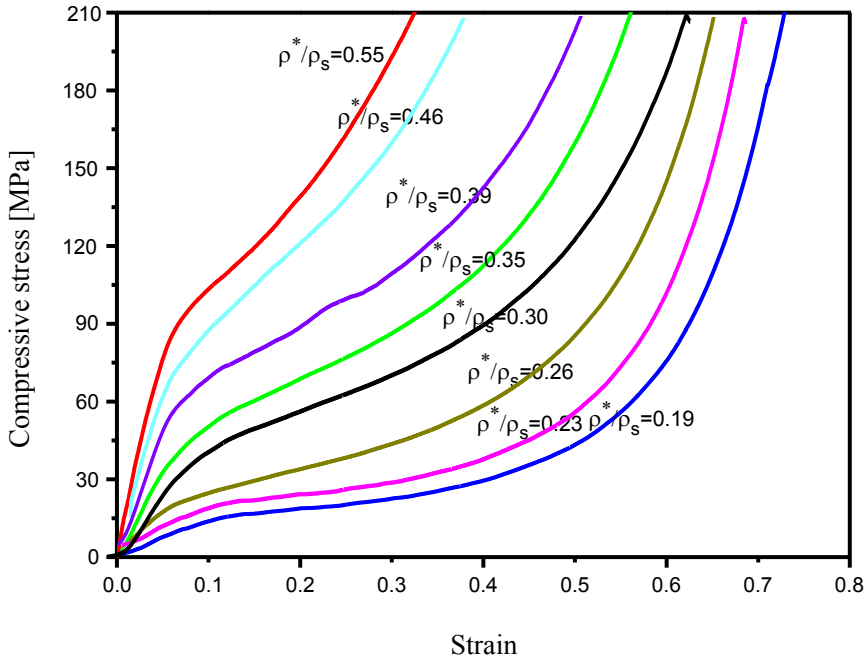

Figure 4.12. Compressive stress-strain of the Ti-6Al-4V samples with different relative densities.

Table 4.3 summarizes the mechanical properties of the investigated foams after the compression tests. As expected for porous solids, the relative density of the structure shows an important influence on the mechanical property. The porous samples exhibit elastic moduli from (1.9±0.9) GPa to (34.1±3.2) GPa while the relative density increases from 0.19 to 0.55. The values for the compressive strength increase from (18±3) MPa to (110±8) MPa with increasing relative densities. This data confirms that the mechanical property of the cellular solids is directly correlated to the porosity. The elastic moduli and the compressive yield strengths of the foams are comparable to that of bones [106]. For this reason, Ti-6Al-4V scaffolds can be used for

under-loading applications.

Table.4.3. Mechanical properties of the porous Ti-6Al-4V structures obtained in the compression tests.

Specimen NO	Relative density	Compressive strength (MPa)	Elastic modulus (GPa)
1	0.55 ± 0.07	110 ± 8	34.1 ± 3.2
2	0.46 ± 0.06	87 ± 7	25.9 ± 2.6
3	0.39 ± 0.05	63 ± 4	16.9 ± 1.5
4	0.35 ± 0.07	53 ± 5	10.5 ± 1.8
5	0.30 ± 0.05	43 ± 3	9.5 ± 1.0
6	0.26 ± 0.08	33 ± 3	6.4 ± 1.0
7	0.23 ± 0.04	25 ± 4	3.2 ± 1.0
8	0.19 ± 0.07	18 ± 3	1.9 ± 0.9
9	0.23 ± 0.06	23 ± 5	3.0 ± 1.1
10	0.22 ± 0.06	21 ± 3	3.0 ± 0.8

Figure 4.13 shows a comparison between the elastic moduli of the Ti-6Al-4V foams and the predicted theoretical values. The elastic moduli of the porous metals are compared with the prediction according to the Gibson and Ashby model [107]:

$$E/E_0=C\,(\rho^*/\rho_s)^2 \qquad (4\text{-}1)$$

where E and E_0 are the elastic moduli of foam and bulk materials with densities ρ^* and ρ_s , respectively, using E_0=117 GPa and ρ_s=4.43 g/cm^3 for Ti-6Al-4V [108]. The proportionality constant C has to be considered as 1 for titanium alloys [107]. The actual measured elastic moduli of the foams are exponential decay with the porosity increase, ranging from (34.1±3.2) GPa to (1.9±0.9) GPa, which comparable with the calculated moduli.

Besides the elastic modulus, the yield strength is an important property of an orthopedic implant, in particular in loading applications. According to the Gibson-Ashby model, the relationship between the yield strength and relative density is given by [107]:

$$\sigma/\sigma_0=C\,(\rho^*/\rho_s)^{3/2} \qquad (4\text{-}2)$$

where σ_0 and ρ_s are the yield strength and the density of the solid material, σ and ρ^* of the foam, respectively. The experimental data for open-cell structures indicates that C is around 0.3 and the strength of the foam is proportional to the strength of the solid (n=3/2) [109]. The density of dense solid Ti-6Al-4V is 4.43 g/cm3 with a yield strength 902 MP [110]. The yield strength of Ti-6Al-4V foams and predicted theoretical values for open porous material are given in Figure

4.14. It can be seen that the measured values for porous Ti-6Al-4V are slightly lower than the analytical predictions by Gibson and Ashby for open structures

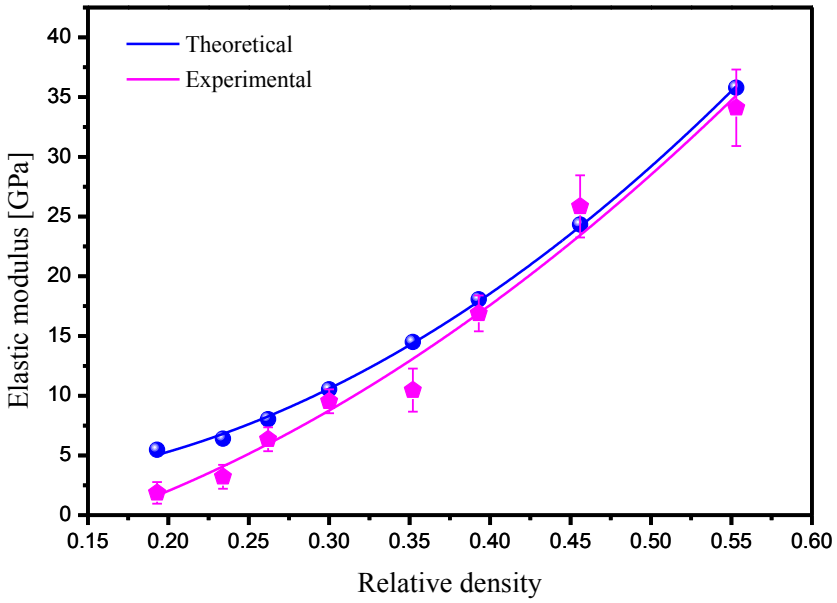

Figure 4.13. Elastic modulus of the Ti-6Al-4V foams and theoretically predicted values.

.

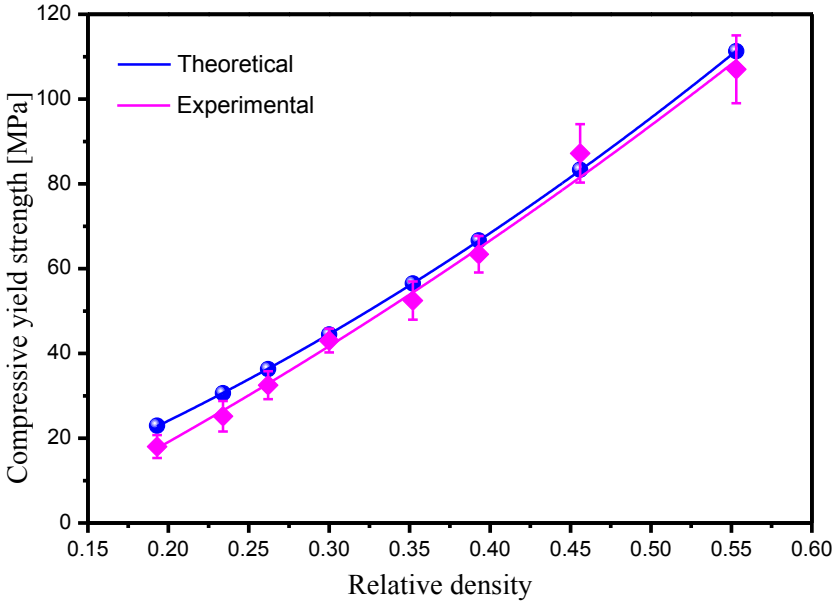

Figure 4.14. Compressive yield strength of the Ti-6Al-4V foams and theoretically predicted values.

To estimate the correlation between the mechanical property and the pore size of the porous Ti-6Al-4V alloys, the mechanical properties of the foams are plotted against the space-holder sizes, as shown in Figure 4.15. The compressive strengths decrease from (25±4) MPa to (21±3) MPa and the elastic modulus reduce from (3.2±1.2) GPa to (3.0±0.8) GPa with the pore size increasing.

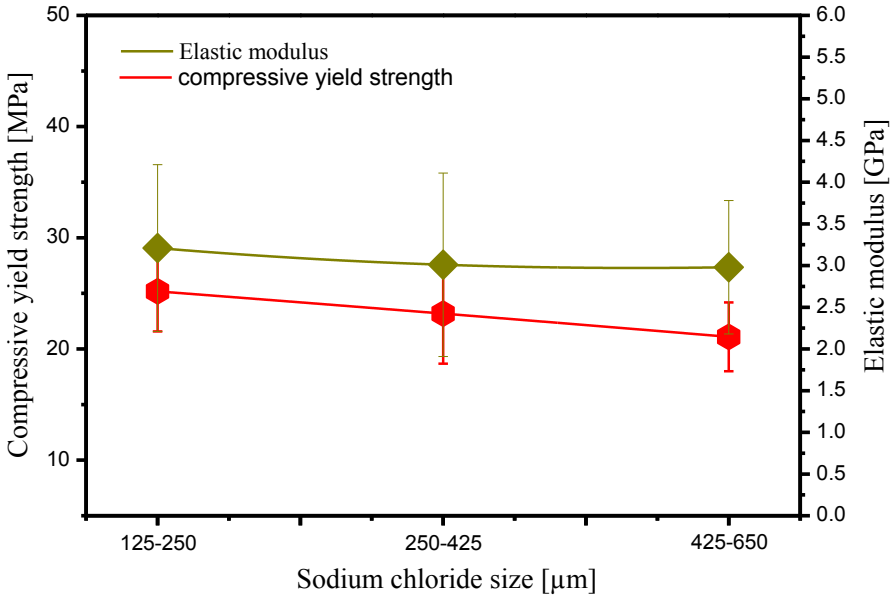

Figure 4.15. Effect of space-holder sizes on the elastic modulus and compressive yield strength of the Ti-6Al-4V foams.

4.2.6. Culture of human bone cells

Human osteoblast like cells (MG-63) were cultured on the porous Ti-6Al-4V samples. Figure 4.15 shows the SEM images of human bone-like MG-63 cells on the porous Ti-6Al-4V foams with porosities (45±2)%, (54±3)%, (61±3)%, and (70±3)%. After 24 hours they exhibit a well spread morphology and excellent bonding to the surface. The cells formed filopodia to reach the adjacent particles of the Ti-6Al-4V structure. The cells grow inside the pores to a large extend implying a good integration when implanted into the scaffold. The cell tests display that the pore sizes and porous surfaces of the Ti-6Al-4V foams synthesized by the FAST are suitable for the in-growth of osteoblasts.

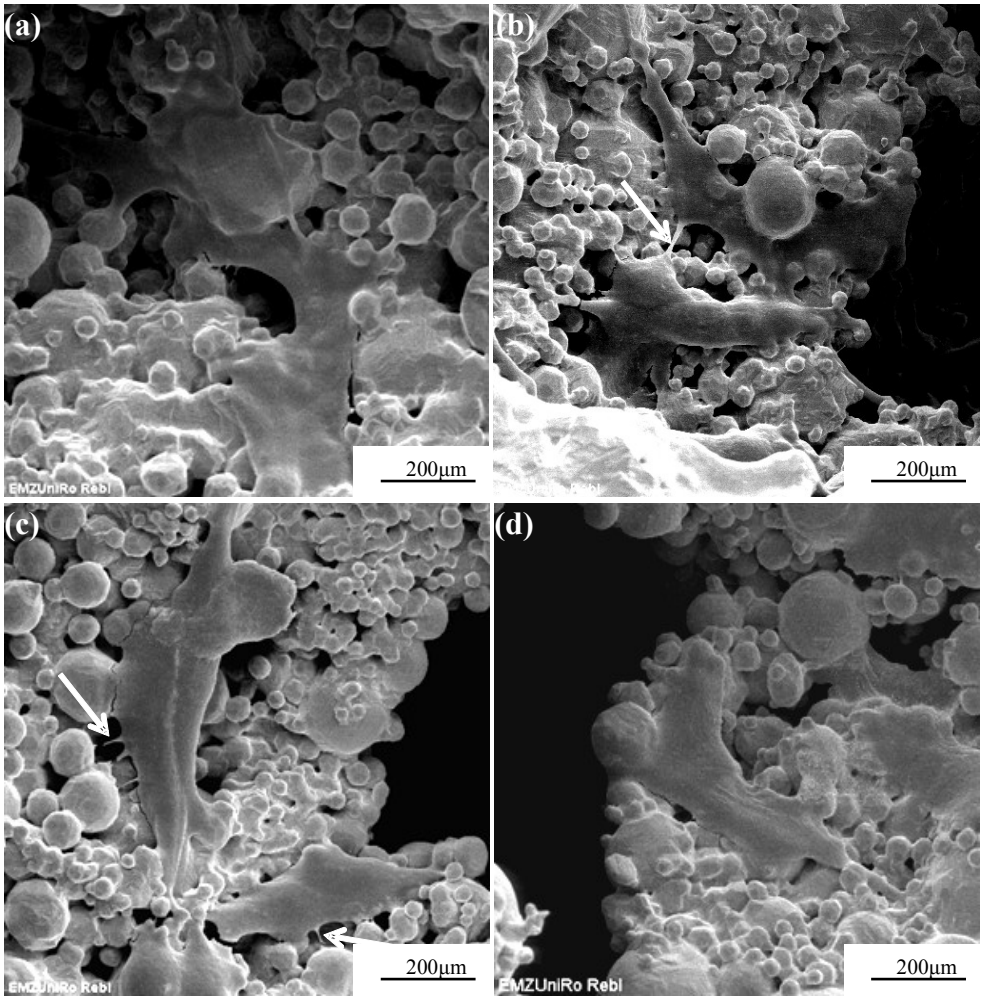

Figure 4.16. SEM of human bone-like MG-63 cells on porous Ti-6Al-4V foams (a) 45%, (b) 54%, (c) 61%, (d) 70%. The cells display a well spread morphology and moreover the cells extend various filopodia to the adjacent grains (arrow).

4.3. Discussion

4.3.1. Synthesis of Ti-6Al-4V foams

The synthesis of metal implants with mechanical properties matching those of human bones is generally difficult. Various methods have been reported to obtain the porous compacts. Under FAST, the local surfaces of the particles melt, allowing junctions to be formed between the particles in contact. In addition, a space-holder remaining during the process allows the use of pressure to enhance the densification of the powders. In this study, the Ti-6Al-4V foams were synthesized by using FAST at 700°C with controlled porosity followed by dissolution of the NaCl phase and a post-heat treatment at 1100°C. The NaCl has a melting point of 801°C. In the

actual experiments, the temperatures of 650°C, 700°C, 720°C, 750°C have been tested in the first step of the FAST. At 720°C, only a small amount of NaCl melted resulting in the formation of some impurities. At 750°C, most of NaCl spacer melted and the thermal expansion destroyed the graphite die. The sintering temperature 700°C was determined finally in order to get a relative well densification without the NaCl melting. Higher pressures from 60 MPa to 80 MPa have been tested. At these pressures, the graphite dies broke easily due to the thermal expansion of the Ti-6Al-4V/NaCl mixture during sintering. The pressure of 50 MPa allows the use of pressure to enhance the densification of the Ti-6Al-4V/NaCl mixture. In the end, the parameters of 700°C and 50 MPa were selected.

Previous investigations showed that well-densified Ti foams can be synthesized with NaCl space-holders by the FAST at 700°C and 50 MPa [111]. However, the Ti-6Al-4V/NaCl mixture cannot be densified at the same condition. Powders forming the foam struts are only partially densified after 8 min of sintering at 700°C. It indicates that this Ti-6Al-4V/NaCl mixture is difficult to be consolidated either in the hot pressing [55] or in the FAST. The Ti-6Al-4V foams were post-heat treated by the pressureless FAST method at 1100°C for 5 minutes. The beta transus temperature of the Ti-6Al-4V alloy is about 980°C [52]. In the second run, several temperatures (1000°C, 1100°C and 1200°C) over the transus were tested. The results indicated that at 1000°C the foam struts cannot be well densified. At 1200°C, the samples were well densified but with the increased cost of power. Hence, the post-heat treatment temperature was confirmed at 1100°C. The densities of the foams have been increased as shown in Table 4.2. The macroporosity determined by the ratio of NaCl space-holder. The post-heat treatment would contribute to reduce the microporosity of the struts. As the schematic diagram of the set-up for pressureless FAST in Figure 4.2 indicated, the sample was heated by the temperature field of the graphite die. Since there was no pressure applied, surface and boundary diffusion dominated the densification process. These diffusion processes play the main roles for reducing the microporosities in the struts. This post-heat treatment is similar to the technique of hot isostatic pressing (HIP) used to reduce the microporosity of metals and to increase the density of many ceramic materials, thus improving the material's mechanical properties. The only difference between them is the efficiency where the pressureless FAST is much faster with a faster heating rate and a shorter holding time. The results in this study indicate that this pressureless FAST method can be used for post-heat treatment of Ti-6Al-4V foams, and possibly for all the metallic

foams, dense metals and ceramics.

During the foam preparation, various porosities can be achieved by varying the NaCl/Ti-6Al-4V ratios. Figure 4.3 shows the relative density of the foam struts as a function of NaCl/Ti-6Al-4V ratio. It was noticed that the relative density of the foam struts varied with the fraction of NaCl. At lower NaCl/Ti-6Al-4V ratio, the metal powders were too much and it was difficult or impossible to get complete dissolution of the space-holders, which indicates that there was residual NaCl in the foam struts after the manufacturing process. When more NaCl was added, the struts had higher relative densities, implying the dissolution of space-holder was more effectively. With continuously increasing NaCl/Ti-6Al-4V ratio, the Ti-6Al-4V powders were too less to cause sufficient connections needed for the foam production resulting in the porosity of the foams lower than the theoretical values (Figure 4.4). It was experimentally found that a suitable NaCl/Ti-6Al-4V ratio is in the range of 0.34–2.27. The space-holder size of 125 μm – 650 μm is chosen to achieve a final pore size in the range of 150 μm–700 μm, which permits to analyze the effect of pore size on the mechanical properties of foams.

4.3.2. X-ray diffraction

The diffraction pattern confirms the α-phase in the Ti-6Al-4V powders. The α-phase is still the dominant phase in the Ti-6Al-4V foams after the FAST processes. In addition to the diffraction peaks of the α-phase, a small amount of residual β-phase is detected in the sample sintered at 700°C. After the post-heat treatment, the diffraction pattern shows that the intensity of the α-Ti (002) peak is weaker and the peak of the β-phase (110) is higher compared to that of specimens sintered at 700°C. The post-heat treatment has increased the fraction of the β-phase in the foams.

4.3.3. Microstructures

The amount of porosity defines most foam applications and thus it is the most important characteristics. Open-cellular pores are necessary for bone ingrowth. Extensive body fluid transport through the porous scaffold matrix is possible, which can trigger bone growth if substantial pore interconnectivity is established [66]. The characterization of the porous materials indicates that FAST allows the synthesis of scaffolds with well-controlled porous structure. In the present study, the measured porosity of samples was in the range of 45%–81%. The morphologies of the produced Ti-6Al-4V foams are shown in Figures 4.7-11. It is clear that there

are two types of pores: interconnected pores, which are called macropores, and micropores. The interconnected macropores are a result of NaCl decomposition. The sizes of these pores range from 150 μm to 700 μm. However, there are also some micropores in the foam struts. They are the result of partial sintering of the Ti-6Al-4V powders.

4.3.4. Mechanical properties

The differences of the bone mechanical properties set challenges for fabricating biomaterial scaffolds that can meet the requirements of specific applications. The design and the synthesis of a bone graft substitute should find a balance between mechanical function and biological performance. Porous titanium implants were synthesized with porosities of 5.0% to 37.1% by powder sintering by Oh I.H et al [72]. The implant with a porosity of around 30% showed an identical Young's modulus as human cortical bone. By using a technique called laser engineering net shaping, Krishna et al. have demonstrated that the modulus of implants can be varied from 1.7 GPa to 47.7 GPa and that samples with 27% porosity presented matched strength and modulus with human cortical bone [76]. The compressive strength of Ti alloy synthesized by hot pressing with about 67% porosity was tested to be 28 MPa [55]. Takemoto reported porous titanium with 40% porosity and a compression yield strength of around 85.2 MPa [112]. Titanium foam with the controlled porosity in the range of 17 percent to 58 percent and pore sizes up to 800 μm showed that the strength varies from 24 MPa – 463 MPa with stiffness values increasing from 2.6 GPa–44 GPa [75].

Using FAST allows to control properties of the metallic implants with the help of space-holder material. The compression stress–strain curves of foams with 45%–81% porosity are illustrated in Figure 4.12. The foams show the typical stress–strain behavior of metal foams [82], which consists of three regions. Region one is the elastic deformation area; region two is the plateau stage in which the pores start to crash and are distorted, causing the strain to increase while the stress flows smoothly. Finally, in region 3, the pores crash, the stress increases sharply and the mechanical behavior of the foam transforms into that of bulk materials. The elastic modulus of the produced Ti-6Al-4V foams varied from 1.9 GPa to 34.1 GPa. Similarly, the yield strength of the foams was in the range of 18 MPa–110 MPa. It is obvious that when the porosity increases, the yield strength and the elastic modulus decrease. There are some empirical relations that relate the mechanical properties of the foams to their densities. The Gipson and Ashby model [107] suggests that the wall of pores contribution to the overall stiffness depends linearly

on the relative density (ρ^*/ρ_s). In contrast, the contribution of the struts is nonlinear. In the theoretical relation, all of the structural features are assumed to be ideal. In this study, the mechanical properties were found to be lower than expected from the idealized models. This is attributed to the inefficient sintering resulting in interconnected micropores in the load bearing pore struts.

Increased porosity and pore sizes are obviously preferential for new bone growth in implants, but another consequence of the porosity increase is the reduction of the implant mechanical properties. The influence of the pore size can be illustrated using the compression results for sintered Ti-6Al-4V foams with an average porosity of 77% (Figure 4.15). At this high porosity, the Ti-6Al-4V scaffolds were easy to break due to the thin strut of foams. For the narrow range of porosities, typical compression values are very similar since only little variations were observed. The slightly increases with decreasing size of used NaCl space-holder are due to the fact that the finer pores possess higher packaging capability than the larger ones.

4.3.5. Cell culture

Because of the passive oxide film formed at the surface of materials, the Ti alloys have very good corrosion resistance. The oxide films on the powder surfaces would probably have some effects on the sintering temperatures; however, it is not noticeable during the FAST process. In another side, the biological properties of a Titanium alloy implant depend on its surface oxide film [113]. The TiO_2 has good cell biocompatibility and it is already used as a coating on many Ti alloys [114]. In this study, there are no bad effects been observed for the oxide films interaction with the MG-63 cells. The highly porous nature of the alloys combining improved mechanical properties with osteoconductivity makes these materials ideal for bone scaffolds.

Chapter 05 General discussion and future outlook

5.1. General discussion

Titanium and its alloys are currently receiving attention in both the medical and the dental field due to excellent biocompatibility, light weight, good balance of mechanical properties, corrosion resistance, etc. They are mainly used in implant devices for replacement of failed hard tissue, for example, artificial hip joints, artificial knee joints, bone plates, dental implants, etc. For biomedical applications, the implanted material must be strong enough and durable to withstand the physiological loads placed upon it over the years. Strength considerations require the use of the materials in their solid form. Research using field activation in sintering has increased dramatically in the past decade and has drawn attention to this process at both the fundamental and the applied levels. With the aid of high electric currents, it is possible to consolidate powders to full density much faster and at lower temperatures than by traditional methods such as pressureless sintering or hot pressing. For example, a typical FAST run is approximately 30 min from start to finish, in contrast to processing times on the order of hours required for conventional methods.

Applying the field assisted sintering technique, Ti-6Al-4V alloys with density approaching to theoretical value were produced. The effects of various sintering parameters on the microstructure and the properties of the sintered samples were studied. A gas cooling procedure was performed to synthesize the alloy for modifying the mechanical properties. The cooling rate is important because it determines the final microstructure (crystallite size; colony size) and the recrystallization of the α-phase at the particle boundaries. With the increase of the cooling rate, the densities of sintered compacts increased slightly, the crystallite sizes became finer, the weight fractions of the β-phase increased and the compressive yield strength, ultimate strength and the plastic strain increased slightly. The fracture morphology of the sintered samples consisted of smooth shear bands and shear dimples, and the fraction of shear dimples increased with increasing the cooling rate.

Sintering at lower temperatures and for shorter times minimizes undesirable phase transformations. It suppresses grain growth, which results in differences in the microstructure and, consequently, in changes of the mechanical properties. The microstructures of the samples sintered at low temperature contain fine lamella α+β phase structures and recrystallized equiaxial

α grains. With the increase of the sintering temperature, the microstructures were transformed gradually from bimodal grained to coarse grained structure with an increase of the average crystallite sizes. A decrease in yield strength is observed when the colony structure is changed to the Widmanstätten microstructure due to the increase of the size of α-phase lamellas with increasing the sintering temperature from 950°C to 1050°C. The plastic strain increases as the sintering temperature increases from 750°C to 850°C, but the compressive strain starts to decrease in the specimen sintered at 950°C. Similarly, the weight fraction of the β-phase increases as the sintering temperature increases from 750°C to 950°C, but the presence of the β-phase starts to decrease in the specimen sintered at 1050°C. The ductility, showing an increase with increasing sintering temperature first, passes through a maximum and is then declining at highest sintering temperature (1050°C) in this study.

The studies carried out have established that the formations of microstructure were influenced by the cooling rates and the sintering temperature conditions. All samples subjected to field assisted sintering exhibited ductile fracture. The important microstructural parameter on the mechanical properties is the crystallite size, because it determines the effective slip length. During the sintering process, the average crystalline sizes in the samples were restricted to the range of nano-meter scale. The yield strength increases due to the refinement of the finer crystallite microstructure. It should be pointed out that these considerations are not independent of each other and that the observed property enhancement is most likely related to the reduction in the crystallite size. According to the results, a compromise between adequate values of strength and elongation can be achieved with the sintering temperature below the β-transus, i.e., between 850°C and 950°C, applying gas-cooling as a moderate cooling rate. Thus, the routine offers opportunity for the easy synthesis of components in the biomedical applications. Further, cost reduction has been projected, particularly if these structures do not require subsequent reheat treatment.

Implant stability is not only a function of its strength but it is also dependent upon the degree of fixation within the surrounding tissues. Mismatch of Young's moduli of the biomaterials and the surrounding bone has been identified as a major reason for implant loosening. Porous metallic systems possess a large potential to advance the current generation of prostheses and to address unresolved clinical applications. The porous biomaterial is expected to lead to a strong interface between the bone and the implant. The most important advantage of porous implants is

that they allow for ingrowth of bone and other tissues into the pores of the implant, resulting in a mechanical interlocking with the surrounding tissue and a better implant fixation.

The application of a space holder material in the FAST process makes it possible to obtain the porous metallic structures characterized by high porosity. The potential of NaCl for application as a spacer in the space-holder technique has been investigated. Mechanical analysis revealed that the compressive strength and the elastic modulus value lied between the values of human bones. An improvement in the compressive strength of porous Ti-6Al-4V could be achieved through post-sintering treatments. After post-heat steps, the synthesized foams have 45%–81% porosity and an elastic modulus of 1.9 GPa–34.1 GPa, while the compressive strength varied from 18 MPa to 110 MPa. The modulus of such porous biomaterial is very low and thus these materials are expected to overcome the stress shielding effect eventually prolonging device lifetime.

An investigation of the in vitro behavior of cells on porous Ti-6Al-4V scaffolds is described. The results showed that cells were able to attach and spread on the surfaces of scaffolds, and to subsequently form an extracellular matrix, which suggested that the larger pore size and high porosity degree are beneficial for cell attachment, diffusion, vascularization and subsequent new bone formation. Although increased porosities and pore sizes are obviously preferential for new bone growth facilitation in porous titanium alloy implants, it should be kept in mind that another consequence of the porosity and the pore size increase is the reduction of the implant mechanical properties. Therefore, a compromise should be reached between mechanical properties and porosity of materials.

In summary, this method using FAST by dissolution of NaCl spacer and post-heat treatment provides a foamed structure with a close to homogenous pore structure, high levels of porosity and improved mechanical properties. Consequently, the mechanical properties of the metal foams can be adjusted by choosing the size and quantity of the space-holder material used. The results indicate that the porous Ti-6Al-4V scaffolds have the properties to be potentially employed in orthopaedic applications.

5.2. Concluding remarks and future directions

Biomaterials need a co-work of many adjacent sciences like biology, chemistry, engineering, medicine or physics because of the interdisciplinary approach to the subject. According to this study, Ti-6Al-4V sintering by FAST is very efficient and yields accurate lab results. However, a

clinical use of these is still far away due to the long approval procedure to avoid harms of human beings. Therefore, more research is necessary with regard to the implants and effective optimization of these properties can only be possible using interdisciplinary approaches.

In the work presented by this thesis, we have synthesized Ti-6Al-4V using field assisted sintering technique. The ability of titanium and its alloys to conduct new bone formation is limited since they are considered bionert. Therefore, in order to improve their biological performance it might be necessary to either combine them with other, more bioactive biomaterials or to improve their bioactivity by surface modification. The chemical methods and/or heat treatment allow the formation of titanium oxide layers on the Ti surface. The presence of this protective passive layer can also improve the corrosion resistance of titanium and its alloys.

A major concern with the use of Ti-6Al-4V implants in biomedical field is the effect stress shielding. From the biomechanical point of view, it is probably desirable to have a low Young's modulus comparable to that of surrounding bone at the interface of implant and bone, and a gradually increasing Young's modulus away from this interface in order to achieve a continuous load transfer from the bone to the implant. Implants with solid cores and porous coating structures are recommended for future studies.

New frontiers of research should be directed towards better mimicking the properties of natural bone. Implants with a microporous surface and a macroporous interior to mimic the cortical surface and the cancellous interior of natural bone are more appropriate. Gradients in the porosities and the pore sizes will allow on one side of the implants high vascularization and direct osteogenesis and on the other, osteochondral ossification.

Although it is difficult to mimic natural bones, recent scientific and technological findings show potential to achieve implants that would encourage local and systemic biological functions. Prospectively, this kind of Ti-6Al-4V is potential to alleviate the problem of mechanical mismatch between the bones and the Ti alloy implants and may provide a candidate as a long-term bone substitute for biomedical applications.

References

1. Boyce, T., J. Edwards, and N. Scarborough, *Allograft bone: the influence of processing on safety and performance.* Orthopedic Clinics of North America, 1999. **30**(4): p. 571-581.
2. Damien, C.J. and J.R. Parsons, *Bone graft and bone graft substitutes: a review of current technology and applications.* Journal of Applied Biomaterials, 1991. **2**(3): p. 187-208.
3. Stevens, M.M., *Biomaterials for bone tissue engineering.* Materials today, 2008. **11**(5): p. 18-25.
4. Giannoudis, P.V., H. Dinopoulos, and E. Tsiridis, *Bone substitutes: an update.* Injury, 2005. **36**(3): p. S20-S27.
5. Bauer, T., *Bone graft substitutes.* Skeletal radiology, 2007. **36**(12): p. 1105-1107.
6. Steinemann, S., G. Winter, and J. Leray, *Evaluation of biomaterials.* Willey, New York (USA), 1980.
7. Bohner, M., *Calcium orthophosphates in medicine: from ceramics to calcium phosphate cements.* Injury, 2000. **31**: p. D37-D47.
8. Kon, E., et al., *Autologous bone marrow stromal cells loaded onto porous hydroxyapatite ceramic accelerate bone repair in critical‐size defects of sheep long bones.* Journal of biomedical materials research, 2000. **49**(3): p. 328-337.
9. Burg, K.J., S. Porter, and J.F. Kellam, *Biomaterial developments for bone tissue engineering.* Biomaterials, 2000. **21**(23): p. 2347-2359.
10. Hutmacher, D.W., *Scaffolds in tissue engineering bone and cartilage.* Biomaterials, 2000. **21**(24): p. 2529-2543.
11. Langer, R. and D.A. Tirrell, *Designing materials for biology and medicine.* Nature, 2004. **428**(6982): p. 487-492.
12. Williams, D.F., *Definitions in biomaterials: proceedings of a consensus conference of the European Society for Biomaterials, Chester, England, March 3-5, 1986*. Vol. 4. 1987: Elsevier Science Ltd.
13. Ratner, B., et al., *Biomaterials science: an introduction to materials in medicine.* San Diego, California, 2004: p. 162-164.
14. Geetha, M., et al., *Ti based biomaterials, the ultimate choice for orthopaedic implants–A review.* Progress in Materials Science, 2009. **54**(3): p. 397-425.
15. Puleo, D. and A. Nanci, *Understanding and controlling the bone–implant interface.* Biomaterials, 1999. **20**(23): p. 2311-2321.
16. Sumner, D., et al., *Functional adaptation and ingrowth of bone vary as a function of hip implant stiffness.* Journal of biomechanics, 1998. **31**(10): p. 909-917.
17. Huiskes, R., H. Weinans, and B. Van Rietbergen, *The relationship between stress shielding and bone resorption around total hip stems and the effects of flexible materials.* Clinical orthopaedics and related research, 1992. **274**: p. 124-134.
18. Olszta, M.J., et al., *Bone structure and formation: a new perspective.* Materials Science and Engineering: R: Reports, 2007. **58**(3): p. 77-116.
19. Hallab, N., K. Merritt, and J.J. Jacobs, *Metal sensitivity in patients with orthopaedic implants.* The Journal of Bone & Joint Surgery, 2001. **83**(3): p. 428-428.
20. Alhassan, S. and T. Goswami, *Wear rate model for UHMWPE in total joint applications.* Wear, 2008. **265**(1): p. 8-13.
21. Viceconti, M., et al., *Large-sliding contact elements accurately predict levels of bone–implant micromotion relevant to osseointegration.* Journal of biomechanics, 2000. **33**(12): p. 1611-1618.
22. Jain, R.K., et al., *Engineering vascularized tissue.* Nature biotechnology, 2005. **23**(7): p. 821-823.
23. Rouwkema, J., N.C. Rivron, and C.A. van Blitterswijk, *Vascularization in tissue engineering.* Trends in biotechnology, 2008. **26**(8): p. 434-441.
24. Niinomi, M., *Recent metallic materials for biomedical applications.* Metallurgical and materials transactions A, 2002. **33**(3): p. 477-486.
25. McKee, G. and J. Watson-Farrar, *Replacement of arthritic hips by the McKee-Farrar prosthesis.* Journal of Bone & Joint Surgery, British Volume, 1966. **48**(2): p. 245-259.
26. Block, M.S., *Color atlas of dental implant surgery*2010: Elsevier Health Sciences.
27. Long, M. and H. Rack, *Titanium alloys in total joint replacement—a materials science perspective.* Biomaterials, 1998. **19**(18): p. 1621-1639.
28. Leyens, C. and M. Peters, *Titanium and Titanium Alloys*2003.
29. Alloy, N.-b., *Mechanical properties.* Biomaterials Science: An Introduction to Materials in Medicine, 2012.

316: p. 120.
30. Bania, P.J., *Beta titanium alloys and their role in the titanium industry.* Beta Titanium Alloys in the 1990's, 1993: p. 3-14.
31. Ratner, B.D., *A perspective on titanium biocompatibility*, in *Titanium in medicine*2001, Springer. p. 1-12.
32. Niinomi, M., et al., *Corrosion wear fracture of new β type biomedical titanium alloys.* Materials Science and Engineering: A, 1999. **263**(2): p. 193-199.
33. Liu, X., P.K. Chu, and C. Ding, *Surface modification of titanium, titanium alloys, and related materials for biomedical applications.* Materials Science and Engineering: R: Reports, 2004. **47**(3): p. 49-121.
34. Dujovne, A., et al., *Mechanical compatibility of noncemented hip prostheses with the human femur.* The Journal of Arthroplasty, 1993. **8**(1): p. 7-22.
35. Von Recum, A.F. and J.E. Jacobi, *Handbook of biomaterials evaluation: scientific, technical, and clinical testing of implant materials*1999: CRC Press.
36. Schuh, A., et al., *Second generation (low modulus) titanium alloys in total hip arthroplasty.* Materialwissenschaft und Werkstofftechnik, 2007. **38**(12): p. 1003-1007.
37. Frosch, K.-H. and K.M. Stürmer, *Metallic biomaterials in skeletal repair.* European Journal of Trauma, 2006. **32**(2): p. 149-159.
38. Pohler, O.E., *Unalloyed titanium for implants in bone surgery.* Injury, 2000. **31**: p. D7-D13.
39. Ratner, B., *Titanium in Medicine: Material Science.* Surface Science, Engineering, Biological Responses and Medical Applications, 2001: p. 2.
40. Apple, D., et al., *Biocompatibility of implant materials: a review and scanning electron microscopic study.* Journal-American Intra-Ocular Implant Society, 1983. **10**(1): p. 53-66.
41. Becker, B. and J. D BOLTON, *Corrosion behaviour and mechanical properties of functionally gradient materials developed for possible hard-tissue applications.* Journal of Materials Science: Materials in Medicine, 1997. **8**(12): p. 793-797.
42. Textor, M., et al., *Properties and biological significance of natural oxide films on titanium and its alloys*, in *Titanium in medicine*2001, Springer. p. 171-230.
43. Khan, M., R. Williams, and D. Williams, *The corrosion behaviour of Ti–6Al–4V, Ti–6Al–7Nb and Ti–13Nb–13Zr in protein solutions.* Biomaterials, 1999. **20**(7): p. 631-637.
44. Hutchings, I.M., *Tribology: friction and wear of engineering materials: Edward Arnold,(Fax:+ 44 (0) 732 461321) 1992, 352pp, ε19. 95 paperback, ISBN 0 340 56184.* Materials & Design, 1992. **13**(3): p. 187.
45. Jasty, M., *Clinical reviews: particulate debris and failure of total hip replacements.* Journal of Applied Biomaterials, 1993. **4**(3): p. 273-276.
46. Lakes, R.S., *Biomaterials: an introduction*2007: Springer.
47. Miller, P. and J. Holladay, *Friction and wear properties of titanium.* Wear, 1958. **2**(2): p. 133-140.
48. Hernández de Gatica, N.L., G.L. Jones, and J.A. Gardella, *Surface characterization of titanium alloys sterilized for biomedical applications.* Applied surface science, 1993. **68**(1): p. 107-121.
49. Rieu, J., et al., *Ion implantation effects on friction and wear of joint prosthesis materials.* Biomaterials, 1991. **12**(2): p. 139-143.
50. Zhecheva, A., et al., *Enhancing the microstructure and properties of titanium alloys through nitriding and other surface engineering methods.* Surface and Coatings Technology, 2005. **200**(7): p. 2192-2207.
51. Bloyce, A., *Surface engineering of titanium alloys for wear protection.* Proceedings of the Institution of Mechanical Engineers, Part J: Journal of Engineering Tribology, 1998. **212**(6): p. 467-476.
52. Welsch, G., R. Boyer, and E. Collings, *Materials properties handbook: titanium alloys*1993: ASM international.
53. Ibrahim, A., et al., *Processing of porous Ti and Ti5Mn foams by spark plasma sintering.* Materials & Design, 2011. **32**(1): p. 146-153.
54. Asaoka, K., et al., *Mechanical properties and biomechanical compatibility of porous titanium for dental implants.* Journal of biomedical materials research, 1985. **19**(6): p. 699-713.
55. Ye, B. and D.C. Dunand, *Titanium foams produced by solid-state replication of NaCl powders.* Materials Science and Engineering: A, 2010. **528**(2): p. 691-697.
56. Brunette, D.M., Tengvall, P., Textor, M., Thomsen, P., *Titanium in Medicine*2001, Berlin: Springer.
57. Ratner, B.D., *Biomaterials science: an introduction to materials in medicine*2004: Academic press.
58. Niinomi, M., *Mechanical biocompatibilities of titanium alloys for biomedical applications.* Journal of the Mechanical Behavior of Biomedical Materials, 2008. **1**(1): p. 30-42.
59. Tokita, M. *Development of large-size ceramic/metal bulk FGM fabricated by spark plasma sintering*. in *Materials science forum*. 1999. Trans Tech Publ.

60. Munir, Z.A., D.V. Quach, and M. Ohyanagi, *Electric current activation of sintering: a review of the pulsed electric current sintering process.* Journal of the American Ceramic Society, 2011. **94**(1): p. 1-19.
61. Munir, Z., U. Anselmi-Tamburini, and M. Ohyanagi, *The effect of electric field and pressure on the synthesis and consolidation of materials: a review of the spark plasma sintering method.* Journal of Materials Science, 2006. **41**(3): p. 763-777.
62. Anselmi-Tamburini, U., et al., *Fundamental investigations on the spark plasma sintering/synthesis process: II. Modeling of current and temperature distributions.* Materials Science and Engineering: A, 2005. **394**(1): p. 139-148.
63. Mamedov, V., *Spark plasma sintering as advanced PM sintering method.* Powder Metallurgy, 2002. **45**(4): p. 322-328.
64. Sosnik, B., *US Patent, 2434775.* 1948.
65. Banhart, J., *Manufacture, characterisation and application of cellular metals and metal foams.* Progress in materials Science, 2001. **46**(6): p. 559-632.
66. Ryan, G., A. Pandit, and D.P. Apatsidis, *Fabrication methods of porous metals for use in orthopaedic applications.* Biomaterials, 2006. **27**(13): p. 2651-70.
67. Dunand, D.C., *Processing of titanium foams.* Advanced Engineering Materials, 2004. **6**(6): p. 369-376.
68. Davis, N., et al., *Solid-state foaming of titanium by superplastic expansion of argon-filled pores.* JOURNAL OF MATERIALS RESEARCH-PITTSBURGH-, 2001. **16**(5): p. 1508-1519.
69. St-Pierre, J.-P., et al., *Three-dimensional growth of differentiating MC3T3-E1 pre-osteoblasts on porous titanium scaffolds.* Biomaterials, 2005. **26**(35): p. 7319-7328.
70. Nakajima, H., T. Ikeda, and S. Hyun, *Fabrication of Lotus‐type Porous Metals and their Physical Properties.* Advanced Engineering Materials, 2004. **6**(6): p. 377-384.
71. Li, B.-Y., et al., *A recent development in producing porous Ni–Ti shape memory alloys.* Intermetallics, 2000. **8**(8): p. 881-884.
72. Oh, I.-H., et al., *Mechanical properties of porous titanium compacts prepared by powder sintering.* Scripta Materialia, 2003. **49**(12): p. 1197-1202.
73. Fujibayashi, S., et al., *Osteoinduction of porous bioactive titanium metal.* Biomaterials, 2004. **25**(3): p. 443-450.
74. Yang, Y., et al., *Preparation of graded porous titanium coatings on titanium implant materials by plasma spraying.* Journal of biomedical materials research, 2000. **52**(2): p. 333-337.
75. Xue, W., et al., *Processing and biocompatibility evaluation of laser processed porous titanium.* Acta Biomaterialia, 2007. **3**(6): p. 1007-1018.
76. Krishna, B.V., S. Bose, and A. Bandyopadhyay, *Low stiffness porous Ti structures for load-bearing implants.* Acta Biomaterialia, 2007. **3**(6): p. 997-1006.
77. Heinl, P., C. Körner, and R.F. Singer, *Selective electron beam melting of cellular titanium: mechanical properties.* Advanced Engineering Materials, 2008. **10**(9): p. 882-888.
78. Ryan, G.E., A.S. Pandit, and D.P. Apatsidis, *Porous titanium scaffolds fabricated using a rapid prototyping and powder metallurgy technique.* Biomaterials, 2008. **29**(27): p. 3625-3635.
79. Degischer, H.P. and B. Kriszt, *Handbook of cellular metals: production, processing, applications*2002: Wiley-vch.
80. Kotan, G. and A.Ş. Bor, *Production and characterization of high porosity Ti-6Al-4V foam by space holder technique in powder metallurgy.* Turkish Journal of Engineering and Environmental Sciences, 2007. **31**(3): p. 149-156.
81. Aydoğmuş, T. and Ş. Bor, *Processing of porous TiNi alloys using magnesium as space holder.* Journal of alloys and compounds, 2009. **478**(1): p. 705-710.
82. Esen, Z. and Ş. Bor, *Processing of titanium foams using magnesium spacer particles.* Scripta materialia, 2007. **56**(5): p. 341-344.
83. Gu, Y., et al., *Synthesis and bioactivity of porous Ti alloy prepared by foaming with TiH< sub> 2</sub>.* Materials Science and Engineering: C, 2009. **29**(5): p. 1515-1520.
84. Bansiddhi, A. and D. Dunand, *Shape-memory NiTi foams produced by replication of NaCl space-holders.* Acta biomaterialia, 2008. **4**(6): p. 1996-2007.
85. Rietveld, H., *A profile refinement method for nuclear and magnetic structures.* Journal of applied Crystallography, 1969. **2**(2): p. 65-71.
86. Young, R., *Introduction to the Rietveld method.* The Rietveld Method, 1993. **5**: p. 1-38.
87. Lutterotti, L., *Introduction to diffraction and the Rietveld method.*
88. Lutterotti, L., R. Vasin, and H.-R. Wenk, *Rietveld texture analysis from synchrotron diffraction images. I.*

Calibration and basic analysis. Powder Diffraction, 2014. **29**(01): p. 76-84.
89. Wyckoff, R.W.G., *Crystal Structures*. Second edition ed1967, New York: John Wiley & Sons.
90. Dowling, N.E., *Mechanical behavior of materials: engineering methods for deformation, fracture, and fatigue*1993: Prentice hall.
91. Hertzberg, R.W., *Deformation and fracture mechanics of engineering materials*. Vol. 89. 1996: Wiley.
92. Bergemann, C., et al. *Proliferation and migration of human osteoblasts on porous three dimensional scaffolds*. in *Materials Science Forum*. 2010. Trans Tech Publ.
93. Zhang, F., et al., *The potential of rapid cooling spark plasma sintering for metallic materials.* Materials Today, 2013. **16**(5): p. 192-197.
94. S. Malinov, Z.G., W. Sha, and A. Wilson, *Differential Scanning Calorimetry Study and Computer Modeling of beta alpha Phase Transformation in a Ti-6Al-4V Alloy.* Metallurgical and materials transactions A, 2001. **32A**: p. 879-887.
95. Christian, J.W., *The Theory of Transformations in Metals and Alloys (Part I+ II)*2002: Newnes.
96. Ahmed, T. and H. Rack, *Phase transformations during cooling in< i> α</i>+< i> β</i> titanium alloys.* Materials Science and Engineering: A, 1998. **243**(1): p. 206-211.
97. Lütjering, G., *Influence of processing on microstructure and mechanical properties of (< i> α+ β</i>) titanium alloys.* Materials Science and Engineering: A, 1998. **243**(1): p. 32-45.
98. Voyiadjis, G.Z. and R. Peters, *Size effects in nanoindentation: an experimental and analytical study.* Acta mechanica, 2010. **211**(1-2): p. 131-153.
99. Stauss, S., et al., *Determining the stress–strain behaviour of small devices by nanoindentation in combination with inverse methods.* Microelectronic Engineering, 2003. **67**: p. 818-825.
100. Oh, C.-S., et al., *Comparison of the Young's modulus of polysilicon film by tensile testing and nanoindentation.* Sensors and Actuators A: Physical, 2005. **117**(1): p. 151-158.
101. Rodrıguez, R. and I. Gutierrez, *Correlation between nanoindentation and tensile properties: influence of the indentation size effect.* Materials Science and Engineering: A, 2003. **361**(1): p. 377-384.
102. Malinov, S., W. Sha, and J. McKeown, *Modelling the correlation between processing parameters and properties in titanium alloys using artificial neural network.* Computational Materials Science, 2001. **21**(3): p. 375-394.
103. Lipkin, D., D. Clarke, and G. Beltz, *A strain-gradient model of cleavage fracture in plastically deforming materials.* Acta materialia, 1996. **44**(10): p. 4051-4058.
104. Ryan, G., A. Pandit, and D.P. Apatsidis, *Fabrication methods of porous metals for use in orthopaedic applications.* Biomaterials, 2006. **27**(13): p. 2651-2670.
105. Zhang, F., et al., *Spark plasma sintering of macroporous calcium phosphate scaffolds from nanocrystalline powders.* Journal of the European Ceramic Society, 2008. **28**(3): p. 539-545.
106. An, Y.H. and R.A. Draughn, *Mechanical testing of bone and the bone-implant interface*2010: CRC press.
107. Gibson, L.J. and M.F. Ashby, *Cellular solids: structure and properties*1999: Cambridge university press.
108. Choe, H., et al., *Effect of tungsten additions on the mechanical properties of Ti-6Al-4V.* Materials Science and Engineering: A, 2005. **396**(1): p. 99-106.
109. Biener, J., et al., *Nanoporous Au: A high yield strength material.* Journal of Applied Physics, 2005. **97**(2): p. 024301.
110. Lee, M.H., et al., *High strength porous Ti–6Al–4V foams synthesized by solid state powder processing.* Journal of Physics D: Applied Physics, 2008. **41**(10): p. 105404.
111. Zhang, F., E. Otterstein, and E. Burkel, *Spark plasma sintering, microstructures, and mechanical properties of macroporous titanium foams.* Advanced Engineering Materials, 2010. **12**(9): p. 863-872.
112. Takemoto, M., et al., *Mechanical properties and osteoconductivity of porous bioactive titanium.* Biomaterials, 2005. **26**(30): p. 6014-23.
113. Feng, B., et al., *Characterization of surface oxide films on titanium and bioactivity.* Journal of Materials Science: Materials in Medicine, 2002. **13**(5): p. 457-464.
114. Kim, D.-Y., et al., *Formation of hydroxyapatite within porous TiO< sub> 2</sub> layer by micro-arc oxidation coupled with electrophoretic deposition.* Acta Biomaterialia, 2009. **5**(6): p. 2196-2205.

Acknowledgements

First of all, my greatest thanks and admiration go to my supervisor Prof. Dr. Eberhard Burkel. Thousand thanks for giving me the opportunity to pursue my PhD within your group. Your strength lies in enabling your students to realize their research ideas by giving them all the freedom, advice and support they need, while accepting the differences between the individuals without judging them. I would like to thank my co-promotor, Dr. Faming Zhang who discussed all the results between the important steps together with me. It is you who introduced me to the new area of biomaterials. I greatly appreciate your availability, guidance and feedback.

To my fellow colleagues in Rostock: I want to thank Dieter Skroblin who introduced me to the Rietveld refinement and discussed the experimental results and Rico Schnierer who spent time to support nanoindentation tests. Especially I want to thank Wenwei Gu, Wiktor Bodnar and Kerstin Witte who spent much more time to support my sintering experiments in FAST lab and the X-ray diffraction experiments in Hamburg (DESY). Other people I would like to thank are: Lijun Jing, Qingqing Xu, Martin Hantusch, Ulrike Schröder, Bärbel Przybill and Stephan Flor, thank you all, I am glad we worked together and I sincerely hope that Physics of New Materials will be a great success. I wish you all the best in your further work.

I would also like to express my gratitude to the adjacent work groups at Welisa. Prof. Dr. Rainer Bader gave me the possibility to perform the compression measurements which were performed by Dipl. Rebecca Schubert, Dipl. Carmen Zietz and Mr. Mario Jackszis. Thanks to Dr. Henrike Rebl and Dr. Claudia Bergemann for the measurements of the cell attachments. The SEM images were taken at the EMZ (Electron Microscopic Center) with the assistance from Mr. Gerhard Fulda.

This work was gratefully supported by the DFG GRK1505/1 and GRK1505/2 (Welisa) and I acknowledge the support from China Scholarship Council (CSC). Of course I want to thank my wife Linge Zhu, my parents, young sister and brother, for their enduring love and support.

Declaration

Hereby I declare that I wrote this dissertation myself only with the help of the cited literature and auxiliary means. Up to now, this thesis was not published or presented to another examinations office in the same or similar shape.

Yujie Quan
Rostock, 27th March 2015